

© 2020 Kihoon Park

ON THE GENERATION, DISSIPATION, AND TRANSPORT OF HEAT
IN GaN MATERIALS FOR ADVANCED HIGH-POWER DEVICES

BY
KIHOOON PARK

DISSERTATION

Submitted in partial fulfillment of the requirements
for the degree of Doctor of Philosophy in Electrical and Computer Engineering
in the Graduate College of the
University of Illinois at Urbana-Champaign, 2020

Urbana, Illinois

Doctoral Committee:

Assistant Professor Can Bayram, Chair
Professor Jean-Pierre Leburton
Professor Joseph Lyding
Associate Professor Sanjiv Sinha

ABSTRACT

GaN semiconductors show excellent optical and electronic properties such as large direct bandgap (3.4 eV), high breakdown field (3.3 MV/cm), high saturation velocity (2.5×10^7 cm/s), and high thermal stability. However, many GaN-based devices that rely on the material's capacity to flow high current and sustain high voltage levels suffer from undesirable Joule heating effects that critically limit their performance and device lifetime. Thermal management, therefore, has become essential in applications such as high-brightness light-emitting diodes and AlGaIn/GaN-based high-electron-mobility transistors (HEMTs). An accurate understanding of the thermal properties in GaN material is crucial to improve the reliability and performance of GaN-based high-power devices.

This work addresses the generation, dissipation, and transport of heat in GaN materials and devices. First, the interactions between electrons and optical phonons are investigated to understand the intrinsic electronic and phonon properties in GaN-based structures. Based on the theoretical uniaxial dielectric continuum model, a formalism is developed to calculate the electron mobility and saturation velocity as a function of temperature. It is found that at room temperature, the phonon-limited mobility is ~ 3000 cm²/V-s (with a power law of $T^{-3.1}$) and saturation velocity is $\sim 3.1 \times 10^7$ cm/s. Furthermore, properties of interface and confined optical phonons and their interactions with electrons are studied in an AlN/GaN/AlN quantum well structure. Next, the heat dissipation in GaN/substrate stacks is analyzed using TCAD software to understand the relation between the thermal resistance, thermal boundary resistance (of GaN/substrate interface), and GaN thickness. As commercially available bulk GaN is extremely expensive, cost-driven consumer electronics applications are mostly implemented on GaN grown on foreign substrates. The effects

of these substrates on thermal resistance of GaN devices are investigated considering multiple design parameters. We propose a device design scheme that can be used to optimize the GaN layer thickness and minimize the device thermal resistance assuming an isotropic heat dissipation from the hotspot located under the drain side of the gate. Finally, the dislocation density dependent thermal conductivity of GaN is experimentally investigated using techniques such as cathodoluminescence, X-ray diffraction, secondary ion mass spectroscopy, and time-domain thermorefectance. Four types of GaN samples (hydride vapor phase epitaxy grown GaN, high nitrogen pressure grown GaN, metal-organic chemical vapor deposition grown GaN on sapphire and silicon) are studied to understand the relationship between dislocation density and thermal conductivity. A systematic analysis of the various experimental setup variables of the technique is also performed to optimize the measurement of GaN thermal conductivity.

To electrons and phonons.

ACKNOWLEDGMENTS

I must express my sincerest gratitude to my advisor, Prof. Can Bayram, for accepting me in his group and for his support, advice, philosophy lessons, ideas, and insights. His hands-on approach has inspired me in many ways allowing me to change my perspective on not only scientific research but also on encounters in daily life. I also thank him for giving me the opportunity to work on various subjects that I wouldn't have even imagined learning about if not for him.

I thank Prof. Jean-Pierre Leburton, Prof. Joseph Lyding, and Prof. Sanjiv Sinha for serving on my doctoral committee and providing feedback on this work.

I would like to thank Prof. Michael Strosio for providing me the opportunity to conduct theoretical studies on phonons. When I asked him a question, I was very surprised that someone of his stature would offer to go to the library together to search for an answer. Instead of just giving me ambiguous answers or vague directions, he was kind and enthusiastic enough to guide me through obstacles and show me the way.

I couldn't have come this far without my fellow lab mates, Hsuan-Ping Swamp Lee and Richard Dicky Liu, who have been there with me from the beginning. Their consistent bodily gas emission throughout the days has allowed me to train my ability to focus. I also thank Yi-chia Tsai for sitting next to me. I extend my gratitude to my many former lab mates Jarod, Dennis, Josephine, Josh, Ryan, Taiming, Estelle, Kai, Yifan, Jingyi, Eric, and Subin for their help during my studies.

I would like to acknowledge the support from Dr. Julio Soares, Dr. Mauro Sardela, Dr. Changqiang Chen, Dr. Jade Wang, Dr. Fubo Rao, Edmond Chow, Lavendra Mandyam, and Joe Maduzia for sharing and teaching their expertise on conducting experimental research.

Last but not least, I thank my wife Jung Eun and my family for their love, sacrifice, and support.

This work was supported by the Air Force Office of Scientific Research (AFOSR) through the Young Investigator Program and by the Department of Electrical and Computer Engineering at the University of Illinois through teaching assistantships and the Gregory Stillman Semiconductor Research Award.

TABLE OF CONTENTS

LIST OF TABLES	ix
LIST OF FIGURES	x
CHAPTER 1 INTRODUCTION	1
CHAPTER 2 INTERACTION BETWEEN ELECTRONS AND POLAR OPTICAL PHONONS IN WURTZITE GaN	6
2.1 Introduction	6
2.2 Electron-Phonon Interaction in Bulk Wurtzite Crystals	7
2.3 Electron Mobility and Saturation Velocity	20
2.4 Hotspot Size: Travel Distance of Electrons	24
2.5 Conclusion	28
CHAPTER 3 ELECTRON SCATTERING VIA INTERFACE OPTICAL PHONONS WITH HIGH GROUP VELOCITY IN WURTZITE GaN-BASED QUANTUM WELL HETEROSTRUCTURES	30
3.1 Introduction	30
3.2 Optical Phonon Mode Dispersion in Wurtzite Crystals	32
3.3 Electron-Phonon Scattering Rate	39
3.4 Group Velocity of Emitted Optical Phonons	42
3.5 Conclusion	50
CHAPTER 4 THERMAL RESISTANCE OPTIMIZATION OF GaN/SUBSTRATE STACKS	52
4.1 Introduction	52
4.2 Heat Transfer Basics	53
4.3 Simulation Using Finite Difference Analysis MATLAB Code	57
4.4 Thermal Properties of GaN and Substrate Materials	59
4.5 Device Structure and Simulation Method	62
4.6 Results and Discussion	66
4.7 Conclusion	74
CHAPTER 5 THERMAL CONDUCTIVITY OF GaN	75
5.1 Time-Domain Thermoreflectance (TDTR)	75
5.2 Aluminum Film Characterization	82
5.3 Impact of Dislocations on Thermal Conductivity	86
5.4 Conclusion	103

CHAPTER 6	SUMMARY AND CONCLUSION	105
APPENDIX A	P-CHANNEL CUBIC-PHASE GaN HETEROSTRUCTURE FIELD-EFFECT TRANSISTORS	108
A.1	Introduction	108
A.2	Device Structure and Simulation Method	108
A.3	Results and Discussion	110
A.4	Conclusion	116
APPENDIX B	LOW-TEMPERATURE PHOTOLUMINESCENCE	118
B.1	Optics	120
B.2	Cryostat	123
APPENDIX C	NUMERICAL CALCULATION OF SCATTERING BETWEEN ELECTRONS AND OPTICAL PHONONS IN GaN-BASED QUANTUM WELLS	129
C.1	Main Function	129
C.2	Subfunction: Interface Optical Phonons	133
C.3	Subfunction: Confined Optical Phonons	137
C.4	Subfunction: Electron Wave Vectors	139
REFERENCES	140

LIST OF TABLES

1.1	Basic material parameters of conventional semiconductor materials and GaN. Cost and size of commercially available wafers are also listed together.....	1
2.1	Wurtzite GaN material constants for 300 and 800 K used in the numerical calculations.....	11
3.1	Material constants used in the numerical calculations.....	34
4.1	Thermal conductivity values of GaN and substrate materials from other literature. Thermal conductivities at 300 K and their temperature dependencies are shown together.....	61
4.2	TBR of GaN/substrate interfaces.....	62
4.3	Temperature-dependent thermal conductivity for GaN and other substrate materials, and TBR values for GaN/substrate interfaces used in simulations. For each substrate material, four TBR values are simulated. Temperature-independent thermal conductivity is taken to be equal to the temperature-dependent thermal conductivity at 300 K.....	65
5.1	Dislocation densities measured by CL and XRD and GaN thermal conductivities κ_{GaN} measured by TDTR of HVPE GaN, HNP GaN, GaN/sapphire, and GaN/Si samples.....	96
5.2	Impurity concentrations measured by SIMS and impurity scattering strengths Γ calculated by Klemens's model of HVPE GaN, HNP GaN, GaN/sapphire, and GaN/Si samples.....	96
5.3	Thermal resistance of the GaN samples calculated assuming an AlGaIn/GaN multi-finger HEMT structure. Thicknesses and temperature-dependent thermal conductivity values used in TCAD simulation are listed. TBR between GaN and substrate layers are fixed to a moderate $20 \text{ m}^2\text{K/GW}$	102
A.1	Material parameters for cubic- and hexagonal-phase GaN and AlN. Mobilities in the parentheses are values for carriers in the two-dimensional electron or hole gas channel. The cubic material parameters are used in the p-channel device simulations.....	110
B.1	List of grating and wavelength of the spectrometer.....	119

LIST OF FIGURES

1.1	Reported values of GaN thermal conductivity plotted as a function of its dislocation density. Only data from literature that report both values are collected. No apparent relation can be deduced.....	4
2.1	The unit cell of wurtzite (hexagonal) GaN. The larger orange spheres represent the Ga atom and the smaller blue spheres represent the N atom.	8
2.2	The two extraordinary optical phonon mode branches E_1 and A_1 . These two branches are both Raman and infrared (IR) active and give rise to a Fröhlich interaction.....	8
2.3	The coordinate system set to calculate the electron–optical phonon scattering. The initial electron wave vector \mathbf{k} is on the y-z plane with the z-axis aligned to the optical axis (c -axis). The angles between the electron wave vector \mathbf{k} and the c -axis, and the phonon wave vector \mathbf{q} and the c -axis, are denoted as θ_k and θ , respectively. The azimuthal angle between the wave vectors \mathbf{k} and \mathbf{q} is denoted as ϕ	9
2.4	The phonon frequencies of $E_1(\text{LO})$, $A_1(\text{LO})$, $E_1(\text{TO})$, and $A_1(\text{TO})$ plotted as a function of temperature. Temperature dependence is calculated using Eq. (2.3). Coefficients α and β are set according to Ref. [25].	12
2.5	The LO-like and TO-like polar optical phonon frequencies and their corresponding energies as a function of the angle θ between the phonon wave vector and c -axis for temperatures 300 K (solid lines) and 800 K (dashed lines).	13
2.6	Electron scattering rates $W(\mathbf{k})$ due to emission and absorption of LO-like and TO-like phonon modes plotted as a function of electron initial energy E_k for two different temperatures (a) $T = 300$ K and (b) 800 K. The incident electron angles with respect to the c -axis are set to $\theta_k = 0$ (solid line), $\pi/4$ (dashed line), and $\pi/2$ (dotted line). The temperature affects the scattering rates through the temperature-dependent phonon frequencies and the phonon occupation number.	15
2.7	Electron scattering rates $W(k)$ due to (a) LO-like and (b) TO-like phonon modes plotted as a function of electron incident angle θ_k for a fixed electron initial energy $E_k = 0.1$ eV. Solid lines and dashed lines represent scattering rates when the temperature is $T = 300$ and 800 K, respectively.	17
2.8	(a) Absolute value of the momentum relaxation rates $1/\tau_m$ and (b) the rate of energy change dE_k/dt due to emission and absorption of LO-like and TO-like phonons plotted as a function of electron initial energy E_k . The temperature is $T = 300$ K	

	and the incident electron angles with respect to the c -axis are set to $\theta_k = 0$ (solid line), $\pi/4$ (dashed line), and $\pi/2$ (dotted line).....	19
2.9	The effects of temperature on (a) electron mobility μ and (b) saturation velocity v_{sat} plotted for three different electron incident angles $\theta_k = 0, \pi/4$, and $\pi/2$. The spatial electron concentration is fixed to $N = 5 \times 10^{18} \text{ cm}^{-3}$ in the temperature-dependent electron mobility and saturation velocity calculations. Inset of (a) shows electron mobility as a function of electron concentration for five different. The electron incident angle is fixed to $\theta_k = \pi/2$	23
2.10	Finite element method simulation result showing the position and temperature of the hotspot in a GaN HEMT. The bias conditions used for the simulation are $V_G = 0 \text{ V}$ and $V_D = 50 \text{ V}$. Simulation is done using TCAD Synopsys Sentaurus.	24
2.11	(a) Comparison of saturation velocity and drift velocity and (b) the minimum velocity of the two are shown as a function of the initial energy of the electron. Saturation velocity and drift velocity are calculated based on energy relaxation rates and momentum relaxation rates. We take the smaller value to be the electron velocity at that energy.....	26
2.12	(a) Electron velocity and (b) LO-like phonon scattering rate are combined to show the transport scenario of an electron with initial energy of 0.4 eV. As the electron traverses through the channel, it releases energy and relaxes to the energy labeled as 5. At the point 5, the electron no longer has enough energy to emit LO phonons and thus absorbs energy to arrive at the point 4, and repeats emission and absorption.....	27
2.13	Released energy plotted as a function of position to estimate the hotspot size. Most of the electrons' energy is dumped within 20 nm of the starting point. Energy released beyond 50 nm in the one-dimensional grid is omitted.....	28
3.1	Dielectric constants as a function of phonon frequency. The characteristic frequencies of the dielectric functions which define the range of available interface (IF) and confined (C) mode phonon frequencies are indicated by vertical dashed lines. The region shaded in red (ω_{1t}, ω_{2z}) is where the interface phonons associated with the TO phonon modes of bulk GaN and AlN are defined. The region shaded in blue ($\omega_{1Lz}, \omega_{2Lz}$) is where the interface phonons associated with the LO phonon modes of bulk GaN and AlN are defined. The regions shaded in green (ω_{1z}, ω_{1t}) and magenta ($\omega_{1Lz}, \omega_{1Lz}$) are where the confined phonons are defined.	35
3.2	Dispersion relation of asymmetric interface (q_A^{IF}), symmetric interface (q_S^{IF}), asymmetric confined (q_A^{C}), and symmetric confined (q_S^{C}) mode phonons of the AlN/GaN/AlN quantum well in the (a) low-frequency and (b) high-frequency region. Only a few of the confined mode phonons (two modes each for the asymmetric and symmetric branch with lowest quantum numbers) are plotted.	

	Phonon modes associated with TO phonon modes of AlN and GaN are shown in the lower frequency region (a), whereas those associated with LO phonon modes are in the higher frequency region (b). The interface phonon resonant frequencies are shown in dotted horizontal lines and the other characteristic frequencies are shown in dashed horizontal lines. The x -axis is shown in the dimensionless wave vector qd	38
3.3	Numerically calculated group velocities of interface and confined mode phonons as a function of phonon frequency. For both interface and confined modes, the solid and dashed lines indicate the asymmetric and symmetric phonon modes, respectively. The group velocity of interface phonons goes to zero close to the TO and LO resonant frequency ($\omega_{\text{TO,res}}$ and $\omega_{\text{LO,res}}$ shown in vertical dotted lines). Maximum group velocity of 138 km/s occurs at $\omega = \omega_{\text{LT}}$ for the interface mode phonons. This value is almost 20 times that of the maximum group velocity of the confined mode phonons.	42
3.4	(a) Interface and (b) confined mode phonon scattering rates are calculated and plotted as a function of electron energy. For both modes, the total interface phonon scattering rate combining all phonon modes (including the TO absorption scattering rate) is shown as the black solid line. The droplines with symbols are shown to indicate the threshold energies of TO emission and LO emission scattering. For interface mode scattering, these energies correspond to the TO and LO interface phonon resonant frequency energies $\hbar\omega_{\text{TO,res}} = 71.7$ meV and $\hbar\omega_{\text{LO,res}} = 103.2$ meV, respectively. For confined mode scattering, the threshold energies are in the vicinity of (but not identical to) the TO and LO phonon energies of GaN, $\hbar\omega_{\text{LT}} = 65.8$ meV and $\hbar\omega_{\text{LO}} = 91.9$ meV, respectively.....	43
3.5	Interface and confined mode phonon emission scattering rates of the AlN/GaN/AlN double heterostructure with GaN thickness of $d = 1$ nm. Compared to the $d = 5$ nm case, the interface mode scattering rate (red solid line) shows a factor of 3 increase, whereas the confined mode scattering rate (blue dashed line) shows a factor of 2.5 decrease. Overall, the interface phonon scattering rate is approximately 8 times the confined mode scattering rate with GaN thickness of $d = 1$ nm.....	46
3.6	Number of produced interface phonons as a function of phonon frequency for different electron energies $E_k = 0.12$ (black dashed line), 0.3 (red dotted line), and 0.5 eV (blue solid line). Only the interface phonons involved in the LO emission phonon process are plotted. The LO phonon resonant frequency is indicated as the vertical dotted line. The y -axis represents the integrand of Eq. (3.9) or equivalently the number of phonons emitted with each phonon frequency.	47
3.7	Average group velocity of the emitted interface and confined mode phonons with different GaN thickness $d = 1, 2, 5$, and 10 nm as a function of electron energy E_k . As a reference, the longitudinal acoustic phonon propagation velocity along the c -	

axis [0001] is indicated as the horizontal dashed line. At low energies right above $E_{LO,res} = 103.2$ meV, heterostructures with smaller GaN thickness d show a larger average group velocity. In contrast, as electron energy increases, the average group velocity of heterostructures with thicker d saturates at a larger value.....	48
4.1 Example (a) structure and (b) temperature profile of 1-D heat transfer. (a) Temperature of heat contacts, thicknesses and thermal conductivities of each layer. (b) Temperature distribution has been simulated and calculated by setting $T_{TOP} = 400$ K, $T_{BOT} = 300$ K, $L_1 = 3$ μ m, $L_2 = 7$ μ m, $\kappa_1 = 1.5$ W/cm-K, $\kappa_2 = 4.0$ W/cm-K, and $R_{TB} = 4 \times 10^{-4}$ cm ² K/W.....	55
4.2 Example (a) structure and (b) temperature profile of 2-D heat transfer. (a) Temperature of heat contacts, thicknesses and thermal conductivities of each layer. The heat source size is reduced to L_H . (b) Temperature distribution has been simulated and calculated by setting $T_{TOP} = 400$ K, $T_{BOT} = 300$ K, $L_1 = 0.3$ μ m, $L_2 = 0.7$ μ m, $L_H = 0.1$ μ m, $\kappa_1 = 1.5$ W/cm-K, $\kappa_2 = 4.0$ W/cm-K, and $R_{TB} = 4 \times 10^{-4}$ cm ² K/W.....	59
4.3 Overall process flowchart using TCAD Sentaurus software.....	63
4.4 Temperature rise and simulation time as a function of element count for the same device with different meshing strategies. (a) Uniformly distributed mesh and (b) dense mesh only near the material interface and heat source.....	64
4.5 Thermal resistance as a function of GaN layer thickness for different heat source lengths (0.01, 0.1, 1, 5, 10, and 20 μ m) and TBR values (20 and 40 m ² K/GW). Inset shows simulated GaN/substrate stack schematically where device width, length and substrate thickness are taken as 1 mm, 20 μ m, and 300 μ m, respectively. Heat sink temperature is kept at 300 K. Heat source length (L_{HEAT}), GaN layer thickness (t_{GaN}), and TBR are varied.	67
4.6 The effect of GaN layer thickness on thermal resistance for different substrate materials. Four TBRs (listed in Table 4.3) for each substrate are used. GaN on diamond, SiC, and Si substrates are applied 1 W of dissipated power, whereas those on sapphire substrates are applied 0.3 W of dissipated power. The arrow directions indicate increasing TBR and the symbols indicate the thermal resistance minima.....	68
4.7 Minimum thermal resistance for temperature-independent (filled symbols) and temperature-dependent (open symbols) thermal conductivity cases. 0.3 W of dissipated power was applied to the GaN/sapphire stack, and 1 W of dissipated power was applied to the rest to limit hotspot GaN temperature below 800 K.....	69
4.8 Temperature reduction with thickness optimization as a function of dissipated power and various TBR values for GaN-on-diamond stack. The temperature reduction is calculated as the temperature difference between the device with	

	optimal GaN layer thickness and a device with GaN layer thickness of 4 μm . The arrow direction indicates decreasing TBR.....	70
4.9	(a) The 3-D device structure, (b) temperature profile along the surface under the heat source in the z -axis direction, (c) temperature profile from the center (2-D and 3-D) and edge of the heat source to the heat sink in the y -axis direction, and (d) maximum temperature dependence on GaN layer thickness.....	72
5.1	Photograph of TDTR measurement setup.	75
5.2	Schematic of the TDTR measurement setup with its laser beam paths. The red and green lines show the pump and probe laser beam paths, respectively.....	76
5.3	Thermal penetration depths d_p as a function of modulation frequency with thermal conductivity of 100, 150, and 200 W/m-K.	81
5.4	Schematic diagram of the heat flow that is analyzed. At left, the laser spot size is larger than the thermal penetration depth. At right, the spot size is comparable to the penetration depth.....	82
5.5	XRR measurement data showing results obtained from different samples with different thicknesses. Through detailed modeling, not only the thickness of the film but also the density of the material and interface roughness can be extracted.	83
5.6	Sensitivity plot showing parameters that can be altered in TDTR analysis. The sensitivity plot is generated for an Al/SiO ₂ /Si system with thicknesses approximately 70 nm, 500 nm, and 500 μm , respectively. The parameters with the largest influence are heat capacity and thickness of aluminum shown in red and green curves.	84
5.7	Surface scanning electron microscopy (SEM) images of sputtered aluminum using (a), (b) Sputter-1 and (c), (d) AJA3. The aluminum was sputtered onto samples of (a) Al ₂ O ₃ , (b) GaN on Al ₂ O ₃ , (c) and (d) SiO ₂ on Si substrates. All images were taken with the same resolution and accelerating voltages.	85
5.8	Heat map of laser spot size versus modulation frequency. Laser spot size must be larger than thermal penetration depth to assure heat flow is mostly one dimensional and the model is properly capturing the physics. For accurate analysis, the ratio should be larger than 4. Also shown together (as horizontal dashed lines) are the laser spot sizes obtained in the system with objective lenses of 5, 10, and 20 times magnification. Thermal penetration depth is calculated based on $\kappa = 175 \text{ W/m-K}$ and $C_{\text{P,GaN}} = 2.64 \text{ J/cm}^3\text{K}$ for a GaN sample with moderate thermal conductivity.....	90
5.9	TDTR measurement results of HNP GaN. (a) In-phase signal V_{in} , (b) out-of-phase signal V_{out} , (c) ratio $-V_{\text{in}}/V_{\text{out}}$ and their fitting results, and (d) thermal conductivity from multiple measurements and average values with five different laser powers (20, 24, 32, 40, and 48 mW). At higher power, noise signals included in the	

relatively small out-of-phase signal have smaller effect on the analysis of the ratio.....	91
5.10 TDTR measurement results ($-V_{in}/V_{out}$ as a function of time delay) and fitted κ_{GaN} of (a) HVPE GaN, (b) HNP GaN, (c) GaN/sapphire, and (d) GaN/Si. Open symbols indicate measurement data, solid lines indicate thermal transport model calculation (with fitting parameters listed), and dashed lines indicate thermal transport model calculations with $\kappa_{\text{GaN}} \pm 10\%$	93
5.11 CL images of (a) HVPE GaN, (b) HNP GaN, (c) GaN/sapphire, and (d) GaN/Si.	95
5.12 Representative XRD ω scans in the (a) (0002) symmetric and (b) (10 $\bar{1}$ 2) asymmetric planes are performed for the HVPE GaN, HNP GaN, GaN/sapphire, and GaN/Si samples (shown in magenta, red, blue, and orange, respectively). FWHM of the ω scans are extracted and used to estimate the dislocation density of each sample. Multiple scans are performed for each sample to obtain an average value.....	96
5.13 SIMS measurement results of the (a) HVPE GaN, (b) HNP GaN, (c) GaN/sapphire, and (d) GaN/Si samples. Average concentration values of impurities Si, H, C, and O are used in the Klemens's model to calculate the scattering strength Γ between phonons and impurities.....	99
5.14 GaN thermal conductivity of HVPE GaN, HNP GaN, GaN/sapphire, and GaN/Si plotted as a function of σ_D (open symbols). Empirical model by Mion et al. from Ref. [136], $\kappa_{\text{GaN}} = 230 \tanh^{0.12}(5 \times 10^6 / \sigma_D)$ (dotted line), new empirical model, $\kappa_{\text{GaN}} = 210 \tanh^{0.12}(1.5 \times 10^8 / \sigma_D)$ (dashed line, this work), and modified Klemens's model (solid line, this work) are plotted together for comparison.....	100
A.1 Schematic of simulated device. Thicknesses of the AlGaIn layers are t_1 , t_2 , and t_3 , with t_3 being the thickness of the topmost AlGaIn layer.....	109
A.2 Energy band diagram of the device under equilibrium condition with different aluminum contents.....	111
A.3 Comparison of maximum channel hole density with varying aluminum content. Hole density increases with aluminum content.....	111
A.4 Drain current at low drain bias (50 mV) with different aluminum contents. Irregular characteristics are due to hole pile-up at the SiO ₂ /AlGaIn interface.....	112
A.5 Valence band diagram at gate voltage of -10 V showing formation of the secondary hole channel at the SiO ₂ /AlGaIn interface for aluminum content of 0.25 and 0.5.....	112
A.6 Band diagram with different AlGaIn layer thickness t_3 at equilibrium. <i>Thickening</i> the layer increases hole density in the channel.	112
A.7 Band diagram with different AlGaIn layer thickness t_1 at equilibrium. <i>Thinning</i> the layer increases hole density in the channel.....	112

A.8	Band diagram with different AlGaIn layer thickness t_2 at equilibrium. <i>Thickening</i> the layer increases the hole density in the channel.	113
A.9	Band diagram with different δ -doping concentrations at equilibrium. Hole density in the channel increases with doping level.	113
A.10	Hole density distribution with different δ -doping concentrations. Doping level of $3 \times 10^{19} \text{ cm}^{-3}$ shows normally-ON behavior.	114
A.11	Transfer characteristics with different δ -doping levels. Threshold voltage is controlled effectively by adjusting δ -doping levels.	114
A.12	Transfer characteristics with different SiO ₂ thicknesses at (a) $V_D = 50 \text{ mV}$ and (b) 5 V	115
A.13	Band diagram with various gate metals.	115
A.14	Band diagram and hole density distribution at different gate voltages using default parameters.	116
A.15	I_D - V_D characteristics at different gate voltages using default parameters.	116
B.1	Photograph of photoluminescence setup at MRL used to investigate LEDs and schematic diagram of the optics, equipment, sample, and laser beam path.	118
B.2	Photograph of the wavelength calibration step using mercury-neon lamp and spectrometer readings of the lamp after calibration. The red dotted vertical lines show a few emission wavelengths that coincide with mercury-neon emission lines.	119
B.3	Power module for the 266 nm laser.	121
B.4	Camera installed into the spectrometer.	121
B.5	Laser focused on the sample, and lenses collimating and focusing photoluminescence light on slit of spectrometer is shown.	122
B.6	266 nm wavelength notch is installed right before the slit to filter out stray laser source light arriving at spectrometer.	122
B.7	(Left) Optics aligned beam path where 45° angle mirror was used. (Right) Sample inside cryostat sample chamber.	123
B.8	Vacuum pump connected to cryostat.	124
B.9	Vacuum pump connected to exhaust.	124
B.10	Photograph showing pipes, valves, and He ₂ gas tank.	125
B.11	Schematic diagram of cryostat vacuum pump.	125
B.12	Cryostat chamber with liquid N ₂ filled and heating coils wrapped around knobs.	127

B.13	Wire connection on top of the sample space used to measure and control temperature.....	127
------	---	-----

CHAPTER 1 INTRODUCTION

Power electronics is a type of electronic devices and circuits that deals with collecting, delivering, and storing energy by conversion and control of electrical power [1], [2]. It is estimated that more than 30% of the energy consumed around the whole globe is through electric power and 50% of that electrical power is controlled by power electronics [3]. Therefore, the performance of the power electronic devices is of critical importance.

The performance of the semiconductor devices that comprise the power electronics is theoretically limited by the intrinsic material parameters of the semiconductor. The combined figure of merit (CFOM), expressed as

$$\text{CFOM} = \frac{\kappa \varepsilon_0 \mu v_{\text{sat}} E_c^2}{[\kappa \varepsilon_0 \mu v_{\text{sat}} E_c^2]_{\text{Si}}}, \quad (1.1)$$

states that wide band gap semiconductor materials are ideal candidates for high-power and high-frequency power electronics. Here, κ is the thermal conductivity, ε_0 is the dielectric constant, μ is the electron mobility, v_{sat} is the saturation velocity, and E_c is the critical electric field.

Table 1.1. Basic material parameters of conventional semiconductor materials and GaN. Cost and size of commercially available wafers are also listed together.

Properties	Si	GaAs	SiC	GaN
Electron Saturation Velocity ($\times 10^7$ cm/s)	1.0	1.3	2.0	2.5
Electron Mobility ($\text{cm}^2/\text{V-s}$)	1400	8500	700	2000 ^a
Critical Electric Field (MV/cm)	0.3	0.4	3.0	3.5
Thermal Conductivity (W/cm-K)	1.5	0.5	3.5	1.8
Maximum Operation Temperature (K)	300	300	600	700
Available Maximum Wafer Size (in)	12	8	4	2 ^b
Cheapest Cost per Area ($\$/\text{cm}^2$)	0.04	2.0	7.9	310

^a 2DEG

^b Bulk GaN wafers

In Table 1.1, the basic material parameters of GaN and a few other conventional semiconductor materials are listed together. The comparison of material parameters reveals that GaN is a suitable candidate for high-frequency and high-power electronics. However, also shown is that due to the lack of availability of large-size wafers, the cost per area is much higher than that of other materials.

In order to reduce the cost of GaN wafers, using metal-organic chemical vapor deposition (MOCVD) or molecular-beam epitaxy (MBE), GaN is heteroepitaxially grown on large-size foreign wafers such as Si (111), SiC, or sapphire. Typically, less than 10- μ m-thick GaN films are grown that would function as the active layer of light-emitting diodes (LEDs) or as the channel of high-electron-mobility transistors (HEMTs). The drawback of this approach is the necessity to grow interlayers and nucleation layers to reduce the lattice mismatch between GaN and Si (111) (17%), SiC (3.5%), and sapphire (14%) such that the GaN layer does not suffer from its low crystallographic quality. However, due to these many interlayers and nucleation layers, the heat generated at the GaN layer is more difficult to remove for most GaN-based device configurations where the heat sink is located at the bottom of the substrate. As the GaN-based transistors drive high levels of voltage and current compared to conventional Si-based power transistors in a much smaller area, they produce excessive heat which can be detrimental to their electrical performance [4], [5]. Prolonged overheating of the device may also lead to device failure; the device's operation temperature is shown to have an exponential relationship with device lifetime [6]. Hence, to realize GaN-based high-frequency and high-power devices, a thorough understanding of thermal management issues is required. To that end, this dissertation addresses the generation, dissipation, and transport of heat in GaN material and GaN-based devices for the realization of more reliable high-power devices.

To study the generation of heat in GaN material, the interaction between electrons and optical phonons is discussed. In a polar semiconductor such as wurtzite GaN, the electron interaction with polar optical phonons determines carrier mobilities and saturation velocities in many cases. For bulk materials, the phonon energy dispersion relation, which determines their extent of interaction with electrons, is mostly fixed. However, with the state-of-the-art technology that allows us to build sophisticated quantum systems using GaN-based material, we now have the power to alter the quantum confinement of carriers and phonons and build lower-dimensional systems that can exhibit different behaviors of electron–phonon interactions. Also, phonon mode mixing between materials forming heterostructures plays an important role and offers room for improvement. On top of the intrinsic superior optical and electronic properties of the material, with phonon engineering, the performance of GaN-based devices can be enhanced further.

In optical and electronic GaN-based devices, heterostructures involving AlGa_N or InGa_N compounds are frequently employed to form quantum wells with specific electron energy levels, induce piezoelectric polarization or lessen epilayer growth issues. In either type of device, an understanding of the interplay between electrons and phonons must be incorporated to fully exploit the material’s excellent properties. The discrepancy between the generation rate of optical phonons and the rate of their decay to heat-carrying-acoustic-phonons causes the hot-phonon bottleneck effect in high-electron-mobility transistors. In quantum well lasers, the thermalization time of electrons determines the laser’s modulation frequency. By controlling the dimensions and the material of these heterostructures, the dynamics of electron–phonon interaction can be engineered to reduce these detrimental effects.

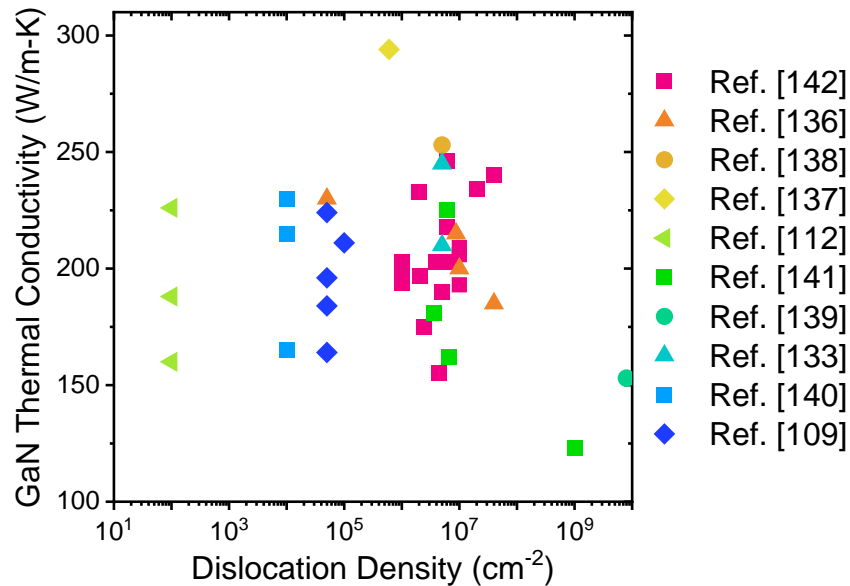


Figure 1.1 Reported values of GaN thermal conductivity plotted as a function of its dislocation density. Only data from literature that report both values are collected. No apparent relation can be deduced.

Next generation high-power and high-frequency power electronics will operate at power densities and frequencies reaching up to 60 W/mm and 10 GHz, respectively. Unless the thermal resistance of the device is sufficiently low, device operation will produce excessive heat at the electron channel which will degrade its performance. Currently, thermal properties of GaN as well as GaN/substrate interfaces are not well understood. The literature reports a large spread of available GaN thermal conductivity (130 to 250 W/m-K) and TBR (10 to 60 m²K/GW). For example, Figure 1.1 shows reported values of GaN thermal conductivity as a function of its dislocation density. This suggests that the thermal properties of the system are extremely sensitive to growth conditions and that the research community lacks understanding of the critical source of such degradations.

The remainder of this dissertation is organized as follows: In Chapter 2, the uniaxial dielectric continuum model is combined with the temperature-dependent phonon mode frequency model to study the temperature- and orientation-dependent polar optical phonon limited electron mobility and saturation velocity in bulk uniaxial semiconductors. The formalisms for calculating electron

scattering rates, momentum relaxation rates, and rate of energy change as a function of the electron kinetic energy and incident electron angle with respect to the c -axis are presented and evaluated numerically. In Chapter 3, the uniaxial dielectric continuum model is further developed to study the interaction between electrons and optical phonons of interface and confined modes in wurtzite AlN/GaN/AlN quantum well heterostructure. The formalisms describing the interface and confined mode optical phonon dispersion relation, electron–phonon scattering rates, and average group velocity of emitted optical phonons are developed and numerically calculated to explore the possibility of exploiting high group velocity interface mode optical phonons as an additional heat dissipation channel in GaN-based heterostructures. In Chapter 4, the effects of thermal boundary resistance and temperature-dependent thermal conductivity on the thermal resistance of GaN/substrate material stacks are studied using technology computer-aided design software. Through multiple simulations considering combination of different parameters such as material of substrate (diamond, silicon carbide, silicon, and sapphire), thermal boundary resistance, heat source length, and power dissipation levels, it is shown that there exists an optimal GaN layer thickness that can reduce the thermal resistance of the whole material stack. In Chapter 5, four different types of GaN samples (namely, hydride vapor phase epitaxy grown freestanding GaN, high nitride pressure grown freestanding GaN, and metal-organic chemical vapor deposition grown GaN on sapphire and silicon substrates) are studied to establish the relationship between thermal conductivity of GaN and dislocation density. The dislocation densities of the GaN samples are examined using cathodoluminescence and X-ray diffraction technique, and the thermal conductivities are measured using time-domain thermoreflectance technique. Chapter 6 summarizes and concludes the dissertation.

CHAPTER 2 INTERACTION BETWEEN ELECTRONS AND POLAR OPTICAL PHONONS IN WURTZITE GaN

Parts of this chapter are reproduced from [7], with the permission of AIP Publishing.

2.1 Introduction

Gallium nitride (GaN) with high breakdown field (3.3 MV/cm), high electron saturation velocity (2.5×10^7 cm/s) and high electron mobility (2000 cm²/V-s) is an ideal material for electronics [8]. Under many device configurations such as in AlGaIn/GaN high-electron-mobility transistors, the temperature of the GaN layer (where electrons are transported through/across) can easily reach above $> 100^\circ\text{C}$ [9]. Among scattering mechanisms limiting the electron mobility (ionized impurity scattering, alloy disorder scattering, interface- or surface-roughness scattering, and acoustic and optical phonon scattering [10], [11], [12], [13]), the most prominent one under such elevated temperatures is reported to be the polar optical phonon scattering [14], [15]. For this reason, interactions between electrons and polar optical phonons and/or electron mobility and saturation velocity in GaN-based devices have been under intense investigation by theoretical means; these investigations either focus solely on the optical phonon limited electron transport or take into account other scattering mechanisms as well [10], [11], [14], [16], [17]. The majority of these investigations (with a few exceptions [18], [19]) are done in the framework of the dielectric continuum model of cubic crystals which treats the polar optical phonons in wurtzite crystals as isotropic, assuming that the anisotropy emerging from the wurtzite model is small enough to be ignored [20]. However, such models fundamentally ignore the inherent uniaxial properties of wurtzite GaN. Thus, a theory providing an understanding of the theoretical limits of the uniaxial electronic properties of GaN materials is essential for enabling advanced devices such as vertical

GaN devices [21]. Another futuristic device in which this theory portends utility is the polariton laser. It is expected that the transverse optical phonon modes play a larger role in the polariton laser [22].

In this chapter, we develop the anisotropic dielectric continuum model for uniaxial crystals and investigate the electron–polar optical phonon interactions in bulk wurtzite GaN considering its angular variance with respect to the c-axis. Although the calculations are done assuming bulk optical phonons, the discussions are not restricted to bulk materials. In two-dimensional systems, based on the dielectric continuum model, there originally exist two types of phonon modes: the half space modes and interface modes. Electrons traversing in the two-dimensional channel formed at the heterointerface of the AlGaN/GaN experience scattering processes with both types of phonons. However, it has been shown that the sum of the two form factors associated with these modes is equal to the form factor for bulk optical phonons [23]. Hence, the results obtained in this work may be applied to electron–phonon interactions in two-dimensional channels as well.

2.2 Electron-Phonon Interaction in Bulk Wurtzite Crystals

For wurtzite crystals, due to their lower symmetry compared to zincblende crystals, there are more distinct phonon branches. The crystal structure of the wurtzite GaN is shown in Figure 2.1. As in the cubic (zincblende) crystals, the bonding is tetrahedral and they have four atoms per unit cell. The lattice vibrations may be classified in terms of orientation with respect to the c-axis, the phonon wave vector \mathbf{q} , the electric field E , and the polarization P . This divides the lattice vibrations into two groups of phonons: ordinary and extraordinary. For the extraordinary phonons, the phonon frequencies are dependent on the angle between the phonon wave vector \mathbf{q} and the c-axis (θ).

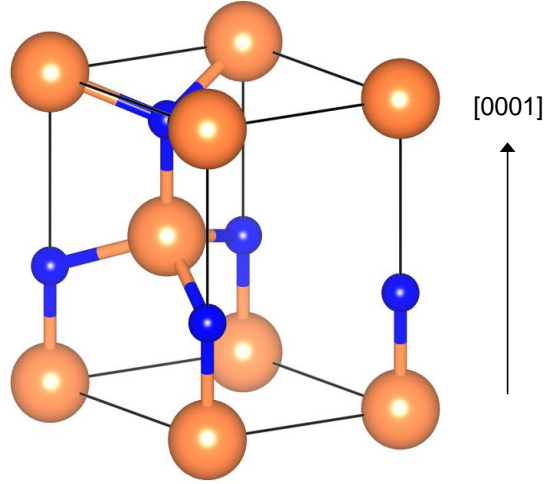


Figure 2.1. The unit cell of wurtzite (hexagonal) GaN. The larger orange spheres represent the Ga atom and the smaller blue spheres represent the N atom.

Two of the extraordinary optical branches correspond to the A_1 and E_1 modes (Figure 2.2); both are Raman and infrared (IR) active. For $\theta = 0$, the $A_1(\text{LO})$ and $E_1(\text{TO})$ modes give rise to a Fröhlich interaction. The $A_1(\text{LO})$ is the mode where the two positive ions (in the four-atom unit cell of the wurtzite structure) are displaced along the c -axis, and the two negative ions are displaced along the c -axis in the opposite direction; thus, the $A_1(\text{LO})$ mode produces a polarization \mathbf{P} directed along the c -axis. Likewise, for $\theta = 0$ the $E_1(\text{TO})$ mode is characterized by displacements of the two positive ions perpendicular to the c -axis, and the two negative ions are displaced in the opposite

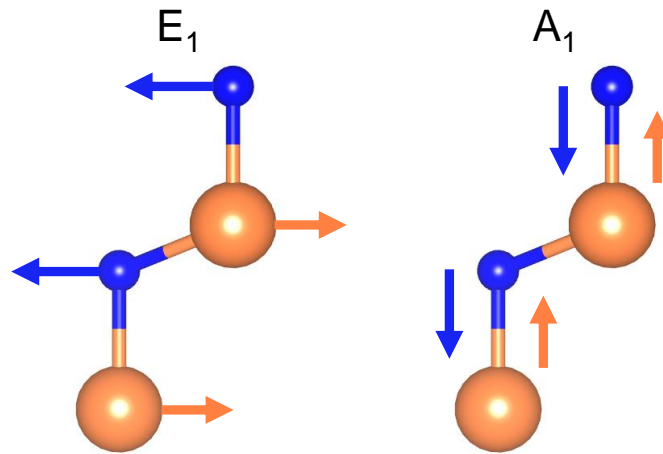


Figure 2.2. The two extraordinary optical phonon mode branches E_1 and A_1 . These two branches are both Raman and infrared (IR) active and give rise to a Fröhlich interaction.

direction; thus, the $E_1(\text{TO})$ mode produces a polarization \mathbf{P} directed perpendicular to the c -axis. As θ varies between 0 and $\pi/2$, the modes are mixed and do not have purely LO or TO character. These Fröhlich interactions produce strong carrier–polar optical phonon interactions leading to carrier scattering.

The dielectric continuum model of uniaxial wurtzite crystals provides a formalism that can be used to calculate properties that have a dependency on the angle between the phonon wave vector \mathbf{q} and the c -axis, denoted here as θ (Figure 2.3). This dependency stems from the solution of Loudon’s model [24] for frequencies of extraordinary phonons which is expressed as [20]

$$\omega_{\text{LO}}^2 = \omega_{\text{zL}}^2 \cos^2 \theta + \omega_{\text{zL}}^2 \sin^2 \theta \quad (2.1)$$

$$\omega_{\text{TO}}^2 = \omega_{\text{zT}}^2 \sin^2 \theta + \omega_{\text{zT}}^2 \cos^2 \theta \quad (2.2)$$

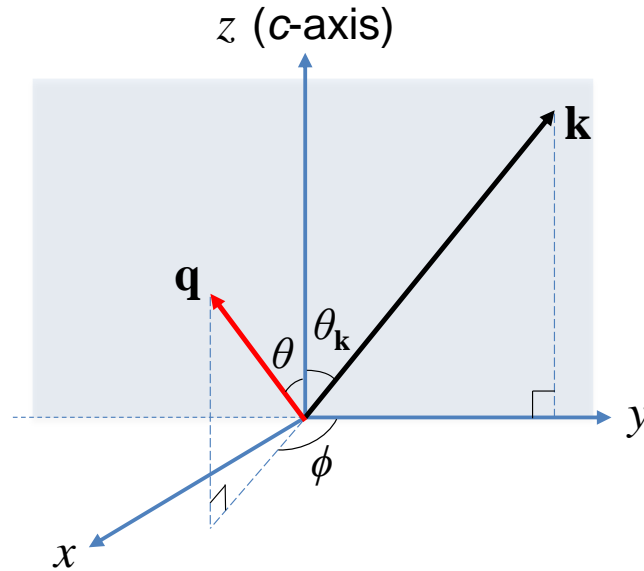


Figure 2.3. The coordinate system set to calculate the electron–optical phonon scattering. The initial electron wave vector \mathbf{k} is on the y - z plane with the z -axis aligned to the optical axis (c -axis). The angles between the electron wave vector \mathbf{k} and the c -axis, and the phonon wave vector \mathbf{q} and the c -axis, are denoted as θ_k and θ , respectively. The azimuthal angle between the wave vectors \mathbf{k} and \mathbf{q} is denoted as ϕ .

where ω_L and ω_T are longitudinal-optical (LO) and transverse-optical (TO) phonon frequencies with the subscripts z and \perp indicating directions parallel and perpendicular to the c -axis, respectively. These phonon modes ω_{LO} and ω_{TO} are purely LO and TO modes, respectively, only when the angle is $\theta = 0$ or $\pi/2$. For intermediate angles between $\theta = 0$ and $\pi/2$, the modes are mixed, and for this reason we refer to ω_{LO} as longitudinal-optical-like (LO-like) phonon mode frequency and ω_{TO} as transverse-optical-like (TO-like) phonon mode frequency. In the case of cubic crystals, the θ dependence is completely absent because of the condition $\omega_{zL} = \omega_{\perp L}$ and $\omega_{zT} = \omega_{\perp T}$, which simplifies Eqs. (2.1) and (2.2) to $\omega_{LO} = \omega_{zL}$ and $\omega_{TO} = \omega_{zT}$, respectively. Hence, cubic crystals are referred to as isotropic materials, whereas wurtzite crystals are referred to as uniaxial materials since their properties must be specified considering the angle with respect to the c -axis. In addition, due to this mixing of the two phonon modes in wurtzite crystals, the interaction between electrons and the TO-like phonon modes cannot be ignored as in the cubic crystals. Pure TO phonon modes only produce displacements of oppositely charged planes such that their normal distance between each other is fixed; that is, the charged planes only *slide by* each other, resulting in negligible contributions to the electron–polar optical phonon interaction. In contrast, pure LO phonon modes produce displacements of oppositely charged planes such that the normal distance between the planes is varied, making them the dominant source of electron–polar optical phonon interaction. As the TO-like phonon mode in wurtzite crystals is only purely TO mode when $\theta = 0$ and $\pi/2$, the effect of phonon modes with intermediate angles on the electron-phonon interaction must be considered.

To fully understand the electron–polar optical phonon interactions and evaluate electronic properties for not only room temperature but also higher temperatures, the effect of temperature

on phonon mode frequencies is implemented in the calculations by using temperature-dependent phonon mode frequencies [25]. The general expression is given by

$$\omega = \omega_0 - \alpha T - \beta T^2 \quad (2.3)$$

where ω_0 is the extrapolated phonon frequency at 0 K, T is the temperature, and α and β are the first- and second-order temperature coefficients, respectively. GaN material constants including the phonon mode frequencies at temperatures of 300 and 800 K are listed in Table 2.1. In this work, the maximum temperature is limited to 800 K as GaN devices are reported to show degraded characteristics when the operation temperature exceeds this limit (~ 500 °C) [26]. The temperature-dependent phonon frequencies are calculated using Eq. (2.3) with the experimentally extracted fitting parameters [25]. Figure 2.4 shows the temperature dependence of the phonon frequencies of $E_1(\text{LO})$, $A_1(\text{LO})$, $E_1(\text{TO})$, and $A_1(\text{TO})$. For the optical dielectric constant ϵ^∞ , the temperature dependency is derived based on the temperature-dependent refractive index n measurement [27]. Using the relationship between the two constants $\epsilon^\infty = n^2$, we obtain

Table 2.1. Wurtzite GaN material constants for 300 and 800 K used in the numerical calculations.

Material Constants	Symbols	at 300 K	at 800 K
$A_1(\text{LO})$ phonon frequency (cm^{-1})	ω_{zL}	735	720
$A_1(\text{TO})$ phonon frequency (cm^{-1})	ω_{zT}	534	527
$E_1(\text{LO})$ phonon frequency (cm^{-1})	$\omega_{\perp L}$	743	727
$E_1(\text{TO})$ phonon frequency (cm^{-1})	$\omega_{\perp T}$	561	553
Static dielectric constant along z -axis	ϵ_z^0	10.12	10.02
Static dielectric constant perpendicular to z -axis	ϵ_{\perp}^0	9.38	9.30
Optical dielectric constant along z -axis	ϵ_z^∞	5.35	5.38
Optical dielectric constant perpendicular to z -axis	ϵ_{\perp}^∞	5.35	5.38
Electron conduction effective mass	m^*	0.22 m_0	
Electron density of states (DOS) effective mass	m_{DOS}^*	1.5 m_0	

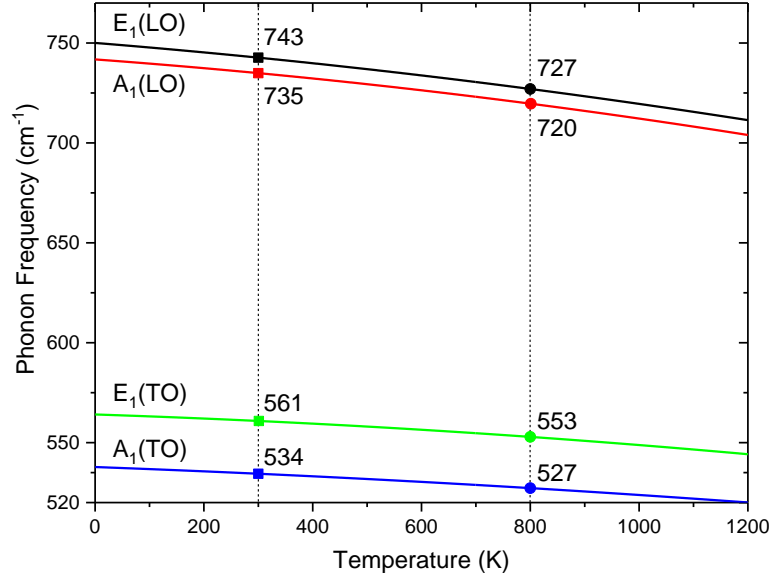


Figure 2.4. The phonon frequencies of $E_1(\text{LO})$, $A_1(\text{LO})$, $E_1(\text{TO})$, and $A_1(\text{TO})$ plotted as a function of temperature. Temperature dependence is calculated using Eq. (2.3). Coefficients α and β are set according to Ref. [25].

$$\varepsilon^\infty = \exp(5.2 \times 10^{-5} T) + \gamma \quad (2.4)$$

where γ is a fitting parameter set as $\gamma = 4.334$ to match the room temperature value $\varepsilon^\infty = 5.35$ [28]

and assume the optical dielectric constant is isotropic [24], i.e., $\varepsilon^\infty = \varepsilon_z^\infty = \varepsilon_\perp^\infty$. The static dielectric

constants are calculated so that they satisfy the Lyddane-Sachs-Teller relation: $\varepsilon_z^0 = \varepsilon_z^\infty \omega_{zL}^2 / \omega_{zT}^2$

and $\varepsilon_\perp^0 = \varepsilon_\perp^\infty \omega_{\perp L}^2 / \omega_{\perp T}^2$.

The LO-like phonon mode frequency ω_{LO} and TO-like phonon mode frequency ω_{TO} and their corresponding phonon energies as a function of the angle θ for two different temperatures $T = 300$ K (solid lines) and 800 K (dashed lines) are calculated using Eqs. (1.1) and (1.2) and are shown in Figure 2.5. For both temperatures, the LO-like phonon mode frequency shows a weak variation upon the angle whereas the TO-like phonon mode frequency exhibits some anisotropy. For $T = 300$ K, the minimum LO-like phonon frequency is obtained at $\theta = 0$ as $\omega_{\text{LO}} = \omega_{zL} = 735 \text{ cm}^{-1}$ and corresponds to the LO phonon emission threshold energy of electron, 91.1 meV. On the other hand,

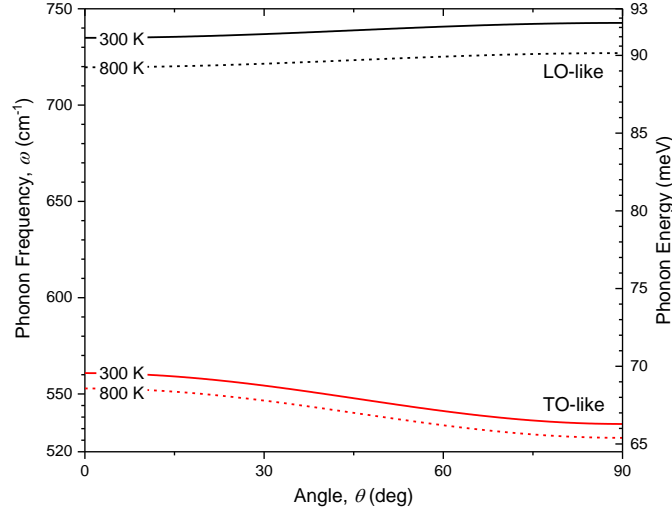


Figure 2.5. The LO-like and TO-like polar optical phonon frequencies and their corresponding energies as a function of the angle θ between the phonon wave vector and c -axis for temperatures 300 K (solid lines) and 800 K (dashed lines).

the minimum TO-like phonon frequency is obtained at $\theta = \pi/2$ as $\omega_{\text{TO}} = \omega_{\perp T} = 534 \text{ cm}^{-1}$ and corresponds to the TO phonon emission threshold energy of electron, 66.2 meV. For $T = 800 \text{ K}$, LO and TO phonon emission threshold energies decrease to 89.3 and 65.3 meV, respectively.

To understand how these angle θ variant optical phonons interact with electrons, we use the Fröhlich interaction Hamiltonian to describe the electric polarization (i.e., the relative displacement of positively and negatively charged ions) produced by the LO-like and TO-like polar optical phonons as [29]

$$\begin{aligned}
 H &= \sum_{\mathbf{q}} \left[\frac{4\pi e^2 \hbar V^{-1}}{\frac{\partial}{\partial \omega} [\varepsilon_{\perp}(\omega) \sin^2 \theta + \varepsilon_z(\omega) \cos^2 \theta]} \right]^{1/2} \frac{1}{q} e^{i\mathbf{q} \cdot \mathbf{r}} (a_{\mathbf{q}} + a_{-\mathbf{q}}^*) \\
 &= \sum_{\mathbf{q}} \sqrt{\frac{2\pi e^2 \hbar}{V \omega q^2}} \frac{(\omega_{\perp T}^2 - \omega^2)(\omega_{zT}^2 - \omega^2)}{\left[(\varepsilon_{\perp}^0 - \varepsilon_{\perp}^{\infty}) \omega_{\perp T}^2 (\omega_{zT}^2 - \omega^2)^2 \sin^2 \theta + (\varepsilon_z^0 - \varepsilon_z^{\infty}) \omega_{zT}^2 (\omega_{\perp T}^2 - \omega^2) \cos^2 \theta \right]^{1/2}} e^{i\mathbf{q} \cdot \mathbf{r}} (a_{\mathbf{q}} + a_{-\mathbf{q}}^*)
 \end{aligned} \tag{2.5}$$

where e is the elementary electron charge, V is the crystal volume, and $a_{-\mathbf{q}}^*$ and $a_{\mathbf{q}}$ are the creation and annihilation operators.

From this Fröhlich interaction Hamiltonian, the transition matrix element $M_{\mathbf{q}}$ may be written as

$$|M_{\mathbf{q}}|^2 = \frac{2\pi e^2 \hbar}{V \omega q^2} \left(n_{ph} + \frac{1}{2} \pm \frac{1}{2} \right) \frac{(\omega_{\perp T}^2 - \omega^2)^2 (\omega_{zT}^2 - \omega^2)^2}{(\varepsilon_{\perp}^0 - \varepsilon_{\perp}^{\infty}) \omega_{\perp T}^2 (\omega_{zT}^2 - \omega^2)^2 \sin^2 \theta + (\varepsilon_z^0 - \varepsilon_z^{\infty}) \omega_{zT}^2 (\omega_{\perp T}^2 - \omega^2)^2 \cos^2 \theta} \quad (2.6)$$

where n_{ph} is the phonon occupation number given by

$$n_{ph} = \frac{1}{e^{\hbar \omega / k_B T} - 1}. \quad (2.7)$$

Here, plane-wave electron states normalized in volume V are used to derive $M_{\mathbf{q}}$.

The probability of polar optical phonon induced electron scattering from electron state \mathbf{k} to \mathbf{k}' per unit time, $W(\mathbf{k}, \mathbf{k}')$, is calculated from the Fermi golden rule as

$$W(\mathbf{k}, \mathbf{k}') = \frac{2\pi}{\hbar} |M_{\mathbf{q}}|^2 \delta(E_{\mathbf{k}'} - E_{\mathbf{k}} \pm \hbar \omega) \quad (2.8)$$

where $E_{\mathbf{k}}$ and $E_{\mathbf{k}'}$ are the initial and final electron kinetic energy, respectively, and $\hbar \omega$ is the transferred phonon energy with the upper sign “+” (the lower sign “−”) corresponding to phonon emission (absorption). The electron kinetic energies are calculated assuming parabolic effective mass, i.e., $E_k = \hbar^2 k^2 / 2m^*$, where $m^* = 0.22m_0$ is the electron conduction effective mass and m_0 is the electron mass.

Then by plugging Eq. (2.6) into Eq. (2.8) and summing over all of the final electron states \mathbf{k}' , the total electron scattering rate due to the Fröhlich interaction can be obtained as [30]

$$\begin{aligned}
W(\mathbf{k}) = & \frac{e^2 \sqrt{m^*}}{2\sqrt{2}\pi\hbar} \int_0^{2\pi} d\phi \int_0^\pi \sin\theta d\theta \left(n_{ph} + \frac{1}{2} \pm \frac{1}{2} \right) \frac{\sigma \sqrt{E_{\mathbf{k}} \cos^2 \phi' \mp \hbar\omega}}{\left(\sqrt{E_{\mathbf{k}} \cos^2 \phi' \mp \hbar\omega} + \sqrt{E_0} \right)^2} \\
& \times \frac{1}{\omega \left(\varepsilon_\perp^0 - \varepsilon_\perp^\infty \right) \omega_{\perp T}^2 \left(\omega_{zT}^2 - \omega^2 \right)^2 \sin^2 \theta + \left(\varepsilon_z^0 - \varepsilon_z^\infty \right) \omega_{zT}^2 \left(\omega_{\perp T}^2 - \omega^2 \right)^2 \cos^2 \theta}
\end{aligned} \tag{2.9}$$

where m^* is the electron effective mass and ϕ' is the angle between the initial electron wave vector \mathbf{k} and the phonon wave vector \mathbf{q} , hence yielding $\cos \phi' = \sin \theta \sin \theta_k \cos \phi + \cos \theta \cos \theta_k$ such that θ_k is the angle between \mathbf{k} and the c -axis, and ϕ is the azimuthal angle between the wave vectors \mathbf{k} and \mathbf{q} . For the case of emission, σ is given as

$$\sigma = \begin{cases} 0 & \text{for } \cos^2 \phi' < \hbar\omega/E_{\mathbf{k}}, \\ 2 & \text{otherwise,} \end{cases} \tag{2.10}$$

and for absorption, $\sigma=1$. Here, a screening factor of $\sqrt{E_0} = 3 \times 10^{-11} \text{ eV}^{1/2}$ is included to facilitate efficient numerical integration in the case of emission when $E_{\mathbf{k}} \cos^2 \phi' \approx \hbar\omega$. The wave vectors and their angles with respect to the c -axis are depicted in Figure 2.3. We set the coordinate system

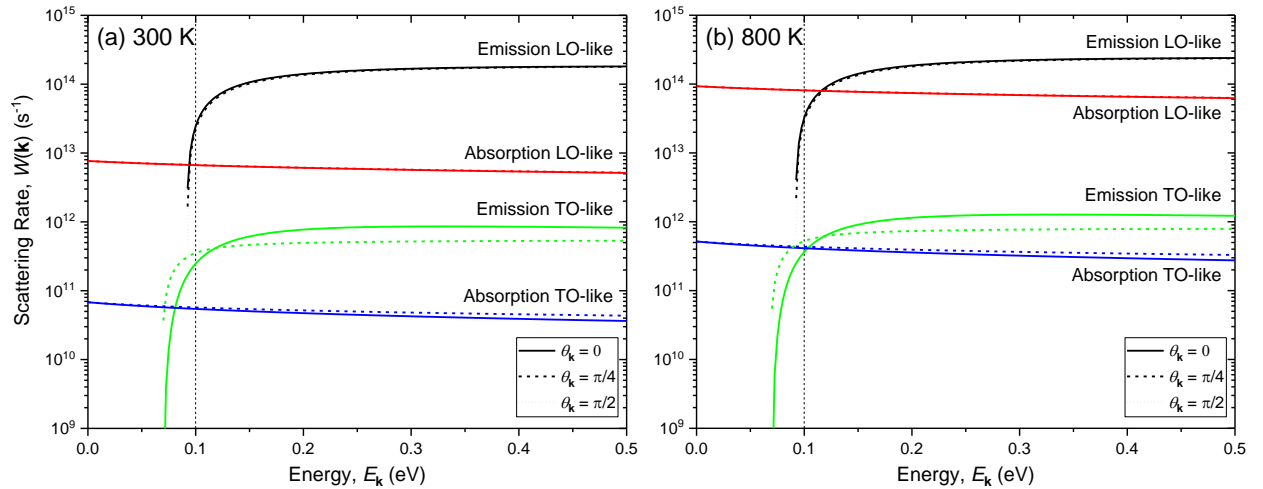


Figure 2.6. Electron scattering rates $W(\mathbf{k})$ due to emission and absorption of LO-like and TO-like phonon modes plotted as a function of electron initial energy $E_{\mathbf{k}}$ for two different temperatures (a) $T = 300 \text{ K}$ and (b) 800 K . The incident electron angles with respect to the c -axis are set to $\theta_k = 0$ (solid line), $\pi/4$ (dashed line), and $\pi/2$ (dotted line). The temperature affects the scattering rates through the temperature-dependent phonon frequencies and the phonon occupation number.

so that the initial electron wave vector is on the y - z plane with the z -axis aligned to the optical axis (c -axis). As long as the z -axis is aligned to the c -axis, the calculation results are invariant to how we set the x - and y -axes in the uniaxial model frame.

The electron–optical phonon scattering rates are numerically calculated using Eq. (2.9) and are plotted in Figure 2.6 for the two cases of (a) $T = 300$ K and (b) 800 K. The scattering rates due to the emission and absorption of LO-like and TO-like phonons are calculated separately as a function of incident electron energy $E_{\mathbf{k}}$ to show the contribution of each scattering process. The scattering rates for different electron incident angles $\theta_{\mathbf{k}} = 0$ (solid line), $\pi/4$ (dashed line), and $\pi/2$ (dotted line) are also shown together. The abrupt increase in the emission scattering rates occurs around the minimum LO-like and TO-like phonon energies, 91.1 and 66.2 meV at 300 K, and 89.3 and 65.3 meV at 800 K, respectively. For both cases of $T = 300$ and 800 K, the LO-like phonon mode scattering shows very weak $\theta_{\mathbf{k}}$ angle variance. The largest $\theta_{\mathbf{k}}$ angle variance is exhibited at the energy of onset of TO-like phonon emission (66.2 meV) as $\theta_{\mathbf{k}}$ varies from $\pi/4$ to $\pi/2$; though the results may differ depending on the numerical integration method or the value of the screening factor, according to my calculations, the TO-like phonon emission scattering rate of $\theta_{\mathbf{k}} = \pi/4$ is more than ten times larger than that of $\theta_{\mathbf{k}} = \pi/2$.

To make a clearer comparison of the extent of anisotropy of LO-like and TO-like mode phonon scattering rates, we plot them as a function of incident angle $\theta_{\mathbf{k}}$ for a fixed energy $E_{\mathbf{k}} = 0.1$ eV with $T = 300$ and 800 K in Figure 2.7. The absorption rates for both LO-like and TO-like modes show almost no anisotropy. The largest anisotropy is between the TO-like emission of $\theta_{\mathbf{k}} = 39^\circ$ and $\pi/2$ at 300 K; the rate at $\theta_{\mathbf{k}} = 39^\circ$ is 2.5 times larger than the rate at $\theta_{\mathbf{k}} = \pi/2$. Furthermore, at this electron energy, it is shown that the effect of increased temperature is quite significant.

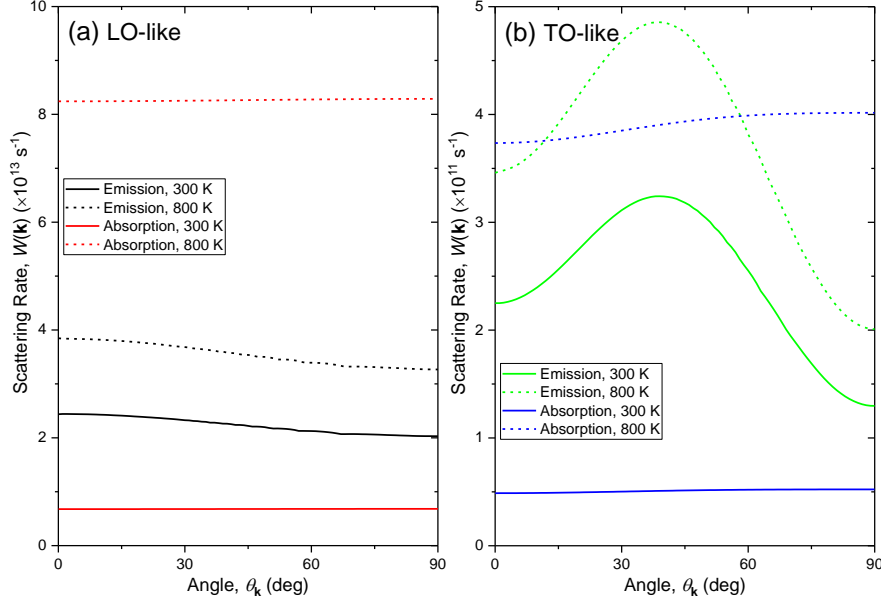


Figure 2.7. Electron scattering rates $W(\mathbf{k})$ due to (a) LO-like and (b) TO-like phonon modes plotted as a function of electron incident angle θ_k for a fixed electron initial energy $E_k = 0.1 \text{ eV}$. Solid lines and dashed lines represent scattering rates when the temperature is $T = 300$ and 800 K , respectively.

Combined with the discussion of Figure 2.6, the results of Figure 2.7 demonstrate that for elevated temperatures there is a large discrepancy between the emission threshold energy and the energy at which emission rates start to dominate over absorption rates. For example, at $T = 300 \text{ K}$ the LO-like emission scattering rate starts to exceed the LO-like absorption scattering rate around 93 meV which is only 2 meV higher than the emission threshold energy (91.1 meV). On the other hand, at $T = 800 \text{ K}$ this inversion occurs around 115 meV which is considerably higher than the emission threshold energy of 89.3 meV . Therefore, at higher temperatures, careful consideration must be given when assuming the onset energy of optical phonon emission is equal to the optical phonon energy itself.

The momentum relaxation of electrons in bulk wurtzite GaN is investigated by using the approach of weighing the scattering rate by the appropriate increase or decrease in momentum [17], [31]. That is, the absorption of a phonon traveling at an angle ϕ' to \mathbf{k} contributes to a fractional increase of momentum of $(q/k)\cos\phi'$ in the direction of \mathbf{k} . On the other hand, the emission of a phonon

contributes to a fractional decrease of momentum of $(q/k)\cos\phi'$ in the direction of \mathbf{k} . Thus, the momentum relaxation rate due to emission (upper signs) and absorption (lower signs) of optical phonons may be expressed as

$$\frac{1}{\tau_m} = \frac{2\pi}{\hbar} \sum_q \left(\mp \frac{q}{k} \cos\phi' \right) |M_q|^2 \delta(E_{\mathbf{k}'} - E_{\mathbf{k}} \pm \hbar\omega). \quad (2.11)$$

Based on Eq. (2.11) we obtain momentum relaxation rates due to phonon emission $1/\tau_m^e$ and absorption $1/\tau_m^a$:

$$\begin{aligned} \frac{1}{\tau_m^e} = & -\frac{e^2\sqrt{m^*}}{\sqrt{2\pi}\hbar} \int_0^{2\pi} d\phi \int_0^\pi \sin\theta d\theta (n_{ph} + 1) \frac{\cos^2\phi' \sqrt{E_{\mathbf{k}} \cos^2\phi' - \hbar\omega}}{\left(\sqrt{E_{\mathbf{k}} \cos^2\phi' - \hbar\omega} + \sqrt{E_0}\right)^2} \\ & \times \frac{1}{\omega \left(\varepsilon_\perp^0 - \varepsilon_\perp^\infty\right) \omega_\perp^2 \left(\omega_z^2 - \omega^2\right)^2 \sin^2\theta + \left(\varepsilon_z^0 - \varepsilon_z^\infty\right) \omega_z^2 \left(\omega_\perp^2 - \omega^2\right)^2 \cos^2\theta} \end{aligned} \quad (2.12)$$

$$\begin{aligned} \frac{1}{\tau_m^a} = & \frac{e^2\sqrt{m^*}}{2\sqrt{2\pi}\hbar} \int_0^{2\pi} d\phi \int_0^\pi \sin\theta d\theta (n_{ph}) \frac{-\cos^2\phi' + \cos\phi' \sqrt{\cos^2\phi' + \hbar\omega/E_{\mathbf{k}}}}{\sqrt{E_{\mathbf{k}} \cos^2\phi' + \hbar\omega}} \\ & \times \frac{1}{\omega \left(\varepsilon_\perp^0 - \varepsilon_\perp^\infty\right) \omega_\perp^2 \left(\omega_z^2 - \omega^2\right)^2 \sin^2\theta + \left(\varepsilon_z^0 - \varepsilon_z^\infty\right) \omega_z^2 \left(\omega_\perp^2 - \omega^2\right)^2 \cos^2\theta}. \end{aligned} \quad (2.13)$$

The momentum relaxation rates due to emission and absorption of optical phonons are numerically calculated using Eqs. (2.12) and (2.13), respectively, and their absolute values as a function of electron initial energy $E_{\mathbf{k}}$ are plotted in Figure 2.8 (a) for temperature $T = 300$ K. The LO-like and TO-like portions of the phonon emission and absorption process are calculated separately to see the contribution of each component. The incident electron angles are set to $\theta_{\mathbf{k}} = 0$ (solid line),

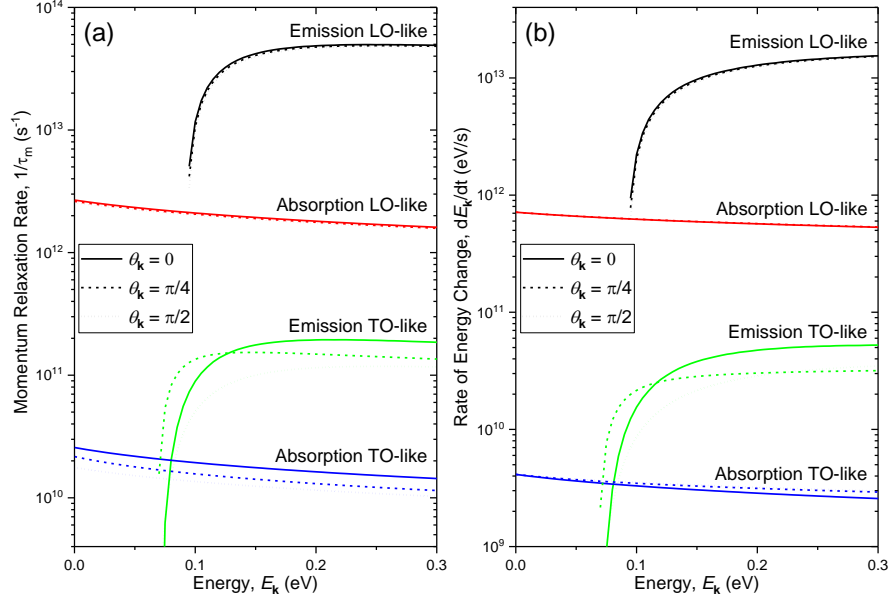


Figure 2.8. (a) Absolute value of the momentum relaxation rates $1/\tau_m$ and (b) the rate of energy change dE_k/dt due to emission and absorption of LO-like and TO-like phonons plotted as a function of electron initial energy E_k . The temperature is $T = 300$ K and the incident electron angles with respect to the c -axis are set to $\theta_k = 0$ (solid line), $\pi/4$ (dashed line), and $\pi/2$ (dotted line).

$\pi/4$ (dashed line), and $\pi/2$ (dotted line). The momentum relaxation rates due to LO-like modes are weakly dependent on the angle. In contrast, the rates due to TO-like modes show some anisotropy, especially near the emission threshold energy of $E_k = 66.2$ meV. The LO-like and TO-like momentum relaxation rates show more than two orders of magnitude difference. As mobility is proportional to the momentum relaxation time τ_m , the electron mobility is principally determined by interactions with LO-like phonons and the effect of the anisotropy shown in the relaxation rates with TO-like phonons is very small.

Through every optical phonon scattering event an electron undergoes, the energy of the electron changes. The Dirac delta function in Eq. (2.11) assures that after going through a scattering event the energy of the final electron state increases if the event was a phonon absorption process and decreases if it was a phonon emission. This energy change per unit time of electron can be directly associated with the saturation velocity as will be seen in the following section. To calculate the net

change of energy per unit time, we subtract the power loss due to phonon emission from the power gain due to phonon absorption as

$$\begin{aligned}
\frac{dE_{\mathbf{k}}}{dt} &= \hbar\omega(W^a(\mathbf{k}) - W^e(\mathbf{k})) \\
&= \frac{e^2\sqrt{m^*}}{2\sqrt{2}\pi} \int_0^{2\pi} d\phi \int_0^\pi \sin\theta d\theta \left[\frac{n_{ph}}{\sqrt{E_{\mathbf{k}} \cos^2 \phi' + \hbar\omega}} - \frac{2(n_{ph}+1)\sqrt{E_{\mathbf{k}} \cos^2 \phi' - \hbar\omega}}{(\sqrt{E_{\mathbf{k}} \cos^2 \phi' - \hbar\omega} + \sqrt{E_0})^2} \right] \\
&\quad \times \frac{(\omega_\perp^2 - \omega^2)^2 (\omega_z^2 - \omega^2)^2}{(\varepsilon_\perp^0 - \varepsilon_\perp^\infty) \omega_\perp^2 (\omega_z^2 - \omega^2)^2 \sin^2 \theta + (\varepsilon_z^0 - \varepsilon_z^\infty) \omega_z^2 (\omega_\perp^2 - \omega^2)^2 \cos^2 \theta}.
\end{aligned} \tag{2.14}$$

The numerical calculation results of Eq. (2.14) are shown in Figure 2.8 (b). The temperature is set to 300 K and the incident electron angles are set to $\theta_{\mathbf{k}} = 0$ (solid line), $\pi/4$ (dashed line), and $\pi/2$ (dotted line). The LO-like and TO-like portions of the phonon emission and absorption process are calculated separately to see the contribution of each component. Similar to the case of momentum relaxation rates, it is shown that scattering with the LO-like phonon is the dominant electron energy relaxation process. For electrons with high kinetic energy ($E_{\mathbf{k}} > 91.1$ meV), the power dissipated per electron through a scattering event saturates at a value of ~ 16 eV/ps.

2.3 Electron Mobility and Saturation Velocity

To investigate the temperature- and orientation-dependent electron mobility and saturation velocity, the standard mobility–momentum relaxation time relation and the electron energy balance equation [32] are used. In the literature, a two-step model [33], [34] which treats the absorption and almost immediate emission of a polar optical phonon as a single elastic process, is used for calculating mobility in GaN. However, in this work, we stick to the momentum relaxation

time approximation which is reasonably accurate while at the same time satisfying the purpose of illustrating the anisotropic electron–optical phonon interaction.

The electron mobility is given by

$$\mu = \frac{e \langle \tau_m \rangle}{m^*}. \quad (2.15)$$

The averaged electron momentum relaxation time over the electron distribution $\langle \tau_m \rangle$ is given by

$$\langle \tau_m \rangle = \frac{1}{N} \int_0^\infty \tau_m(E_{\mathbf{k}}) g_{3D}(E_{\mathbf{k}}) f_{FD}(E_{\mathbf{k}}) dE_{\mathbf{k}} \quad (2.16)$$

where the three-dimensional density of states (DOS) $g_{3D}(E_{\mathbf{k}})$ is given as

$$g_{3D}(E_{\mathbf{k}}) = \frac{(2m_{\text{DOS}}^*)^{3/2}}{2\pi^2 \hbar^3} \sqrt{E_{\mathbf{k}}} \quad (2.17)$$

and m_{DOS}^* is the electron density of states effective mass which is set to $m_{\text{DOS}}^* = 1.5m_0$. The Fermi-Dirac distribution is

$$f_{FD}(E_{\mathbf{k}}) = \left[\exp \frac{E_{\mathbf{k}} - E_F}{k_B T} + 1 \right]^{-1} \quad (2.18)$$

where E_F is the Fermi energy, and N is the spatial electron density. The momentum relaxation times for each of the four modes (LO-like emission, LO-like absorption, TO-like emission, and TO-like absorption) are calculated separately and used to derive the polar optical phonon limited mobility by applying Matthiessen's rule. The drift velocity is then obtained from $v_d = \mu F$ where F is the electric field. In this work, because only the electron scattering with polar optical phonons is considered, the electron concentration only affects the number of electrons considered over the electron distribution in the numerical calculation. Detailed description of models that account for

electron-density-dependent screening factors, electron-electron scattering or nonparabolicity of the electron dispersion relation can be found elsewhere [35], [36].

In order to calculate the saturation velocity, we relate the mobility to the power dissipated by optical phonon scattering. The net electron kinetic energy increase per second is the difference between the power gained from the electric field and the power loss from the scattering. When this net energy increase per unit time becomes zero, the drift velocity saturates to the saturation velocity. Thus, we may write as

$$e\mu F_{\text{sat}}^2 = \frac{dE_{\mathbf{k}}}{dt} \quad (2.19)$$

where F_{sat} is the electric field when the net power increase is equal to zero. From Figure 2.8 (b) it is shown that the net energy loss per second is a function of electron kinetic energy $E_{\mathbf{k}}$. Hence, after we obtain the saturation velocity as a function of kinetic energy, the saturation velocity is averaged over the electron distribution using

$$v_{\text{sat}} = \frac{1}{N} \int_0^\infty \frac{dE_{\mathbf{k}}}{dt} \frac{1}{eF_{\text{sat}}} g_{3D}(E_{\mathbf{k}}) f_{\text{FD}}(E_{\mathbf{k}}) dE_{\mathbf{k}}. \quad (2.20)$$

To predict the theoretical limit of electronic transport properties for different incident angles at elevated temperatures, we calculate the electron mobility and saturation velocity using Eqs. (2.19) and (2.20) with the momentum relaxation rate and the rate of energy change obtained from the previous section. Figure 2.9 shows the (a) electron mobility μ and (b) saturation velocity v_{sat} as a function of temperature. The incident electron angles with respect to the c -axis are set to $\theta_{\mathbf{k}} = 0$ (solid line), $\pi/4$ (dashed line), and $\pi/2$ (dotted line). The spatial electron concentration is fixed to $N = 5 \times 10^{18} \text{ cm}^{-3}$ in the temperature-dependent electron mobility and saturation velocity calculations. The maximum mobility for a given temperature is obtained when the incident angle

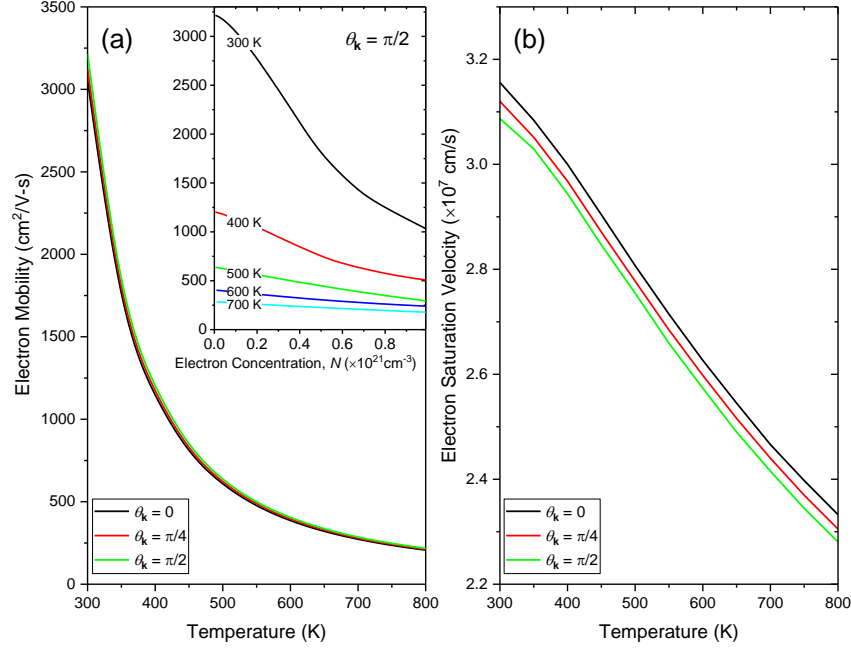


Figure 2.9. The effects of temperature on (a) electron mobility μ and (b) saturation velocity v_{sat} plotted for three different electron incident angles $\theta_k = 0, \pi/4$, and $\pi/2$. The spatial electron concentration is fixed to $N = 5 \times 10^{18}$ cm⁻³ in the temperature-dependent electron mobility and saturation velocity calculations. Inset of (a) shows electron mobility as a function of electron concentration for five different. The electron incident angle is fixed to $\theta_k = \pi/2$.

is $\theta_k = \pi/2$ and mobility decreases approximately $\sim 5\%$ as angle varies to $\theta_k = 0$. For all incident angles, the mobility rapidly drops from ~ 3100 cm²/V-s to ~ 200 cm²/V-s between 300 K and 800 K, falling with a power law of $T^{-3.1}$. The saturation velocity is the smallest for the angle $\theta_k = \pi/2$ and largest for $\theta_k = 0$ with a discrepancy of $\sim 2\%$. For both mobility and saturation velocity, the angle dependence is very weak, showing that the TO-like scattering anisotropy has little impact on the macroscopic electronic properties.

The electron mobilities for higher electron concentrations are also calculated for an angle set as $\theta_k = \pi/2$ and is plotted in the inset of Figure 2.9 (a). For all temperatures, the mobility decreases as the concentration increases. The effect of temperature increase on electron–phonon scattering rates reveals itself through the increased phonon occupation number, the decreased phonon

frequencies (as shown in Figure 2.4), and the dispersion of the Fermi-Dirac distribution. At a fixed concentration, as the temperature increases, more electrons with higher kinetic energy participate in the conduction; that is, electrons that are more likely to emit phonons than to absorb phonons contribute more to the average mobility. Thus, the mobility drops with the temperature increase. Apparently, the increase of phonon absorption rate associated with the increase of temperature is not enough to compensate for the effect of the increase in the number of electrons with higher energy.

2.4 Hotspot Size: Travel Distance of Electrons

Temperature increase critically influences the electrical performance of the device through mobility and saturation velocity degradation. In electronic devices, the temperature is never uniform throughout the whole device but increases more severely in regions where electrons go through intense scattering events. Electrons accelerated by the electric field, which carry a large amount of energy, would give up their energy to the lattice through scattering events leading to an increased temperature. For GaN high-electron-mobility transistors (HEMTs) this local high-temperature region or hotspot is located under the drain-side of the gate [37]. The dissipated power H may be calculated by

$$H = \mathbf{J} \cdot \mathbf{E} \quad (2.21)$$

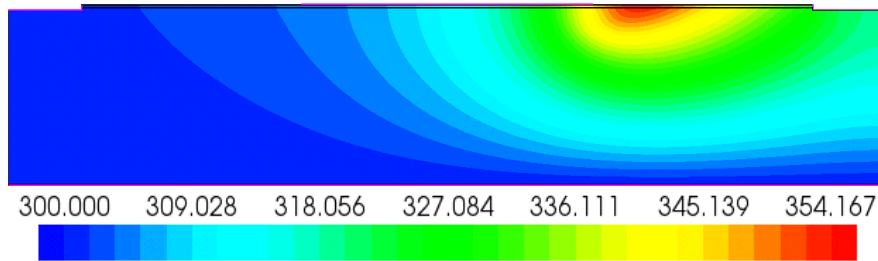


Figure 2.10. Finite element method simulation result showing the position and temperature of the hotspot in a GaN HEMT. The bias conditions used for the simulation are $V_G = 0$ V and $V_D = 50$ V. Simulation is done using TCAD Synopsys Sentaurus.

where \mathbf{J} is the current density and \mathbf{E} is the electric field. A TCAD simulation result depicting the position and temperature of the hotspot is shown in Figure 2.10. The device consists of $\text{Al}_{0.25}\text{Ga}_{0.75}\text{N}$ layer on top of a GaN layer. The AlGa N layer is 21-nm-thick and the GaN layer is 1.2- μm -thick. The contacts are shown as pink films at the top of the structure. The leftmost contact is the source, the rightmost one is the drain, and the one in the middle is the gate contact. In this simulation, the bias conditions are $V_G = 0 \text{ V}$ and $V_D = 50 \text{ V}$. The temperature of the hotspot was 354.2 K and located at the edge of the drain-side of the gate.

To study the fundamental factors that determine the hotspot size, the distance that energetic electrons travel while going through these scattering events is computed. Ideally, the exact location of the hotspot and the energy released to the lattice may be simulated by more sophisticated tools such as the Monte Carlo method or *ab initio* dynamics simulations. Here, the hotspot size is estimated assuming somewhat exaggerated conditions:

- a) All electrons start to traverse at the same starting point.
- b) Electrons only move forward.
- c) Only LO-like phonon scattering events are considered.
- d) Electric-field is fixed to a moderate value through the whole region.
- e) Lattice temperature is fixed to 300 K.
- f) Energy distribution of the electrons is initialized uniformly over the entire energy range; that is, we have one electron for each energy with a resolution of 1 meV.
- g) Each electron experiences 12 scattering events.
- h) Electrons can either release or gain energy via scattering events depending on their energy right before the event.
- i) No interaction between electrons.

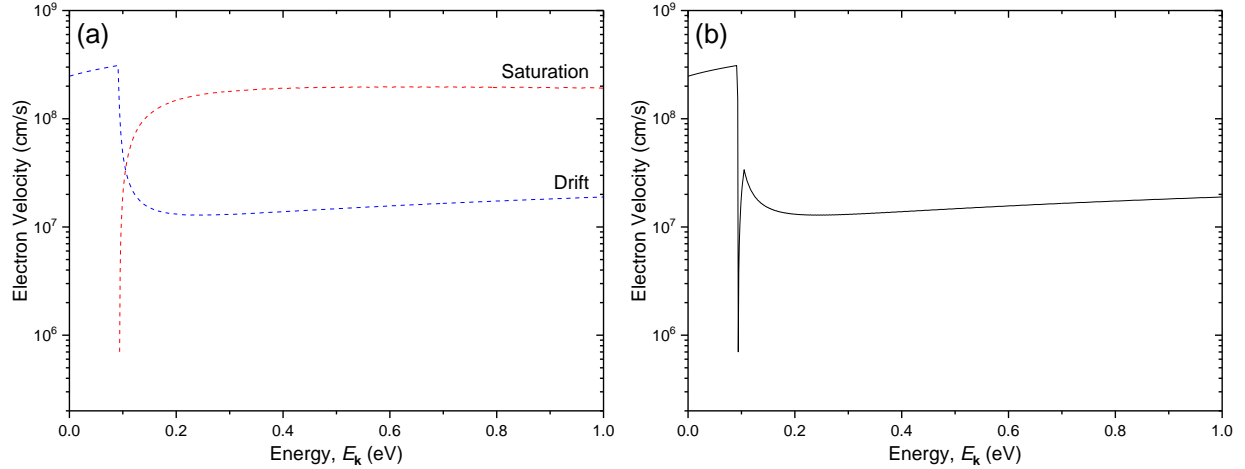


Figure 2.11. (a) Comparison of saturation velocity and drift velocity and (b) the minimum velocity of the two are shown as a function of the initial energy of the electron. Saturation velocity and drift velocity are calculated based on energy relaxation rates and momentum relaxation rates. We take the smaller value to be the electron velocity at that energy.

Figure 2.11 shows the energy-dependent electron velocity. The saturation velocity and drift velocity in Figure 2.11 (a) are compared and the minimum value is taken to be the electron velocity for the given electron initial energy as shown in Figure 2.11 (b). The saturation velocity is calculated based on the energy relaxation rates of Eq. (2.20), but without performing the integration to obtain the energy-dependent velocity. Similarly, the drift velocity is calculated based on the momentum relaxation rates of Eq. (2.16), but without averaging the mobility over the entire electron distribution. As the drift velocity is an electric field dependent quality, it is assumed that a moderate level of field is applied to the electrons.

To estimate the hotspot size, Figure 2.11 (b) is combined with the LO-like phonon scattering rates. Figure 2.12 shows a transport scenario of an electron with initial energy of 0.4 eV. The electron velocity is shown in Figure 2.12 (a) and the scattering rate is shown in Figure 2.12 (b) with the scattering events labeled sequentially as 1 through 5 on top of the figures. First, the electron will travel with the velocity at point 1 until it scatters and loses an energy of 91 meV to arrive at point 2. The distance the electron travels up to this point is computed by multiplying the velocity with

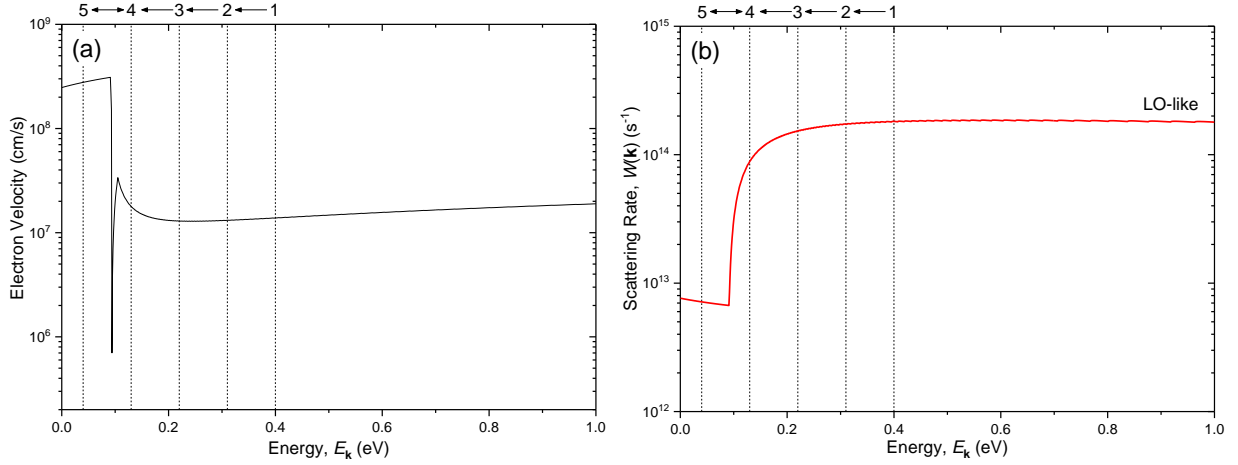


Figure 2.12. (a) Electron velocity and (b) LO-like phonon scattering rate are combined to show the transport scenario of an electron with initial energy of 0.4 eV. As the electron traverses through the channel, it releases energy and relaxes to the energy labeled as 5. At the point 5, the electron no longer has enough energy to emit LO phonons and thus absorbs energy to arrive at the point 4, and repeats emission and absorption.

the reciprocal of the scattering rate. As the electron continues to travel and scatter from 2 through 5, it releases three LO-like phonons (273 meV) to arrive at point 5 where the electron no longer has enough energy to emit an LO-like phonon (i.e., $E_k < 91$ meV). Thus, the electron rather absorbs an LO-like phonon to climb up to point 4 again. Henceforth, the electron moves back and forth between points 4 and 5, absorbing and emitting phonons. Applying this procedure to all electrons with an initial energy less than 1 eV with a resolution of 1 meV, the amount of energy that was released throughout a one-dimensional grid can be plotted.

The amount of released energy along the one-dimensional grid is plotted in Figure 2.13. Here, to better illustrate the hotspot size, the grid is divided into 1-nm-length *bins*. For instance, the total amount of energy that was released from the electrons within the grid $1.5 \text{ nm} < x < 2.49 \text{ nm}$ were all dumped to the bin at $x = 2 \text{ nm}$, and so on. The result shows that most of the energy is released within 20 nm from the starting point at $x = 0$. The release of most of the energy in such a small (or short) region is attributed to the combination of scattering rate and electron velocity which was shown in Figure 2.12. Electrons that have enough energy to emit phonons have a velocity of $\sim 10^7$

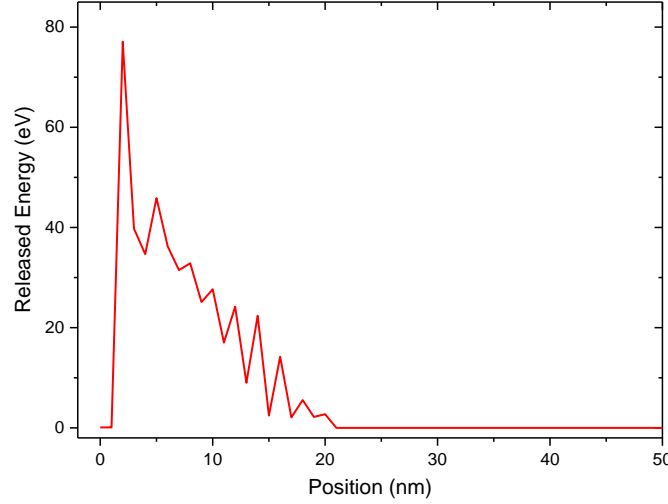


Figure 2.13. Released energy plotted as a function of position to estimate the hotspot size. Most of the electrons' energy is dumped within 20 nm of the starting point. Energy released beyond 50 nm in the one-dimensional grid is omitted.

cm/s and a scattering rate of $\sim 10^{14} \text{ s}^{-1}$. These electrons travel a distance of about 10^{-7} cm , or 1 nm, before undergoing a phonon emission process. On the other hand, electrons with smaller energy that can only absorb phonons travel a few hundreds of nanometers before they can scatter. Due to this large difference, electrons with small energy have almost no impact on the hotspot size. Therefore, even if the electrons can travel towards the second-dimension and backscatter or move back and forth, as long as the electron velocity and scattering rate are in the order of 10^7 cm/s and 10^{14} s^{-1} , respectively, we can roughly estimate that the hotspot to be a few tens of nanometers.

2.5 Conclusion

In conclusion, we have developed a theory of scattering rates, momentum relaxation rates, and rate of energy change due to electron interaction with polar optical phonons in bulk wurtzite GaN based on the dielectric continuum model and the uniaxial model. These rates are calculated numerically and are used to extract temperature and orientation dependent electron mobility and saturation velocity. The results show that the electron–optical phonon interactions rely more on electron incident angle in TO-like phonon modes than in LO-like phonon modes and that LO-like phonon

modes are mostly independent of angle variance. The polar optical phonon limited mobility and saturation velocity show a 5% variance with the orientation mostly due to the anisotropy in LO-like phonon scattering rates. We report that the macroscopic electronic properties such as the mobility and saturation velocity are predominantly determined by LO-like phonon interactions. The strong anisotropy in TO-like phonon scattering rates can be ignored in these calculations because of the two orders of magnitude difference compared to LO-like phonon scattering rates. Using the scattering rates, mobility, and saturation velocity we calculate the hotspot size to be roughly 20 nm.

CHAPTER 3 ELECTRON SCATTERING VIA INTERFACE OPTICAL PHONONS WITH HIGH GROUP VELOCITY IN WURTZITE GaN-BASED QUANTUM WELL HETEROSTRUCTURES

Parts of this chapter are reproduced from [38], with the permission of Springer Nature.

This chapter presents a detailed theoretical analysis of the interaction between electrons and optical phonons of interface and confined modes in a wurtzite AlN/GaN/AlN quantum well heterostructure based on the uniaxial dielectric continuum model. The formalisms describing the interface and confined mode optical phonon dispersion relation, electron–phonon scattering rates, and average group velocity of emitted optical phonons are developed and numerically calculated. The dispersion relation of the interface phonons shows a convergence to the resonant phonon frequencies 577.8 and 832.3 cm^{-1} with a steep slope around the zone center indicating a large group velocity. At the onset of interface phonon emission, the average group velocity is small due to the large contribution of interface and confined mode phonons with close-to-zero group velocity, but eventually increases up to larger values than the bulk GaN acoustic phonon velocity along the wurtzite crystal *c*-axis (8 nm/ps). By adjusting the GaN thickness in the double heterostructure, the average group velocity can be engineered to become larger than the velocity of acoustic phonons at a specific electron energy. This suggests that the high group velocity interface mode optical phonons can be exploited to remove heat more effectively and reduce junction temperatures in GaN-based heterostructures.

3.1 Introduction

GaN-based semiconductors are of great interest in the electronics and optoelectronics communities because they possess large electronic bandgaps (3.4 eV) suitable for fabricating semiconductor

lasers with wavelengths in blue and ultraviolet [39] as well as electronic devices designed to tolerate high electric fields (3.3 MV/cm) and elevated operating temperatures (700 °C) [40]. In particular, AlGaIn/GaN high-electron-mobility transistors (HEMTs) are among the most promising devices for high-power applications [8]. The spontaneous and piezoelectric polarization fields of this heterostructure allow the GaN layer to form a high-density electron channel through which electrons can flow with high saturation velocity (2.5×10^7 cm/s); this is partly due to the optical phonons with high energy ($\hbar\omega_{LO} = 92$ meV) in GaN [36]. The electron velocity saturation occurs with the onset of emission of these optical phonons and therefore their energy roughly determines the electron saturation velocity according to $v_0 \approx [\hbar\omega_{LO}/m]^{1/2}$, where m is the effective electron mass. Taking a closer look into the material, the large mismatch between the cation and anion masses causes a large splitting between the energies of the optical and acoustic phonon branches which raises the energy of optical phonons [41]. The drawback associated with these high-energy optical phonons is their short interaction time with electrons compared to the long-decay time into acoustic phonons. As in common semiconductors, heat in GaN is carried mainly by the long wavelength acoustic phonons [42]. To remove the excessive heat that is generated in the electron channel by the collision of hot electrons and the lattice (at the rate of ~ 10 THz) [7], the non-equilibrium optical phonons (whose propagation velocity is close to zero) must decay into acoustic phonons. The process is known as the Ridley process [43] and the decay time is reported to be ~ 5 ps which is much longer than the electron interaction time of ~ 9 fs [44]. This mismatch between the optical phonon generation rate and the relaxation rate into acoustic phonons results in a large accumulation of optical phonons in a localized region at the channel and eventually causes the electronic properties to degrade [45], [46].

In this chapter, we propose a novel phonon engineering technique that portends applications related to reducing the maximum temperature of the localized hotspot in GaN-based devices. To enhance the heat dissipation efficiency, a double heterostructure consisting of AlN/GaN/AlN is introduced to exploit properties of the interface mode optical phonons. Unlike bulk optical phonons, the mixing between available phonon frequencies of AlN and GaN induces an optical phonon mode that possesses a high propagation velocity at the heterointerface. The existence of these optical phonon modes has been corroborated by Raman studies on AlN/GaN superlattices [47], [48]. The introduction of these interface mode phonons provides an extra channel through which heat can be removed. Here, the uniaxial dielectric continuum model is employed to theoretically examine the properties of interface and confined mode optical phonons and their interaction with hot electrons.

3.2 Optical Phonon Mode Dispersion in Wurtzite Crystals

In the double heterostructure of interest in this work, which is a GaN quantum well sandwiched by two AlN layers (AlN/GaN/AlN), there exist four distinct classes of optical phonon modes: the interface, confined, half-space, and propagating modes [49]. Among these four optical phonon modes, the electrons that are confined in the GaN quantum well mostly interact with the interface and confined phonons; the effect of the half-space and propagating modes on the electrons is negligible in this system [50]. Here, therefore, we only consider the electron scattering with interface and confined mode optical phonons.

In a heterostructure configuration, the available optical phonon modes and the phonon frequencies for each mode are determined by the relation between the dielectric constant functions. The

frequency-dependent dielectric functions parallel (ε_z) and perpendicular (ε_t) to the z -axis are given as [29]:

$$\varepsilon_z(\omega) = \varepsilon_z^\infty \frac{\omega^2 - \omega_{Lz}^2}{\omega^2 - \omega_z^2} \quad (3.1)$$

$$\varepsilon_t(\omega) = \varepsilon_t^\infty \frac{\omega^2 - \omega_{Lt}^2}{\omega^2 - \omega_t^2} \quad (3.2)$$

where ω is the phonon frequency, and ω_{Lz} , ω_z , ω_{Lt} , and ω_t are the characteristic frequencies of $A_1(\text{LO: longitudinal-optical})$, $A_1(\text{TO: transverse-optical})$, $E_1(\text{LO})$, and $E_1(\text{TO})$ optical phonon modes, respectively. For the AlN/GaN/AlN quantum well, two sets of material parameters are required such that we obtain four dielectric functions, namely ε_{1z} , ε_{1t} , ε_{2z} , and ε_{2t} , where the subscripts 1 and 2 indicate the GaN and AlN, respectively. With $\omega = 0$, the Lyddane-Sachs-Teller relation is recovered and the static dielectric constants are obtained. Throughout this chapter, the z -axis is taken to be along the c -axis of the wurtzite crystal [0001] and perpendicular to the heterointerfaces.

The phonon frequencies and dielectric constants for bulk GaN and AlN used in the calculations are listed in Table 3.1 [51], [52]. Using these frequency-dependent dielectric functions of bulk GaN and AlN, the phonon frequencies and available phonon modes of the AlN/GaN/AlN quantum well are deduced by the dielectric continuum model. Notice that the phonon frequencies are listed in units of cm^{-1} . In the following calculations, whenever appropriate, they are converted into units of s^{-1} . It is also assumed that the two high-frequency dielectric constants are identical, i.e., $\varepsilon_z^\infty = \varepsilon_t^\infty = \varepsilon^\infty$ [24].

Table 3.1. Material constants used in the numerical calculations.

Material Constants	Symbols	GaN	AlN
$A_1(\text{TO})$ phonon frequency ^a	ω_z (cm ⁻¹)	531	611
$E_1(\text{TO})$ phonon frequency ^a	ω_t (cm ⁻¹)	559	671
$A_1(\text{LO})$ phonon frequency ^a	ω_{Lz} (cm ⁻¹)	734	890
$E_1(\text{LO})$ phonon frequency ^a	ω_{Lt} (cm ⁻¹)	741	912
High-frequency dielectric constant ^b	ϵ^∞	5.35	4.77

^a Phonon frequencies taken from Ref. [51].

^b Dielectric constants taken from Ref. [52].

The conditions imposed on the available interface mode optical phonon frequency are

$$\epsilon_{1z}\epsilon_{1t} > 0, \epsilon_{2z}\epsilon_{2t} > 0, \text{ and } \epsilon_{1z}\epsilon_{2z} < 0. \quad (3.3)$$

For confined modes, the conditions are

$$\epsilon_{1z}\epsilon_{1t} < 0 \text{ and } \epsilon_{2z}\epsilon_{2t} > 0. \quad (3.4)$$

To clearly illustrate the available range of phonon frequencies for each mode, the four dielectric constants as a function of phonon frequency are shown in Figure 3.1. The characteristic frequencies of the dielectric functions which define the phonon frequency ranges are indicated by vertical dashed lines. According to the conditions in Eq. (3.3), the interface phonons are allowed in two phonon frequency intervals, $(\omega_{1t}, \omega_{2z})$ and $(\omega_{1Lz}, \omega_{2Lt})$. Since the former (latter) interval corresponds to the TO (LO) phonon frequencies of GaN and AlN, we label the phonon modes that lie in this frequency range as TO (LO) interface phonons. These intervals are indicated in the figure as red and blue shaded regions, respectively. Similarly, according to the conditions in Eq. (3.4), the confined phonons are allowed in two phonon frequency intervals, $(\omega_{1z}, \omega_{1t})$ and $(\omega_{1Lz}, \omega_{1Lt})$. The characteristic phonon frequencies associated with these intervals are from the TO and LO phonon frequencies of GaN, and hence we label them as TO confined and LO confined phonons.

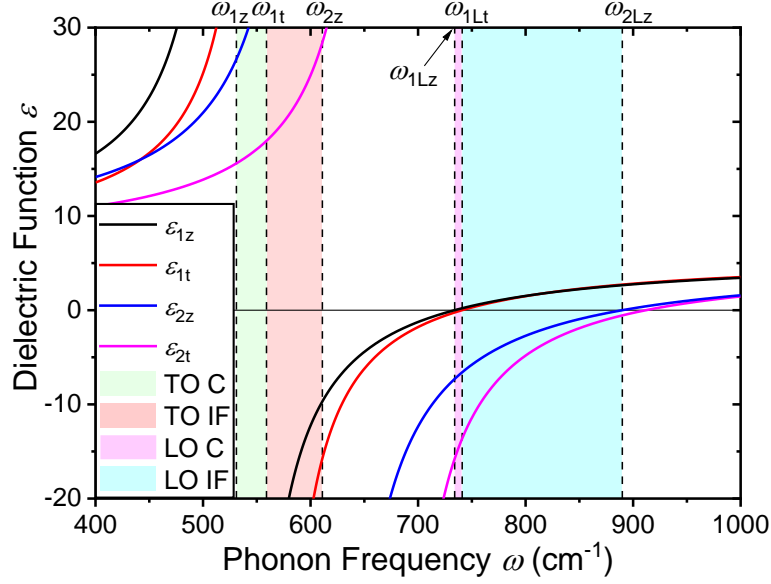


Figure 3.1. Dielectric constants as a function of phonon frequency. The characteristic frequencies of the dielectric functions which define the range of available interface (IF) and confined (C) mode phonon frequencies are indicated by vertical dashed lines. The region shaded in red (ω_{1t} , ω_{2z}) is where the interface phonons associated with the TO phonon modes of bulk GaN and AlN are defined. The region shaded in blue (ω_{1Lt} , ω_{2Lz}) is where the interface phonons associated with the LO phonon modes of bulk GaN and AlN are defined. The regions shaded in green (ω_{1z} , ω_{1t}) and magenta (ω_{1Lz} , ω_{1Lt}) are where the confined phonons are defined.

The TO and LO confined phonon frequency ranges are shown in the figure as green and magenta shaded regions, respectively.

3.2.1 Interface modes

The dispersion relations for the symmetric q_s^{IF} and asymmetric q_a^{IF} interface phonon modes are described by [53]

$$q_s^{\text{IF}} = \frac{1}{2\alpha d} \ln \left[\frac{\xi_1 + \xi_2}{\xi_1 - \xi_2} \right] \quad (3.5)$$

$$q_a^{\text{IF}} = \frac{1}{2\alpha d} \ln \left[\frac{\xi_1 + \xi_2}{\xi_2 - \xi_1} \right] \quad (3.6)$$

where $\alpha = \frac{1}{2} \sqrt{|\varepsilon_{1t}(\omega)/\varepsilon_{1z}(\omega)|}$, $\xi_1 = \sqrt{|\varepsilon_{1z}(\omega)\varepsilon_{1t}(\omega)|}$, $\xi_2 = \sqrt{|\varepsilon_{2z}(\omega)\varepsilon_{2t}(\omega)|}$, and d is the quantum well thickness. The GaN quantum well thickness d is set to a default value of 5 nm in the following calculations unless otherwise specified. The phonon wave vectors q_s^{IF} and q_A^{IF} must be real and positive, which implies that symmetric and asymmetric modes are distinguished based on the polarity of $\xi_1 - \xi_2$.

The resonant interface phonon frequency is obtained from $\xi_1 = \xi_2$. The $\omega_{\text{TO,res}}$ and $\omega_{\text{LO,res}}$ are the TO and LO resonant interface frequencies where ξ_1 and ξ_2 are equal in the TO and LO phonon frequency range, respectively. These frequencies are calculated as $\omega_{\text{TO,res}} = 577.8 \text{ cm}^{-1}$ and $\omega_{\text{LO,res}} = 832.3 \text{ cm}^{-1}$. From the definition of the symmetric and asymmetric phonon wave vectors, the symmetric mode is only defined in the frequency range where $\xi_1 > \xi_2$ and the asymmetric mode is only defined in the range where $\xi_1 < \xi_2$. Combined with the constraints of the dielectric constants, the symmetric TO interface modes can only be defined in the phonon frequency range $(\omega_{1t}, \omega_{\text{TO,res}})$ and the symmetric LO modes in the range $(\omega_{\text{LO,res}}, \omega_{2Lz})$. Similarly, the asymmetric TO interface phonons are only defined in $(\omega_{\text{TO,res}}, \omega_{2z})$ and the asymmetric LO modes in $(\omega_{1Lt}, \omega_{\text{LO,res}})$.

3.2.2 Confined modes

The dispersion relations for the symmetric q_s^C and asymmetric q_A^C confined phonon modes are described by [29], [53]

$$q_s^C = \frac{1}{\alpha d} \left[n\pi + \mu \arctan \frac{\xi_2}{\xi_1} \right]$$

$$n = 1, 2, 3 \dots \text{ and } 0 \text{ if } \mu = 1 \quad (3.7)$$

$$q_A^C = \frac{1}{\alpha d} \left[n\pi - \mu \arctan \frac{\xi_1}{\xi_2} \right]$$

$$n = 1, 2, 3 \dots \text{ and } 0 \text{ if } \mu = -1 \quad (3.8)$$

where $\mu = \text{sign} [\varepsilon_{1z}(\omega)\varepsilon_{2z}(\omega)]$ and n is the quantum number for symmetric and asymmetric confined modes.

The interface and confined mode phonon dispersion relations [Eqs. (3.5) – (3.8)] are shown in Figure 3.2. The subscripts A and S indicate asymmetric and symmetric modes, and superscripts IF and C indicate interface and confined modes, respectively. The low-frequency modes that are associated with the TO phonon frequencies of GaN and AlN are plotted in (a) and the high-frequency modes that are associated with the LO phonon frequencies are plotted in (b). The symmetric modes are shown in dashed lines and asymmetric modes are shown in solid lines for both interface and confined phonons. The characteristic phonon frequencies, which separate the interface modes from the confined modes, and resonant interface phonon frequencies are indicated with horizontal lines. In terms of phonon energy, the LO interface phonon modes ($91.9 < \hbar\omega_{LO}^{IF} < 110.3$ eV) are higher in energy than the TO phonon modes ($69.3 < \hbar\omega_{TO}^{IF} < 75.8$ eV). The TO and LO resonant interface phonon energies are 71.7 and 103.2 meV, respectively. Compared to interface phonon modes, more than a pair of symmetric and asymmetric confined modes exist in each phonon frequency interval. Here, we plot only the two symmetric and the two asymmetric confined modes that contribute most to the electron–phonon scattering process. However, in principle, there is an infinite number of modes available. It should be noted that for the confined modes, the dispersion curves asymptotically approach a characteristic phonon frequency of GaN

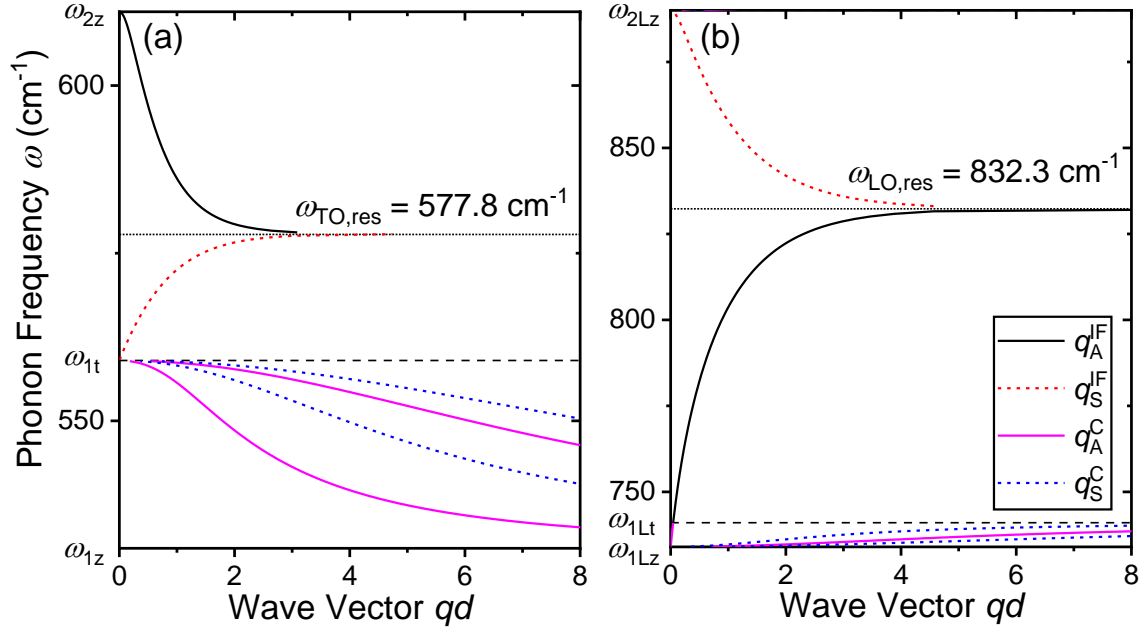


Figure 3.2. Dispersion relation of asymmetric interface (q_A^{IF}), symmetric interface (q_S^{IF}), asymmetric confined (q_A^{C}), and symmetric confined (q_S^{C}) mode phonons of the AlN/GaN/AlN quantum well in the (a) low-frequency and (b) high-frequency region. Only a few of the confined mode phonons (two modes each for the asymmetric and symmetric branch with lowest quantum numbers) are plotted. Phonon modes associated with TO phonon modes of AlN and GaN are shown in the lower frequency region (a), whereas those associated with LO phonon modes are in the higher frequency region (b). The interface phonon resonant frequencies are shown in dotted horizontal lines and the other characteristic frequencies are shown in dashed horizontal lines. The x -axis is shown in the dimensionless wave vector qd .

(i.e., ω_{1z} for TO confined modes and ω_{1Lt} for LO confined modes), whereas for the interface modes the curves approach the resonant frequency with increasing wave vector. This interface phonon dispersion relation gives rise to a phonon emission threshold energy in the electron–phonon scattering process that does not correspond to an energy of the characteristic phonons of either AlN or GaN.

Another important feature in the dispersion relation is that these interface phonon modes have a nonzero slope at the zone center. This indicates that the group velocity $v_g = d\omega/dq$ is nonzero and that optical phonons generated at the interface will not stay where they were generated (as bulk optical phonons do) but will propagate along the interface. Notice that the x -axis is set to the

dimensionless product of phonon wave vector q and the quantum well thickness d . Therefore, the group velocity will increase with increasing quantum well thickness due to the stronger dispersion.

3.3 Electron-Phonon Scattering Rate

To investigate the electron scattering rate with confined and interface mode phonons, we adapt the expression from Ref. [49]:

$$\frac{1}{\tau_e^{(a)}} = \pm \frac{2me_0^2}{\hbar^2} \sum_n \int_{\omega_1}^{\omega_2} \frac{\left\{ N(\omega) + \frac{1}{2} \mp \frac{1}{2} \right\} D(q, \omega) \sigma \left[\left\{ \frac{\omega}{q^2} \pm \frac{\hbar}{2m} \right\} \frac{dq}{d\omega} - \frac{1}{q} \right]}{\left[\frac{q}{2} \pm \frac{m}{\hbar} \left\{ \frac{\omega}{q} - \frac{d\omega}{dq} \right\} \right] \sqrt{\frac{1}{m} \chi(\mathbf{k}, q, \omega)}} d\omega \quad (3.9)$$

with

$$\chi(\mathbf{k}, q, \omega) = \frac{\hbar^2 \mathbf{k}^2}{m} - \frac{\hbar^2 q^2}{4m} \pm \hbar \omega - m \frac{d\omega}{dq} \quad (3.10)$$

$$\sigma = \begin{cases} 0 & \text{for } \chi(\mathbf{k}, q, \omega) < 0 \\ 1 & \text{otherwise} \end{cases} \quad (3.11)$$

where $m = m^* m_0$, the dimensionless effective mass is $m^* = 0.22$, m_0 is the electron rest mass, e_0 is the elementary charge, and $N(\omega) = [e^{\hbar\omega/k_B T} - 1]^{-1}$ is the phonon occupation number. The upper (lower) signs are taken when considering electron absorption (emission) scattering process. The summation over the quantum number n [identical to those in Eqs. (3.7) and (3.8)] is included to consider scattering with all possible symmetric and asymmetric confined mode phonons. For each n , the proper dispersion relation between q and ω should be imposed through Eqs. (3.7) or (3.8). In the numerical calculation of the scattering rates, a practical number for the upper limit is $n = 5$; contributions to the electron-phonon scattering rate from confined modes with n larger than 5 are

negligible. Also, the symmetric and asymmetric confined modes must be considered separately as the dispersion relations are different. For the case of interface modes, the summation is omitted because only one interface mode exists in a given range of phonon frequency $[\omega_1, \omega_2]$.

In the original formula [50], where the integral is assessed over the angle θ between the phonon wave vector q and the optical axis c , the lower and upper limits of the integral are set to $\theta = 0$ and 2π . In order to separately calculate the matrix elements of the Fermi golden rule for each phonon mode of uniaxial wurtzite crystals, the formula with the integral over θ is transformed into Eq. (3.9) where the integral is over ω . Considering the energy and momentum conservation of the electron–phonon scattering process, the limits of the integral over ω may also be transformed according to the relations:

$$\cos \theta = \begin{cases} \frac{m\omega}{kq\hbar} - \frac{q}{2k} & \text{for absorption} \\ \frac{m\omega}{kq\hbar} + \frac{q}{2k} & \text{for emission} \end{cases} \quad (3.12)$$

where $k = |\mathbf{k}|$. However, given that q is also a complex function of ω with different dispersion relations for different phonon modes [Eqs. (3.5) – (3.8)] and that the integral must be calculated for different electron energies $E_{\mathbf{k}} = \hbar^2 \mathbf{k}^2 / 2m$, it is impractical to solve the nonlinear equation. Alternatively, a conditional variable σ is included to take into account the relation Eq. (3.12). Since the implications of the argument inside the square root of the denominator of Eq. (3.9) $[\chi(\mathbf{k}, q, \omega)/m]$ are identical to those of Eq. (3.12), the expression $\chi(\mathbf{k}, q, \omega)$ can be evaluated such that the square root is kept as a real value by imposing Eq. (3.11). This way, the integral limits can be simply set to the phonon frequencies where the phonon mode of interest is defined. For

example, the upper and lower limits are set to $\omega_1 = \omega_{1L}$ and $\omega_2 = \omega_{2Lz}$, respectively, for the case of LO interface phonons.

Depending on the phonon mode of interest, the function $D(q, \omega)$ may be expressed as

$$D^{\text{IF}} = \frac{Y^4 \left[\frac{\cos^2\left(k_1 \frac{d}{2}\right) \cosh(\alpha q d)}{k_2 + \beta q} + \frac{\left\{ 2 \cos^2\left(k_1 \frac{d}{2}\right) \alpha^2 q^2 + k_1^2 \right\} \sinh(\alpha q d) + \alpha q k_1 \cosh(\alpha q d) \sin(k_1 d)}{2 \alpha q (\alpha^2 q^2 + k_1^2)} \right]^2}{\cosh^2(\alpha q d) \zeta(\beta)^+ + \alpha q d \zeta(\alpha)^- + \sinh(\alpha q d) \zeta(\alpha)^+} \quad (3.13)$$

or

$$D^{\text{C}} = \frac{Y^4 \left[\frac{\cos^2\left(k_1 \frac{d}{2}\right) \cos(\alpha q d)}{k_2 + \beta q} + \frac{\left\{ 2 \cos^2\left(k_1 \frac{d}{2}\right) \alpha^2 q^2 - k_1^2 \right\} \sin(\alpha q d) - \alpha q k_1 \cos(\alpha q d) \sin(k_1 d)}{2 \alpha q (\alpha^2 q^2 - k_1^2)} \right]^2}{\cos^2(\alpha q d) \zeta(\beta)^+ + \alpha q d \zeta(\alpha)^+ + \sin(\alpha q d) \cos(\alpha q d) \zeta(\alpha)^-} \quad (3.14)$$

with

$$Y = \left[\frac{\sin(k_1 d)}{2k_1} + \frac{d}{2} + \frac{\cos^2(k_1 d / 2)}{k_2} \right]^{-\frac{1}{2}} \quad (3.15)$$

where $\zeta^\pm(\alpha) = (1/2\alpha)(\partial \varepsilon_{1t}/\partial \omega) \pm 2\alpha(\partial \varepsilon_{1z}/\partial \omega)$, $\zeta^\pm(\beta) = (1/2\beta)(\partial \varepsilon_{2t}/\partial \omega) \pm 2\beta(\partial \varepsilon_{2z}/\partial \omega)$,

$\beta = \frac{1}{2} \sqrt{|\varepsilon_{2t}(\omega)/\varepsilon_{2z}(\omega)|}$, and k_1 and k_2 are the magnitudes of the electron wave vector inside and

outside of the typical finite quantum well. Only the electronic ground state of the quantum well is considered and a conduction band offset of 2.3 eV between AlN and GaN is assumed [54].

3.4 Group Velocity of Emitted Optical Phonons

In Eq. (3.9), the phase ($v_p = \omega/q$) and group velocity ($v_g = d\omega/dq$) of the phonon modes (or its reciprocal) are frequently used. Given the complex form of the phonon wave vector q , instead of expressing these velocities in a closed form equation, the velocities are calculated numerically. The group velocity is not only a component of the integral but also a crucial factor that describes the behavior of the phonons and, furthermore, the thermal characteristics of the system. Figure 3.3 shows the group velocity of the interface and confined phonon modes as a function of phonon frequency. As expected by the dispersion relation shown in Figure 3.2, the interface mode phonons possess a considerably larger group velocity than the confined mode phonons. The largest confined mode group velocity is less than 7 km/s at $\omega \sim 552 \text{ cm}^{-1}$ (TO mode), whereas the largest interface mode group velocity reaches up to 138 km/s (or 138 nm/ps) at $\omega = \omega_{1Lt}$ (LO mode). It is easily deduced that if the full spectrum of interface phonon modes can be utilized, the phonons can carry

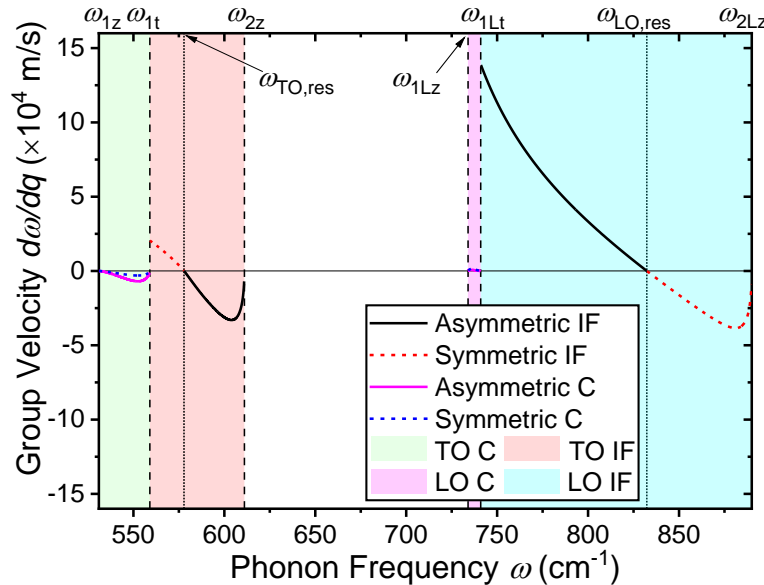


Figure 3.3. Numerically calculated group velocities of interface and confined mode phonons as a function of phonon frequency. For both interface and confined modes, the solid and dashed lines indicate the asymmetric and symmetric phonon modes, respectively. The group velocity of interface phonons goes to zero close to the TO and LO resonant frequency ($\omega_{TO,res}$ and $\omega_{LO,res}$ shown in vertical dotted lines). Maximum group velocity of 138 km/s occurs at $\omega = \omega_{1Lt}$ for the interface mode phonons. This value is almost 20 times that of the maximum group velocity of the confined mode phonons.

a portion of the generated heat away along the heterointerface. This would be an additional heat transport mechanism, on top of the always existing acoustic phonon heat transport, that can help the system dissipate heat more efficiently.

To better understand the electron interaction with these interface and confined mode phonons, Eq. (3.9) is evaluated and the scattering rates between the electrons and optical phonons are calculated. Figure 3.4 shows the (a) interface and (b) confined mode phonon scattering rates as a function of electron energy E_k . For both (a) interface and (b) confined modes, the black solid line shows the total scattering rate which combines all contributions from each process indicated as dashed and dotted color lines. The general behaviors of the scattering rate curves for both modes are similar. The LO emission scattering rates [(a) red and (b) orange dashed lines] start to dominate once the

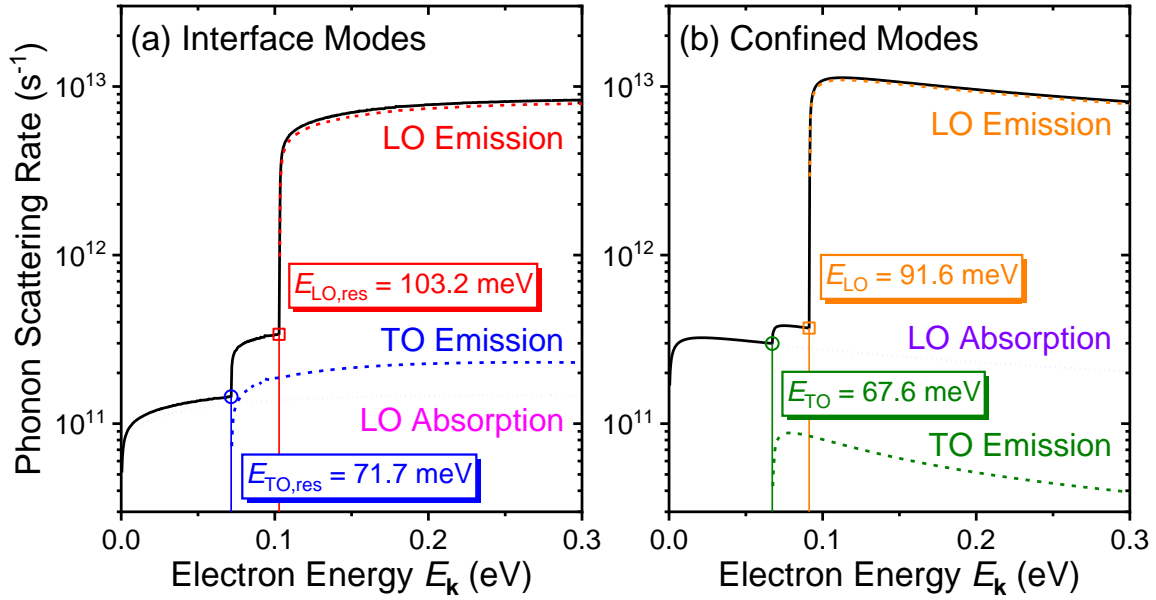


Figure 3.4. (a) Interface and (b) confined mode phonon scattering rates are calculated and plotted as a function of electron energy. For both modes, the total interface phonon scattering rate combining all phonon modes (including the TO absorption scattering rate) is shown as the black solid line. The droplines with symbols are shown to indicate the threshold energies of TO emission and LO emission scattering. For interface mode scattering, these energies correspond to the TO and LO interface phonon resonant frequency energies $\hbar\omega_{TO,res} = 71.7$ meV and $\hbar\omega_{LO,res} = 103.2$ meV, respectively. For confined mode scattering, the threshold energies are in the vicinity of (but not identical to) the TO and LO phonon energies of GaN, $\hbar\omega_{1z} = 65.8$ meV and $= 91.9$ meV, respectively.

$\hbar\omega_{1L}$ electron energy exceeds the threshold energy. The TO absorption processes are negligible compared to the others (not plotted in the figures). Due to mode mixing in wurtzites, the TO emission scattering rate is comparable to the LO absorption scattering rate. This causes the total scattering rate to take a two-step-like shape. The total scattering rates of both modes are roughly similar, converging to $\sim 10^{13} \text{ s}^{-1}$ with $E_k = 0.3 \text{ eV}$ in the current system where the GaN thickness is set to $d = 5 \text{ nm}$. As shown in Figure 3.3, since it is known that the interface mode phonons typically show larger group velocity, a comparable scattering rate between the interface and confined mode phonons indicates that the average phonon velocity of the phonons emitted due to these processes may be large enough to help dissipate the heat.

Focusing on the interface mode LO emission scattering rate [red dashed curve in (a)], the emission threshold energy is observed at 103.2 meV. This energy corresponds to the energy of the LO resonant phonon frequency ($\omega_{LO, \text{res}} = 832.3 \text{ cm}^{-1}$) shown as the horizontal dotted line in Figure 3.2 (b). The LO phonon emission process through electron–phonon scattering can only occur when the electron has, at least, more energy than the phonon to be emitted; of course, more specifically, the condition described by Eq. (3.12) must be satisfied. The emission threshold energy of 103.2 meV indicates that phonons with at least this amount of energy are most likely to be emitted. From Figure 3.3, it is shown that the group velocity of phonons with the resonant frequencies $\omega_{LO, \text{res}}$ and $\omega_{TO, \text{res}}$ are zero. The TO emission threshold energy (71.7 meV) also corresponds to the energy of TO resonant phonon frequency ($\omega_{TO, \text{res}} = 577.8 \text{ cm}^{-1}$). These observations of Figure 3.4 suggest that, however large the group velocity of interface phonons *could* be, simply increasing the interface phonon mode scattering rate with respect to the confined phonon mode scattering rate may not improve the heat dissipation efficiency of the system.

For the confined modes in Figure 3.4 (b), the TO and LO emission threshold energies are shown as 67.6 and 91.6 meV, respectively. The TO emission threshold is slightly larger than $\hbar\omega_{\text{Lz}} = 65.8$ meV. As shown in the dispersion curve in Figure 3.2 (a), the confined mode phonon frequencies asymptotically approach ω_{Lz} with increasing phonon wave vector q . As the electron energy $E_{\mathbf{k}}$ increases, the energy and momentum conservation condition Eq. (3.12) [or Eq. (3.10) > 0] is first satisfied at a considerably large q . It is revealed from the scattering rate calculation that this q is obtained when the phonon frequency ω is close to $\omega_{\text{Lz}} = 531 \text{ cm}^{-1}$, but slightly larger. Similarly, the LO emission threshold is slightly smaller than $\hbar\omega_{\text{Ll}} = 91.9$ meV and this is due to the dispersion, shown in Figure 3.2 (b), approaching ω_{Ll} with increasing q . Since Figure 3.2 is shown with the dimensionless x -axis wave vector qd , it is apparent that the emission threshold energies will also be affected by the GaN thickness d .

Figure 3.5 shows the interface and confined mode phonon emission scattering rates of an AlN/GaN/AlN double heterostructure with GaN thickness of $d = 1$ nm. Compared to the previous $d = 5$ nm case shown in Figure 3.4, indeed, the interface mode scattering rate (red solid line) becomes approximately 8 times larger than the confined mode scattering rate (blue dashed line) for electron energy larger than 0.12 eV. Also notice that the interface mode scattering curve shows more than two of the step-like features. This is due to the emission threshold energy split between the symmetric and asymmetric interface modes. With $d = 5$, the wave vector q is only large enough to satisfy the emission condition at phonon frequencies of $\omega = \omega_{\text{TO(LO),res}}$. However, with smaller d , this is no longer the case and the condition is satisfied with phonon frequencies slightly away from the resonant frequencies. As the symmetric and asymmetric interface modes are defined in

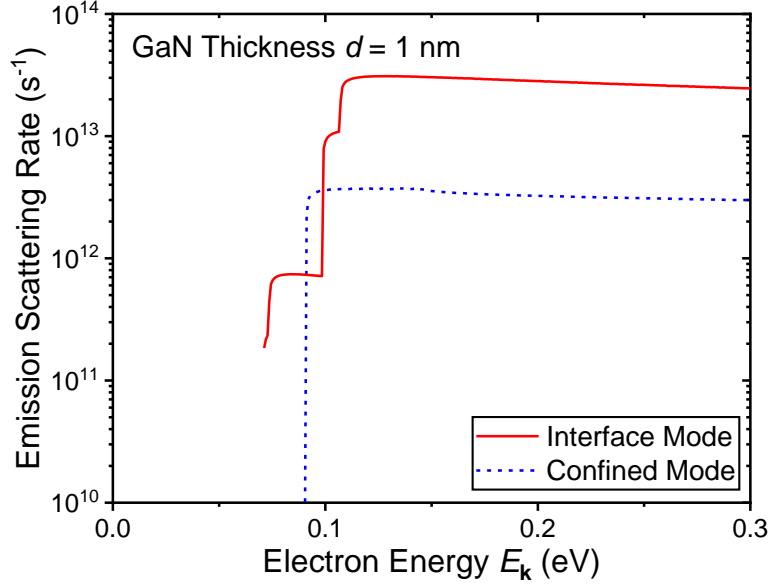


Figure 3.5. Interface and confined mode phonon emission scattering rates of the AlN/GaN/AlN double heterostructure with GaN thickness of $d = 1$ nm. Compared to the $d = 5$ nm case, the interface mode scattering rate (red solid line) shows a factor of 3 increase, whereas the confined mode scattering rate (blue dashed line) shows a factor of 2.5 decrease. Overall, the interface phonon scattering rate is approximately 8 times the confined mode scattering rate with GaN thickness of $d = 1$ nm.

separate phonon frequencies, except at the limit of $\omega \rightarrow \omega_{\text{TO(LO),res}}$, the threshold energies are split and cause the scattering rate curve to show more step-like increases.

To further examine the interface phonons that are emitted in the LO emission scattering process, the integrand of Eq. (3.9) as a function of phonon frequency for different electron energies $E_k = 0.12, 0.3$, and 0.5 eV is presented in Figure 3.6. The plotted curves represent the number of phonons produced with each phonon frequency. The x -axis in this figure is shown in the units of cm^{-1} , but should be interpreted as s^{-1} such that the integral of the curves over the phonon frequency results in the scattering rates represented in s^{-1} .

The vertical dotted line in Figure 3.6 indicates the LO resonant frequency $\omega_{\text{LO,res}} = 832.3 \text{ cm}^{-1}$. Phonons with frequency larger (smaller) than this resonant frequency are symmetric (asymmetric) modes. First, at $E_k = 0.12$ eV, which is slightly above the LO phonon emission threshold energy

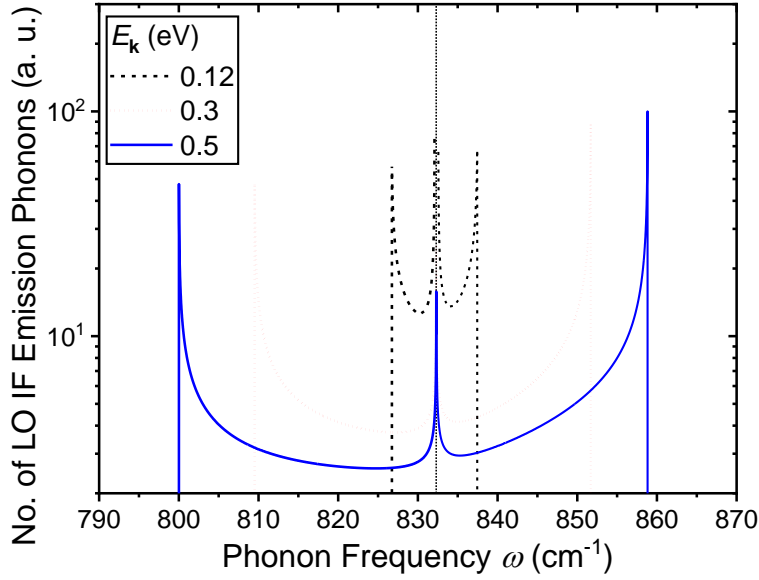


Figure 3.6. Number of produced interface phonons as a function of phonon frequency for different electron energies $E_k = 0.12$ (black dashed line), 0.3 (red dotted line), and 0.5 eV (blue solid line). Only the interface phonons involved in the LO emission phonon process are plotted. The LO phonon resonant frequency is indicated as the vertical dotted line. The y-axis represents the integrand of Eq. (3.9) or equivalently the number of phonons emitted with each phonon frequency.

$E_{\text{LO,res}} = 103.2$ meV, the phonons that are emitted show a small span of frequencies with the ones very close to $\omega_{\text{LO,res}} = 832.3 \text{ cm}^{-1}$ being the majority. As the electron energy increases, the scattering process starts to produce more phonons with frequencies farther away from the resonant frequency. With $E_k = 0.5$ eV, a large number of phonons with $\omega_{\text{LO,res}} \sim 832.3 \text{ cm}^{-1}$ are still generated but the majority of the phonons possess frequencies that are approximately 30 cm^{-1} away from the resonant frequency. Returning to Figure 3.3, it is shown that the group velocity of these LO interface phonon modes is around 30 km/s which is considerably large compared to the maximum group velocity of confined phonons (7 km/s) but still quite small compared to the maximum group velocity of the available interface phonons (138 km/s). In order to utilize the interface phonons with larger group velocity, the electron energy must be increased. However, with GaN thickness set to $d = 5 \text{ nm}$, to utilize the entire span of available interface phonons and generate phonons with the maximum group velocity, calculation results show that the electron

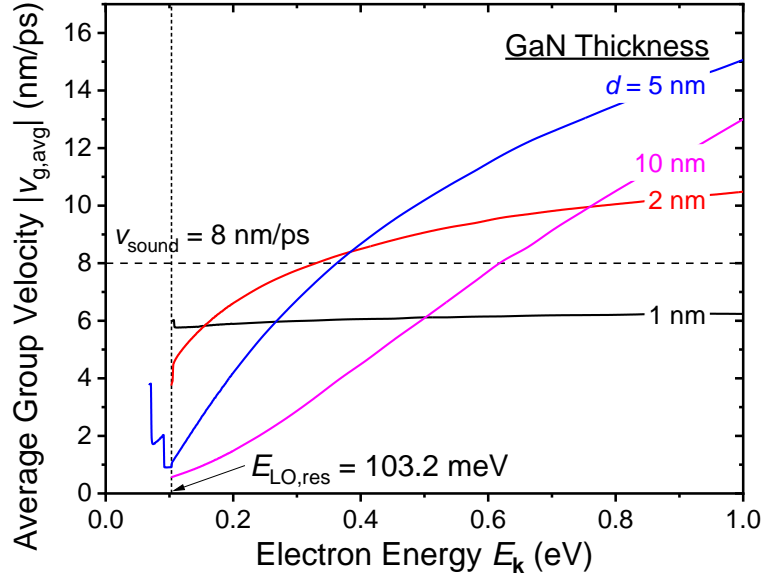


Figure 3.7. Average group velocity of the emitted interface and confined mode phonons with different GaN thickness $d = 1, 2, 5$, and 10 nm as a function of electron energy E_k . As a reference, the longitudinal acoustic phonon propagation velocity along the c -axis [0001] is indicated as the horizontal dashed line. At low energies right above $E_{LO,res} = 103.2$ meV, heterostructures with smaller GaN thickness d show a larger average group velocity. In contrast, as electron energy increases, the average group velocity of heterostructures with thicker d saturates at a larger value.

energy has to increase up to physically unrealistic values as high as $E_k = 100$ eV. An alternative way to produce interface mode phonons with high group velocity may be to increase the GaN thickness d as was suggested from the dispersion relation shown in Figure 3.2. The group velocity (in Figure 3.3) scales linearly with d ; for example, if the thickness increases two-fold to $d = 10$ nm, the group velocity at each phonon frequency also increases to twice the value calculated at $d = 5$ nm.

The GaN thickness d , phonon dispersion relation, interface phonon mode group velocity, and electron energy E_k must all be taken into account to understand if the nonzero interface mode phonons can be exploited to effectively dissipate heat of the system. To this end, we calculate and present in Figure 3.7 the average group velocity of the emitted interface and confined mode phonons with different GaN thicknesses $d = 1, 2, 5$ and 10 nm as a function of electron energy E_k .

Although a GaN thickness of 10 nm may be difficult to grow with the existing technology due to the strain associated with the lattice mismatch in AlN/GaN/AlN structures, we include it in the analysis to show the trend [55]. The procedure of obtaining the average group velocity is as follows: First, to the integrand of Eq. (3.9) (shown in Figure 3.6), we multiply the phonon frequency dependent group velocity and evaluate the integral to obtain the sum of group velocities of all emitted phonons. After adding up all contributions from each interface and confined, TO and LO, symmetric and asymmetric phonon modes, we divide by the total scattering rate to obtain the average group velocity. The average group velocity $v_{g,avg}$ may be expressed as:

$$v_{g,avg} = -\frac{2me_0^2\tau^e}{\hbar^2} \sum_n \int_{\omega_1}^{\omega_2} \frac{[N(\omega)+1]D(q,\omega)\sigma \left[\left\{ \frac{\omega}{q^2} - \frac{\hbar}{2m} \right\} \frac{dq}{d\omega} - \frac{1}{q} \right]}{\left[\frac{q}{2} - \frac{m}{\hbar} \left\{ \frac{\omega}{q} - \frac{d\omega}{dq} \right\} \right] \sqrt{\frac{1}{m} \chi(\mathbf{k},q,\omega)}} v_g d\omega \quad (3.16)$$

where τ^e is the emission scattering rate obtained from Eq. (3.9), and v_g is the group velocity of the corresponding phonon mode. As a reference, the longitudinal acoustic (LA) mode phonon's sound velocity in GaN along the optical c -axis [0001] is shown as the horizontal dashed line [56]. Among all GaN thicknesses considered, a general trend of increasing average group velocity of emitted phonons as the electron energy increases is shown. This is due to the increase in number of interface phonons with higher group velocities (i.e., phonons with frequency away from resonant frequencies) that are involved in the electron-phonon scattering process. Although only the case for $d = 5$ nm is shown in Figure 3.6, a similar trend was observed for all GaN thicknesses: with higher electron energy, more phonons with higher group velocity are emitted.

For the $d = 5$ nm case, at energies smaller than 103.2 meV, a step-like change in average group velocity is shown. This is due to the contribution of different phonon modes with different group

velocities. As the electron energy increases, at each emission threshold energy $E_{\text{TO}} = 67.6$ meV, $E_{\text{TO, res}} = 71.7$ meV, $E_{\text{LO}} = 91.6$ meV, and $E_{\text{LO, res}} = 103.2$ meV (see Figure 3.4), different modes of phonons start to emit, and their contributions appear in the curve as step-like shapes. At energies larger than $E_{\text{LO, res}}$, most of the phonons that are emitted are confined and interface LO phonons, and the average group velocity is determined by the competition between these two factors. The step-like changes for the curves of different GaN thicknesses are omitted in the figure. For the $d = 1$ nm case, at low electron energies right above $E_{\text{LO, res}} = 103.2$ meV, the average group velocity is the largest compared to the velocities with different thicknesses but has already almost saturated to its largest value which is around 6 nm/ps. As the thickness increases, the group velocity starts at a smaller value but increases more steadily and saturates at a larger value (the velocity for the $d = 10$ nm case does not even start to saturate at $E_k = 1.0$ eV suggesting that it has potential to reach a higher value). From the curves, therefore, depending on the range of available electron energies and their distribution in energy, an appropriate GaN thickness can be selected such that the interface phonons can contribute to the heat dissipation process. Putting the electron energies and distribution aside, we see that the average group velocity can easily be engineered to a value comparable to the acoustic phonon's sound velocity. Considering that the acoustic phonons are the major contributor of thermal conduction in semiconductor materials, the results suggest that the generated optical phonons of these systems may also contribute largely to the thermal conduction.

3.5 Conclusion

In conclusion, the interface and confined mode optical phonons of a wurtzite AlN/GaN/AlN double heterostructure and their interaction with electrons are theoretically studied based on the uniaxial dielectric continuum model. The phonon dispersion relation of these phonon modes and

the electron–phonon scattering rates are calculated numerically to derive the average group velocity of the emitted phonons to explore the possibility of exploiting the interface mode phonons as an additional heat dissipation channel. Our estimations show that the average group velocity of phonons that are emitted through electron–phonon scattering processes with electron energy slightly larger than the threshold energy ($E_{\mathbf{k}} \approx E_{\text{LO, res}}$) is very small (for the $d = 5$ nm case, 0.9 nm/ps) compared to the LA phonon propagation velocity of bulk GaN ($v_{\text{sound}} = 8$ nm/ps). This is due to the dispersion relation of interface mode phonons which shows curves that converge to the resonant phonon frequency at large phonon wave vector q . With larger electron energies, the average optical group velocity can exceed the acoustic phonon velocity starting from $E_{\mathbf{k}} = 0.35$ eV. Given the energy distribution of electrons, the quantum well thickness can be engineered to exploit the interface mode phonons, which can propagate a distance of a few tens of nanometers before decaying into heat-carrying acoustic phonons.

CHAPTER 4 THERMAL RESISTANCE OPTIMIZATION OF GaN/SUBSTRATE STACKS

Parts of this chapter are reproduced from [57], with the permission of AIP Publishing.

4.1 Introduction

Gallium nitride (GaN) materials have excellent material properties such as high critical electric field (3.3 MV/cm), high saturation velocity (2.5×10^7 cm/s), and high thermal/chemical/physical stability, making them ideal for high-power and high-frequency devices [58]. Substrates on which GaN-based devices are grown vary greatly from conventional sapphire and silicon carbide to emerging silicon and diamond. Nonetheless, the lattice mismatch for GaN device epitaxy of these substrates leads to high-defectivity ($> 10^8$ cm⁻²) devices, suffering from not only poor electrical characteristics [58] but also degraded thermal performance associated with high thermal boundary resistance (TBR) [59]. Device thermal resistance, defined as the maximum temperature increase in the device divided by the power dissipation of the device, is dominated by the TBR. Recent works have traced up to 50% of the device thermal resistance back to TBR [60]. As device lifetime has an exponential dependence on the temperature [61], [6] such high-power GaN-devices (e.g. 40 W/mm [62]) are thermally limited [26]. Conventional approaches addressing this thermal limitation include switching to high thermal conductivity substrates (such as SiC [63] and diamond [64], [65]) and TBR-engineering [66]. Alternatives such as utilizing lattice-matched free-standing GaN substrate which provides low dislocation density and reduces TBR are also under investigation to enhance electrical and thermal performance of GaN-based devices. More challenging and expensive but effective approaches include convection cooling by flowing liquid and/or vapor through micro-channels or nanoporous structures [67].

In this chapter, through technology computer-aided design TCAD Synopsys [68], the effects of substrates (diamond, silicon carbide, silicon, and sapphire), thermal boundary resistance (10 to 60 m²K/GW), heat source lengths (10 nm to 20 µm), and power dissipation levels (1 to 8 W) on the thermal resistance of GaN/substrate stacks are investigated. With respect to available literature [69], [70], we include detailed TBR and temperature-dependent thermal conductivity analysis, which points towards an optimal separation between heat source and the substrate for improved thermal management.

4.2 Heat Transfer Basics

The basic heat transfer equation [71] that is used to determine the temperature profile of a structure is written as

$$C_p \rho \frac{\partial T}{\partial t} = \nabla \cdot (\kappa \nabla T) + S \quad (4.1)$$

where T is the temperature, C_p is the specific heat, ρ is the density, κ is the thermal conductivity, and S is the heat source density. For stationary cases, the equation reduces to

$$-\nabla \cdot (\kappa \nabla T) = S. \quad (4.2)$$

The boundaries either have a fixed temperature (Dirichlet boundary condition) or a constant heat flux density (Neumann boundary condition). The boundary condition may be written as

$$[\kappa \nabla T]_n = q \quad (4.3)$$

$$q = \alpha (T - T_{\text{ext}}) \quad (4.4)$$

where the subscript n indicates the heat flux component normal to the boundary, q is the heat flux, α is the heat transfer coefficient, and T_{ext} is the external temperature (e.g., temperature of the

thermal contact). Using these basic equations, temperature profile of a simple 1-D structure can be computed easily if boundary conditions, structure dimensions, and thermal conductivity of each material composing the structure are known.

TBR acts on the temperature profile similarly to the heat transfer coefficient or thermal resistance.

The heat flux at the interface is given as

$$q = \frac{T_1 - T_2}{R_{TB}} \quad (4.5)$$

where T_1 and T_2 are temperatures of each side of the boundary and R_{TB} is the TBR.

For a structure shown in Figure 4.1, assuming the heat contacts are ideal, the side wall boundaries are adiabatic, and the thermal conductivities are independent of temperature, the heat transfer equation can be expressed as

$$q = \kappa_1 \frac{T_{TOP} - T_1}{L_1} = \frac{T_1 - T_2}{R_{TB}} = \kappa_2 \frac{T_2 - T_{BOT}}{L_2} \quad (4.6)$$

where T_{TOP} and T_{BOT} are the temperatures of the heat source and heat sink, respectively, L_1 and L_2 are thicknesses, κ_1 and κ_2 are thermal conductivities of each layer, and T_1 and T_2 are temperatures of each side of the interface. The temperatures T_1 and T_2 can be expressed as a function of other parameters as

$$T_1 = T_{TOP} - qR_1 \quad (4.7)$$

$$T_2 = T_{\text{BOT}} + qR_2 \quad (4.8)$$

where

$$q = \frac{T_{\text{TOP}} - T_{\text{BOT}}}{R_1 + R_{\text{TB}} + R_2} \quad (4.9)$$

$$R_1 = \frac{L_1}{\kappa_1} \quad (4.10)$$

$$R_2 = \frac{L_2}{\kappa_2}. \quad (4.11)$$

Applying these equations, the temperatures T_1 and T_2 of a structure have been calculated and compared to simulation results in Figure 4.1 (b). The parameters were set as $T_{\text{TOP}} = 400$ K, $T_{\text{BOT}} =$

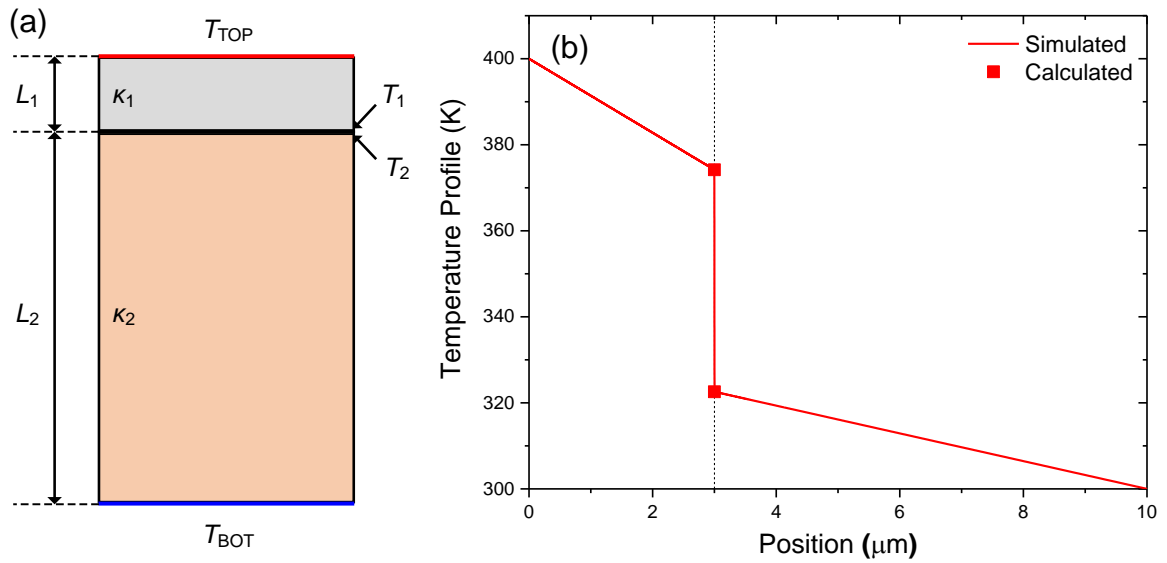


Figure 4.1. Example (a) structure and (b) temperature profile of 1-D heat transfer. (a) Temperature of heat contacts, thicknesses and thermal conductivities of each layer. (b) Temperature distribution has been simulated and calculated by setting $T_{\text{TOP}} = 400$ K, $T_{\text{BOT}} = 300$ K, $L_1 = 3$ μm , $L_2 = 7$ μm , $\kappa_1 = 1.5$ W/cm-K, $\kappa_2 = 4.0$ W/cm-K, and $R_{\text{TB}} = 4 \times 10^{-4}$ cm²K/W.

300 K, $L_1 = 3 \text{ } \mu\text{m}$, $L_2 = 7 \text{ } \mu\text{m}$, $\kappa_1 = 1.5 \text{ W/cm-K}$, $\kappa_2 = 4.0 \text{ W/cm-K}$, $R_{\text{TB}} = 4 \times 10^{-4} \text{ cm}^2\text{K/W}$.

Temperatures T_1 and T_2 obtained by above equations matched the simulation results exactly.

In addition to the temperature profile, the total thermal resistance of a device R_{DEV} can be written as

$$R_{\text{DEV}} = \frac{T_{\text{TOP}} - T_{\text{BOT}}}{qA} = \frac{1}{A} (R_1 + R_{\text{TB}} + R_2) \quad (4.12)$$

where A is the area of the device. As mentioned above, the thermal resistance of a device is determined by dividing the temperature difference between the heat source and the heat sink by the power applied to the device. Because the heat flux only flows in one direction in this case, the thermal resistance is obviously equal to the thermal resistance of each layer combined. In order to reduce the thermal resistance, we can (1) change the material of the layers to a thermally more conductive material (larger κ_1 and κ_2), (2) reduce the thickness of the layers (smaller L_1 and L_2), or (3) reduce the TBR (smaller R_{TB}).

A structure with more layers or thermal resistances between layers and heat contacts can also be expressed easily using the basic equations given above. Nevertheless, when the problem involves more than two dimensions, the problem gets more complicated and becomes hard to solve analytically. The analytic expression for thermal resistance of AlGaN/GaN devices composed of two layers has been presented in Ref. [72]. However, the solution given in this paper does not take TBR into account and is therefore inadequate to describe the actual temperature distribution. Numerical methods must be adapted to obtain more realistic results.

4.3 Simulation Using Finite Difference Analysis MATLAB Code

As mentioned in the previous section, analytic solutions have their limits in obtaining temperature profiles when structures become more complex. Numerical methods can be used to further understand the physics related in heat transfer with various geometries. Before using commercial simulation software, we have implemented a 2-D heat transfer calculation MATLAB code to understand how temperature distributions of 2-D structures can be calculated.

Finite difference analysis is a relatively easy way to implement a simulation code. After assigning grid points to the structure, we solve Eqs. (4.2)–(4.5) for every grid point to obtain the temperature distribution of the whole device. In order to apply the equations on each point, we need to discretize the structure. A general form of the discretized equation may be written as

$$-\frac{\kappa_i^+}{\Delta x^2} T_{i+1,j} - \frac{\kappa_i}{\Delta y^2} T_{i,j+1} + \left[\frac{\kappa_i^+ + \kappa_i^-}{\Delta x^2} + \frac{\kappa_i}{\Delta y^2} \right] T_{i,j} - \frac{\kappa_i}{\Delta y^2} T_{i,j-1} - \frac{\kappa_i^-}{\Delta x^2} T_{i-1,j} = S_{i,j} \quad (4.13)$$

where

$$\kappa_i^+ = \frac{\kappa_i + \kappa_{i+1}}{2} \quad (4.14)$$

$$\kappa_i^- = \frac{\kappa_i + \kappa_{i-1}}{2} \quad (4.15)$$

i and j are the index for grid point in the x - and y -direction, respectively, and Δx^2 and Δy^2 are distance between x and y grid points, respectively. After we write down the equations for every grid point, we collect and align them to set a matrix equation in the form of

$$\begin{bmatrix}
\frac{\kappa_1^+ + \kappa_1^-}{\Delta x^2} + \frac{2\kappa_1}{\Delta y^2} & -\frac{\kappa_1}{\Delta y^2} & \dots & -\frac{\kappa_1^+}{\Delta x^2} \\
-\frac{\kappa_1}{\Delta y^2} & \frac{\kappa_1^+ + \kappa_1^-}{\Delta x^2} + \frac{2\kappa_1}{\Delta y^2} & -\frac{\kappa_1}{\Delta y^2} & \dots & -\frac{\kappa_1^+}{\Delta x^2} \\
\vdots & \vdots & \ddots & \ddots & \vdots \\
\dots & -\frac{\kappa_2^-}{\Delta x^2} & \dots & -\frac{\kappa_2}{\Delta y^2} & \frac{\kappa_2^+ + \kappa_2^-}{\Delta x^2} + \frac{2\kappa_2}{\Delta y^2} & -\frac{\kappa_2}{\Delta y^2} & \dots & -\frac{\kappa_2^+}{\Delta x^2} & \dots \\
& \vdots & \vdots & \ddots & \vdots & \ddots & \vdots & \vdots & \ddots
\end{bmatrix}
\begin{bmatrix}
T_{1,1} \\
T_{1,2} \\
T_{1,3} \\
\vdots \\
T_{1,N_y} \\
T_{2,1} \\
\vdots \\
T_{2,N_y} \\
\vdots \\
T_{N_x,N_y}
\end{bmatrix}
=
\begin{bmatrix}
S_{1,1} \\
S_{1,2} \\
S_{1,3} \\
\vdots \\
S_{1,N_y} \\
S_{2,1} \\
\vdots \\
S_{2,N_y} \\
\vdots \\
S_{N_x,N_y}
\end{bmatrix}$$

where N_x and N_y are the number of points in the x - and y -direction. It should be noted that every grid point on the edge of the structure has one boundary condition, and every grid point on the corner of the structure has two boundary conditions. Every equation for each set of i and j involves temperature of five grid points, hence every row of the matrix has five elements, unless the point is on the edge of the device or has a boundary condition.

After the matrix equation is set, the temperature distribution of the device can be obtained by multiplying the inverse of the square matrix on the left-hand side of the equation to the right-hand side of the equation. Using the code, simulations are carried out for a device that has a geometry similar to Figure 4.1 (a) but with a different heat source size. The structure is presented in Figure 4.2(a) and the simulation results obtained from the commercial TCAD software Synopsys Sentaurus and from the finite difference analysis MATLAB code are plotted together in Figure 4.2 (b). Because now the heat flux not only spreads in the vertical direction but also in the lateral direction, due to the reduced heat source size, the thermal resistance of the device cannot be calculated using the simple equations given in the previous section.

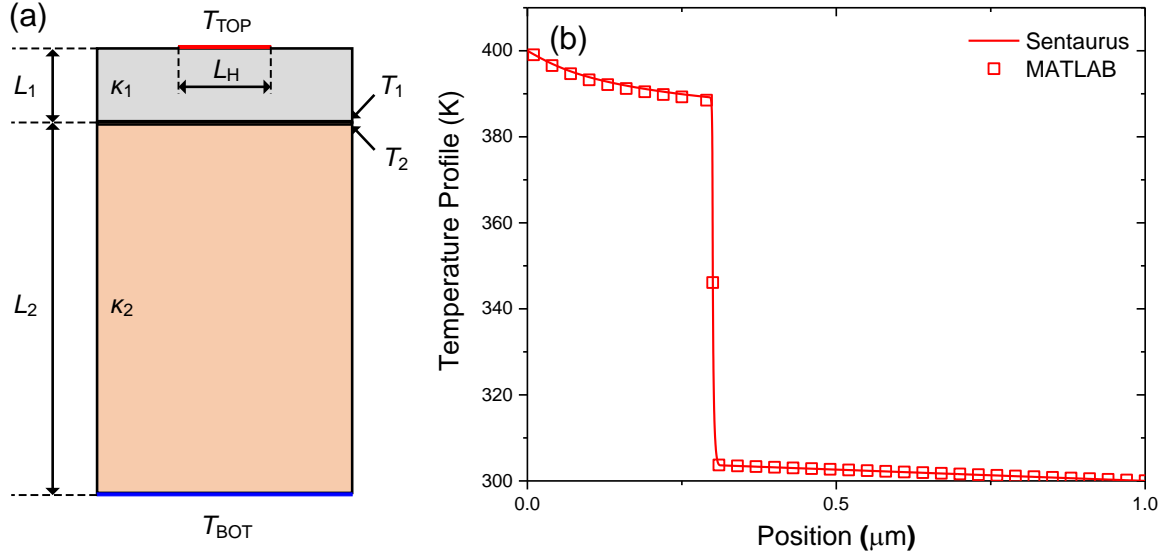


Figure 4.2. Example (a) structure and (b) temperature profile of 2-D heat transfer. (a) Temperature of heat contacts, thicknesses and thermal conductivities of each layer. The heat source size is reduced to L_H . (b) Temperature distribution has been simulated and calculated by setting $T_{TOP} = 400$ K, $T_{BOT} = 300$ K, $L_1 = 0.3$ μm , $L_2 = 0.7$ μm , $L_H = 0.1$ μm , $\kappa_1 = 1.5$ W/cm-K, $\kappa_2 = 4.0$ W/cm-K, and $R_{TB} = 4 \times 10^{-4}$ $\text{cm}^2\text{K/W}$.

4.4 Thermal Properties of GaN and Substrate Materials

From the previous section, we can see that thermal conductivity of the two materials and the TBR of the interface are closely related to the heat transfer and thermal resistance of the whole device. Therefore, the values used in the simulation may have quite an impact on the simulation results. Hence, setting the correct value for thermal conductivity and TBR is essential.

A list of thermal conductivities of GaN and substrate materials from other literature is shown in Table 4.1. Thermal conductivity values at 300 K and their temperature dependencies are shown together. Temperature dependency of thermal conductivity usually obeys a power law relation such as

$$\kappa(T) = \kappa_{300\text{K}} \left(\frac{T}{300} \right)^\gamma \quad (4.16)$$

where κ_{300K} is the thermal conductivity at 300 K and γ is the exponent of the power law. The exponent of the power law is listed in Table 4.1 as well whenever available in the literature. Note that some of the temperature dependencies are given as a polynomial relation rather than a power law relation. Also, it should be noted that although the thermal conductivity values reported show a slight discrepancy, the range is not too broad, varying by less than a factor of two, except for diamond. The reason for this relatively large uncertainty in diamonds is suspected to be the influence of the growth method.

In addition, TBR of the interface of GaN and substrate materials from other literature is shown in Table 4.2. TBR was also found to have a temperature-dependent behavior from experiments [73], [74], [75]. However, rather than showing a material-dependent temperature dependency, TBR tends to differ largely from device to device. Since this is the case, it will be difficult to model the behavior of the device by using one fixed value of TBR.

Based on the literature search of these thermal properties, a set of thermal conductivity values to represent each material and four values of temperature-independent TBR for each GaN/substrate interface is selected in the simulations to illustrate the general trend of thermal resistance with varying TBR. The selected thermal parameters are listed in Table 4.3 in the next section.

Also, we point out that theoretically predicted values of thermal conductivity and TBR were excluded from the list. Theory-based thermal conductivities were found to be much higher than experimentally measured values and, similarly, theoretical calculations of TBR are at least an order of magnitude smaller than experimental values [76], [77], [78], [79].

Table 4.1. Thermal conductivity values of GaN and substrate materials from other literature. Thermal conductivities at 300 K and their temperature dependencies are shown together.

Material	Thermal Conductivity κ (W/m-K)		References
	@300K	Temp. Dep.	
GaN	230	$T^{-1.22}$	[80]
	186-205	-	[81], [82]
	160	$T^{-1.4}$	[83]
	156 ^a	$\alpha = -0.005, \beta = 3.8 \times 10^{-5}$	[84]
	155	-	[85]
	150	$T^{-1.4}$	[72], [73], [86]
	130	$T^{-1.4}$	[70]
Si	150	$T^{-1.3}$	[73], [87]
	148	$T^{-1.65}$	[88]
	148	$T^{-1.3}$	[89], [86]
SiC	490	-	[90]
	475 ^a	$\alpha = -0.003, \beta = 1.7 \times 10^{-5}$	[84]
	420	$T^{-1.3}$	[87]
	400	-	[65], [83]
	400	T^{-1}	[83], [89]
	373	$T^{-1.49}$	[86]
	370	$T^{-1.49}$	[88], [91]
	330	-	[72]
Sapphire	38 ^a	$\alpha = -0.022, \beta = 16 \times 10^{-5}$	[84]
	36	-	[85]
	35	T^{-1}	[73]
	~35	-	[65]
Diamond	800-1800	-	[65]
	1477 ^b , 1173 ^c	-	[86]
	1200	T^{-1}	[92]
	1200	-	[64]
	1000	-	[89], [93]
	710	-	[64]

^a Temperature dependency is given as $\kappa = (\alpha + \beta T)^{-1}$

^b In-plane value $\kappa = 0.003 \times T^2 - 4.238 \times T + 2478$

^c Out of plane value $\kappa = 0.0024 \times T^2 - 3.397 \times T + 1983$

Table 4.2. TBR of GaN/substrate interfaces.

Substrate	TBR, R_{TB} (m ² K/GW)	References
Si	5 – 10	[94]
	33	[73], [86]
	25	[64]
SiC	33	[73], [86]
	45	[60]
	55	[60], [89]
	5 – 60	[74], [75]
Sapphire	12	[73]
	12	[66]
	25	[66]
Diamond	27	[64], [92]
	36	[65], [86]
	50	[66]

4.5 Device Structure and Simulation Method

Throughout the electrical engineering community, much effort has been devoted to using TCAD simulation tools such as ANSYS, COMSOL, and Synopsys Sentaurus to analyze thermal and electrical properties of GaN HEMT devices. Ahmad *et al.* have simulated electrical and thermal transport using ANSYS to verify their micro-Raman experiments on self-heating, and to locate the hotspot in an AlGaIn/GaN HFET [37]. Wu *et al.* compared their 3-D thermal simulation results to experimental results to show the advantage of GaN HEMTs on diamond substrates over silicon substrates and determined the thermal conductivity of their adhesion layer [95]. Won *et al.* investigated heat conduction through multiple layers of interface material of high power GaN devices to calculate thermal resistance of various configurations using COMSOL [67].

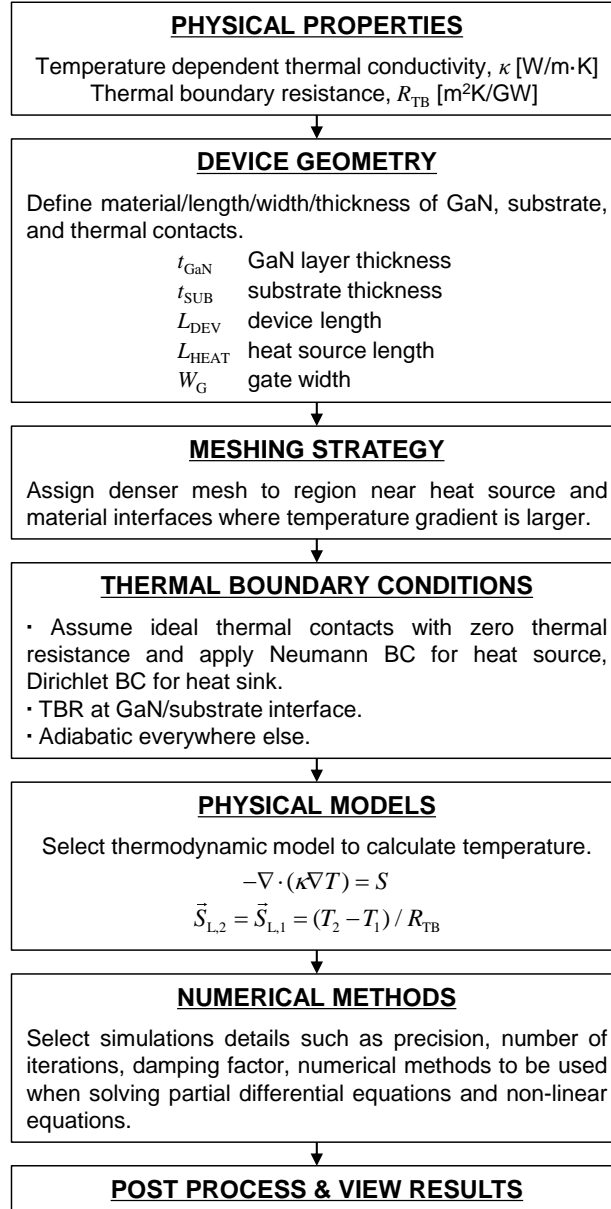


Figure 4.3. Overall process flowchart using TCAD Sentaurus software.

TCAD Synopsys Sentaurus is used to investigate the thermal properties of GaN HEMTs. The simulation process using TCAD Sentaurus is described by the flowchart in Figure 4.3. The only material property associated with this thermal simulation is the thermal conductivity, which can be modified through the parameter files of each material. TBR is assigned to the GaN/substrate interface by the user and is not a material parameter. Device geometry is edited by the Sentaurus

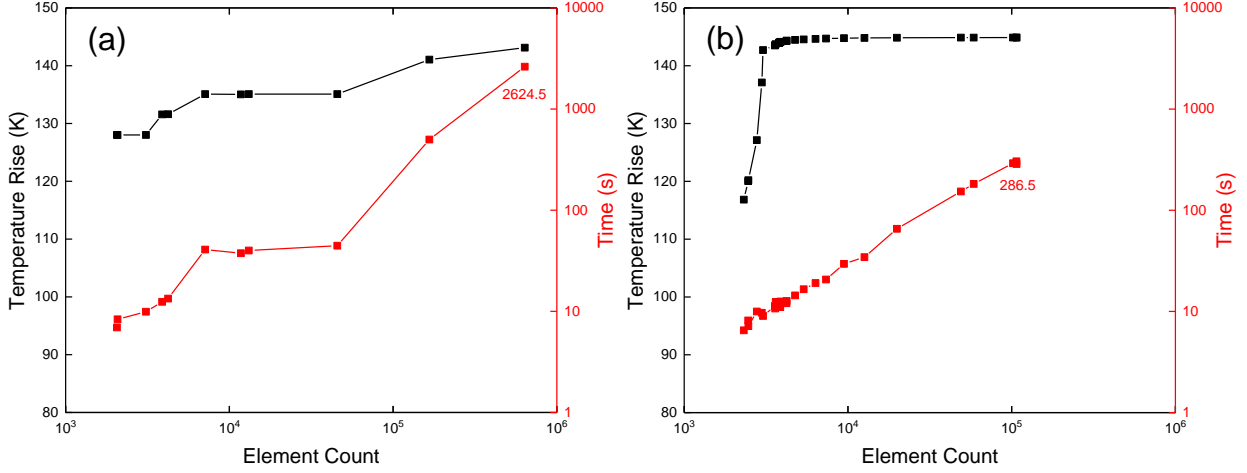


Figure 4.4. Temperature rise and simulation time as a function of element count for the same device with different meshing strategies. (a) Uniformly distributed mesh and (b) dense mesh only near the material interface and heat source.

Structure Editor, which is a package included in the software. After generating the structure, a mesh is assigned to it, which can also be done using the same package, to efficiently and accurately compute temperature distribution. The mesh in this simulation was assigned so that there are more elements near the heat source and the interface, where the temperature gradient is expected to be large. In Figure 4.4, the meshing strategy described above is compared to a uniform meshing strategy in terms of maximum temperature rise in the device and computation time. The saturating maximum temperature rise indicates that the mesh is dense enough to get accurate temperature profiles. Figure 4.4 illustrates that the latter meshing strategy is much more efficient. For boundary conditions, ideal boundary is assumed except for the GaN/substrate interface. Therefore, thermal contacts (i.e., heat source and heat sink) have zero thermal resistance, and every other boundary is adiabatic. Specifically, a constant temperature of 300 K, and a constant heat flux density are allocated for the heat sink and heat source, respectively. To compute the temperature distribution in the device, a set of thermodynamic equations is used. The physical models [71] used in the simulation are identical to those in Eqs. (2.1)–(2.5). Methods and conditions related to numerical computations and solving the necessary partial differential equations and non-linear equations can

also be modified to achieve faster convergence and to obtain more accurate results. The steps from determining thermal boundary conditions to selecting numerical methods are processed using another package called Sentaurus Device. The Sentaurus Device outputs results which can be finally plotted and analyzed using packages such as Sentaurus Visual or Inspect.

The schematic of the simulated device structure is shown in the inset of Figure 4.5. The device structure is designed to replicate a GaN HEMT device. However, thermally less significant components such as the source and drain contacts, and the AlGaN layers are excluded for simplicity [96]. The simulated device has a two-layer structure composed of a varying thickness GaN layer on top of a 300- μm -thick substrate. Device length and width are fixed to 20 μm and 1 mm, respectively. The substrate is heatsinked ideally, which is kept at 300 K. To make a fair comparison between various substrates, a constant heat flux is supplied through the heat sources (instead of keeping the heat source to a fixed temperature). Throughout this work, unless otherwise specified, 1 W of power is dissipated through GaN on Si, SiC, and diamond substrates. For the GaN-on-sapphire device, however, 0.3 W of power is dissipated to prevent unrealistic temperature rise (above 800 K) in the device. Every other face of the device is taken as adiabatic.

Table 4.3. Temperature-dependent thermal conductivity for GaN and other substrate materials, and TBR values for GaN/substrate interfaces used in simulations. For each substrate material, four TBR values are simulated. Temperature-independent thermal conductivity is taken to be equal to the temperature-dependent thermal conductivity at 300 K.

Material	Thermal Conductivity, κ (W/m-K)	TBR ($\text{m}^2 \cdot \text{K}/\text{GW}$)	References
GaN	160 (300/T) ^{1,4}	-	[83]
Sapphire	35 (300/T) ¹	10, 20, 30, 40	[74]
Si	150 (300/T) ^{1,3}	10, 20, 30, 40	[74]
SiC	420 (300/T) ^{1,3}	30, 40, 50, 60	[74]
Diamond	1200 (300/T) ¹	20, 30, 40, 50	[92]

TBR between GaN and substrates, and temperature-dependent thermal conductivities of GaN and substrates, are included in the simulations (Table 4.3). Recent experimental works report differing TBR values from sample to sample [74] and as a function of temperature [73]. However, no TBR model yet exists matching the experimental data. Hence, in an effort to represent a wide TBR range, various TBR values (10 to 60 m²K/GW) are employed in this work (Table 4.3).

4.6 Results and Discussion

Figure 4.5 shows the thermal resistance across GaN/Si as a function of GaN layer thickness (t_{GaN}) (from 0.05 to 4 μm) for various heat source lengths (L_{HEAT}) (0.01, 0.1, 1, 5, 10, and 20 μm), and TBR (20 and 40 m²K/GW). Only the Si substrate is plotted in Figure 4.5; however, all substrate choices lead to the same representative behavior. Figure 4.5 suggests that regardless of the heat source length and GaN layer thickness, thermal resistance increases with increasing TBR. This shows that device thermal resistance can be minimized by reducing the TBR. In addition, by observing the thermal resistance–GaN layer thickness curve for the $L_{\text{HEAT}} = 20 \mu\text{m}$ case, it is shown that when heat source length is comparable to the device length, reducing the GaN layer thickness is helpful in minimizing the thermal resistance. However, as the heat source length decreases (e.g. 0.01 μm), thermal resistance no longer decreases monotonously with GaN layer thickness, but rather it has a minimum. Another way to express this observation is that if the heat source length is relatively small, shrinking the GaN layer thickness beyond a certain point could lead to a significant increase in device thermal resistance.

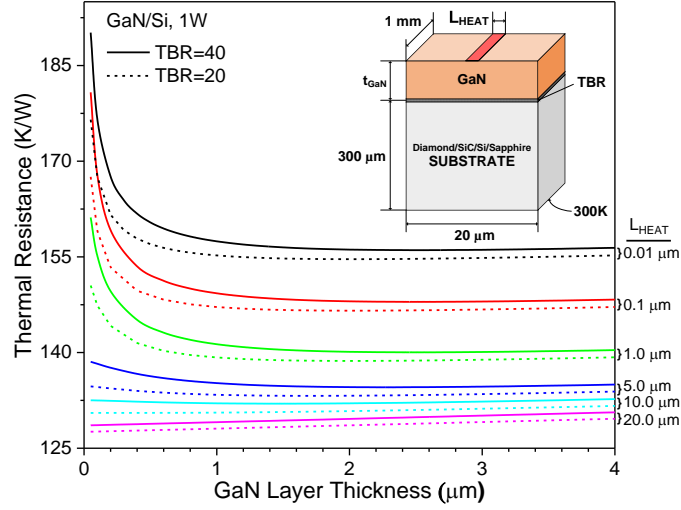


Figure 4.5. Thermal resistance as a function of GaN layer thickness for different heat source lengths (0.01, 0.1, 1, 5, 10, and 20 μm) and TBR values (20 and 40 $\text{m}^2\text{K}/\text{GW}$). Inset shows simulated GaN/substrate stack schematically where device width, length and substrate thickness are taken as 1 mm, 20 μm , and 300 μm , respectively. Heat sink temperature is kept at 300 K. Heat source length (L_{HEAT}), GaN layer thickness (t_{GaN}), and TBR are varied.

The existence of a thermal resistance minimum depends strongly on the heat source length and the TBR. For instance, when $L_{\text{HEAT}} = 10 \mu\text{m}$, thermal resistance–GaN layer thickness curve does not have a minimum when $\text{TBR} = 20 \text{ m}^2\text{K}/\text{GW}$ whereas it does when $\text{TBR} = 40 \text{ m}^2\text{K}/\text{GW}$. As the heat source length gets smaller ($L_{\text{HEAT}} \leq 10 \mu\text{m}$), minima exist even with small TBRs. When the hotspot is localized, the GaN layer acts as a buffer layer for the heat flux to spread out before going through the highly resistive GaN/substrate interface. If the GaN layer is too thin, the concentrated heat flux coming out from the heat source passes through the interface directly without spreading. This causes the region right under the heat source to heat up significantly, which leads to a high thermal resistance. On the other hand, if the GaN layer is too thick, the thermal resistance originating from the thermal conductivity of the GaN layer increases, and also causes the thermal resistance to increase.

Figure 4.6 shows thermal resistance of GaN/substrate devices as a function of GaN layer thickness. Here, the effects of GaN layer thickness on thermal resistance with varying TBR on different substrates is investigated. The heat source length is fixed to $0.01\text{ }\mu\text{m}$ in the rest of the simulations to represent the hotspot of an operating GaN HEMT [37]. Similarly, for every GaN/substrate combination, thermal resistance increases with increasing TBR. Due to the sheer thickness of the substrate, the overall thermal resistance of the device is observed to be dominated by the substrate's thermal conductivity. The symbols on each curve indicate the minimum thermal resistance points. These points show that with increasing TBR, the optimal separation between the heat source and the substrate increases.

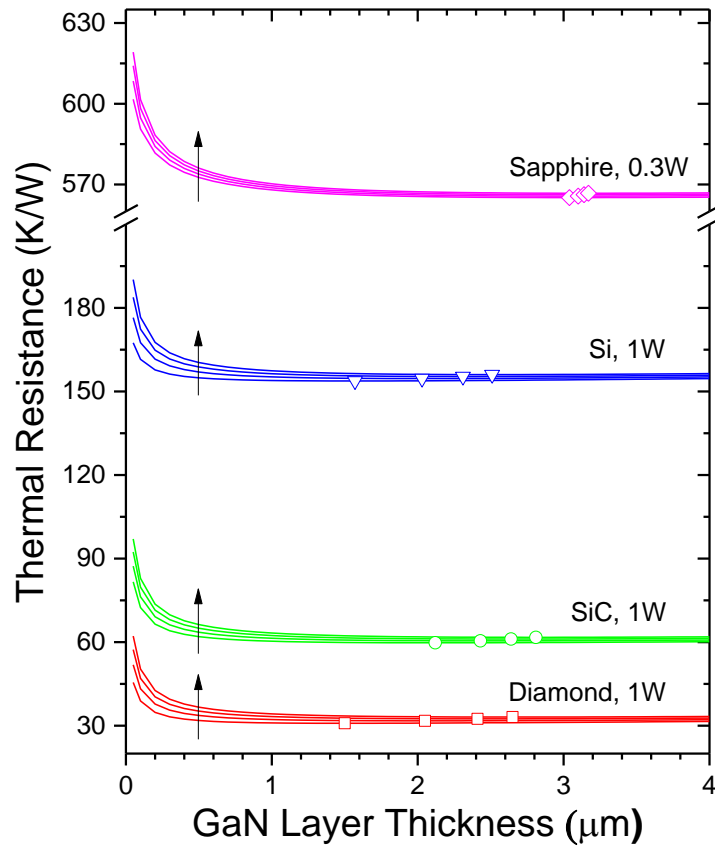


Figure 4.6. The effect of GaN layer thickness on thermal resistance for different substrate materials. Four TBRs (listed in Table 4.3) for each substrate are used. GaN on diamond, SiC, and Si substrates are applied 1 W of dissipated power, whereas those on sapphire substrates are applied 0.3 W of dissipated power. The arrow directions indicate increasing TBR and the symbols indicate the thermal resistance minima.

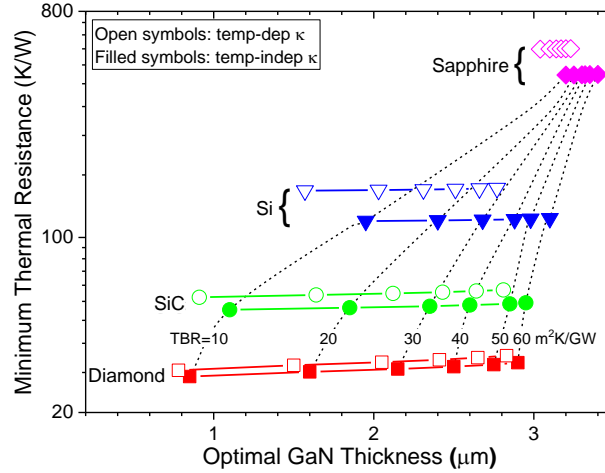


Figure 4.7. Minimum thermal resistance for temperature-independent (filled symbols) and temperature-dependent (open symbols) thermal conductivity cases. 0.3 W of dissipated power was applied to the GaN/sapphire stack, and 1 W of dissipated power was applied to the rest to limit hotspot GaN temperature below 800 K.

Figure 4.7 plots the minimum thermal resistance as a function of optimal GaN layer thickness for different substrates and different TBR values. For comparison, the thermal resistance calculation results are plotted using both temperature-independent (closed symbols) and temperature-dependent (open symbols) thermal conductivities of GaN and substrate materials. The temperature-independent thermal conductivity values are chosen as the temperature-dependent thermal conductivity values at 300 K.

Figure 4.7 shows that when temperature-dependent thermal conductivity is used, compared to when temperature-independent thermal conductivity is used, the minimum thermal resistance of all devices increases. Concurrently, for a given TBR of each substrate the optimal thickness for minimum thermal resistance reduces and the reduction in the optimal thickness increases as we switch to less thermally conductive substrates. This is primarily attributed to the reduction in thermal conductivity of the GaN layer under elevated temperatures. Since the heat source is located at the top of the device, thermal conductivity reduction is most substantial in the GaN layer right beneath the heat source. And because of this reduction, the effective heat source length is larger

than the actual heat source length. As shown in the analysis of Figure 4.5, this heat source length extension causes the optimal GaN layer thickness to decrease.

For instance, Figure 4.7 results show that, in the case of the optimized GaN-on-diamond stacks with $TBR = 10 \text{ m}^2\text{K/GW}$, the thermal conductivity near the hotspot drops from $160 \text{ W/m}\cdot\text{K}$ down to $\sim 140.5 \text{ W/m}\cdot\text{K}$ which is approximately an 12% reduction. In the case of GaN-on-sapphire stacks with $TBR = 10 \text{ m}^2\text{K/GW}$, GaN thermal conductivity near the hotspot plummets 45%, from $160 \text{ W/m}\cdot\text{K}$ to $\sim 85.5 \text{ W/m}\cdot\text{K}$.

To quantify the impact of minimizing thermal resistance through GaN layer thickness optimization, the amount of hotspot temperature reduction achieved through a diamond substrate device with optimized GaN layer thickness compared to a device with reference thickness (i.e. $t_{\text{GaN}} = 4 \text{ }\mu\text{m}$) is plotted under various power dissipation levels (from 1 to 8 W) in Figure 4.8. The dissipated power is limited to 8 W not to exceed hotspot temperature of 800 K for GaN material stability [26]. As seen in Figure 4.8, the temperature reduction increases with dissipated power for

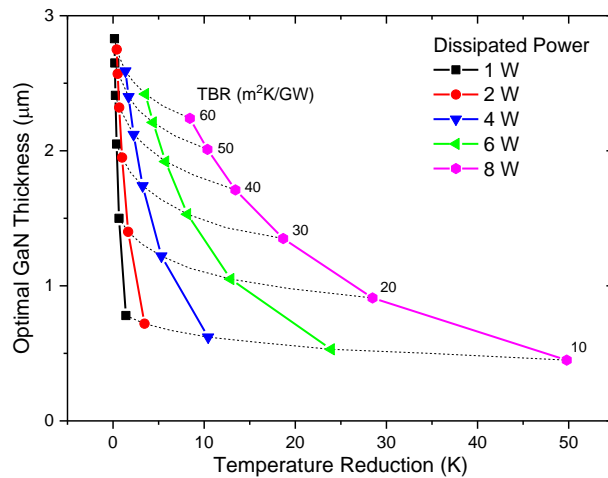


Figure 4.8. Temperature reduction with thickness optimization as a function of dissipated power and various TBR values for GaN-on-diamond stack. The temperature reduction is calculated as the temperature difference between the device with optimal GaN layer thickness and a device with GaN layer thickness of $4 \text{ }\mu\text{m}$. The arrow direction indicates decreasing TBR.

all TBR values, and is maximized when TBR is smallest (i.e., $\text{TBR} = 10 \text{ m}^2\text{K/GW}$). Optimizing the GaN layer thickness has a greater effect when the TBR is smaller due to the thermal conductivity reduction in GaN and substrate material under elevated temperatures. It is important to note that judging by the steeper slope of the curves for smaller TBRs, setting equally distanced t_{GaN} points as the reference for each case would result in the same conclusion. Overall, this work shows that temperature reduction with thickness optimization becomes more prominent as the dissipated power increases, and that it is critical to minimize TBR. Additionally, from the analysis of Figure 4.7 it is shown that the optimal GaN layer thickness shrinks as the dissipated power increases and the TBR decreases. For GaN-on-diamond stack (with a heat source length of 10 nm), the optimal GaN layer thickness, under dissipated power level of 8 W and GaN-diamond TBR of $10 \text{ m}^2\text{K/GW}$, is around 500 nm.

Although the device structure investigated in this work has a thickness, length, and width, since there is no structural variation to the width direction, the simulation domain can be considered 2-D. The width of 1 mm was assigned for simplicity so that the units typically used for power levels of RF power amplifiers, watts per millimeter (W/mm), could be derived easily. However, as heat can flow in three dimensions in real devices, the validity and accuracy of 2-D simulation results needs investigation. Here, simulation results of a 3-D structure are shown to prove the validity and accuracy (within few percent) of 2-D device simulation.

Figure 4.9 shows (a) the 3-D device structure, (b) temperature profile along the surface under the heat source in the z -axis direction, (c) temperature profile from the center (2-D and 3-D) and edge of the heat source to the heat sink in the y -axis direction, and (d) maximum temperature dependence on GaN layer thickness.

The structure is composed of a varying thickness GaN layer on top of a 300- μm -thick diamond substrate with a TBR = 10 $\text{m}^2\text{K/GW}$ at the interface. The device width is 150 μm and heat source

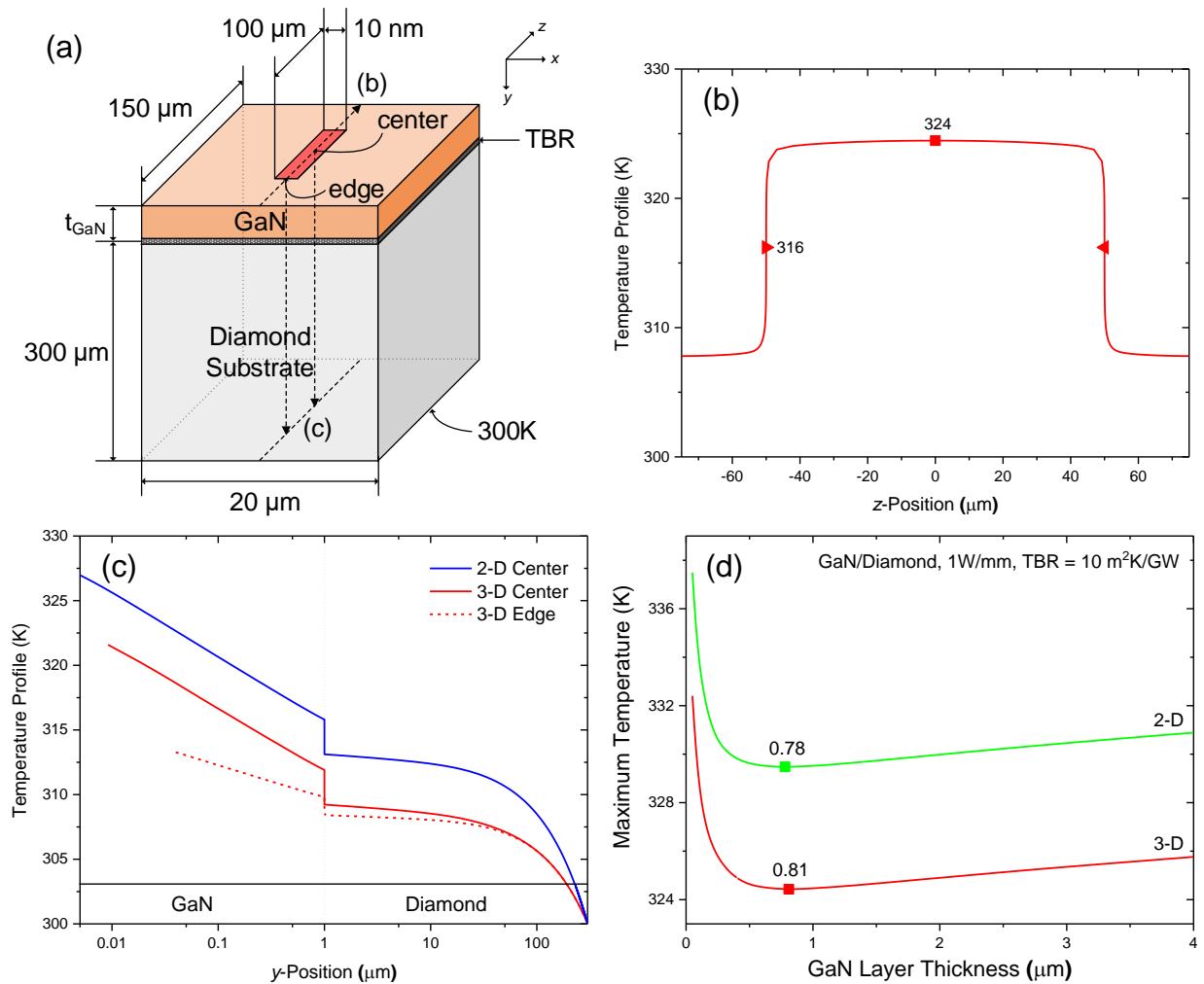


Figure 4.9. (a) The 3-D device structure, (b) temperature profile along the surface under the heat source in the z -axis direction, (c) temperature profile from the center (2-D and 3-D) and edge of the heat source to the heat sink in the y -axis direction, and (d) maximum temperature dependence on GaN layer thickness.

width is 100 μm allowing z -direction heat flow. Total dissipated power is set to 0.1 W so that the dissipated power density is identical to the 2-D case (i.e., 1 W/mm).

Figure 4.9 (b) shows the temperature profile in the z -axis direction. The GaN layer thickness is 1 μm . The maximum temperature is at the center of the device ($z = 0$, marked as square) and as we move towards the edge of the heat source ($z = \pm 50$, marked as triangles), the temperature reduces due to the heat flow in the z -direction towards the region where there is no heat source on top.

Figure 4.9 (c) shows the temperature profile of the 3-D structure in the y -direction at the center (red straight line) and edge (red dashed line) of the heat source. The temperature drop at $y = 1$ is due to the TBR at the interface. The curves terminate at different points due to meshing difference, but the trend should be similar as it gets closer to the surface. This graph also shows that the maximum temperature at the surface (right under the heat source edge) is lower than that at the center due to the 3-D nature of the heat flow. Also, the temperature profile from the 2-D simulation is plotted together (blue straight line) for comparison. The 2-D simulation tends to overestimate the temperature, but the overall trend appears similar to the results of the 3-D simulation.

Figure 4.9 (d) shows the maximum temperature dependence on GaN layer thickness for 2-D and 3-D structures. The absolute temperature difference between the 2-D case and 3-D case is approximately 5 K throughout the entire GaN layer thickness range. Also, the optimal GaN layer thickness difference between the two cases is less than 0.05 μm , showing that 2-D simulation results can be efficiently used to find the optimal GaN thickness of 3-D devices.

4.7 Conclusion

In conclusion, we have studied via TCAD Sentaurus the effects of heat source length, GaN layer thickness, substrate choice, TBR, and dissipated power on the thermal resistance and hotspot temperature of GaN / substrate stacks. The GaN/substrate thermal resistance is shown to have minima when the heat source is localized and a non-zero TBR exists at the GaN/substrate interface. The GaN layer thickness is optimal when it is thick enough to prevent heat crowding and thin enough to keep the thermal resistance small. Temperature-dependent conductivity is shown to be critical in the thermal studies of GaN / substrate stacks. Temperature rise in the GaN layer causes the GaN thermal conductivity to drop (e.g. for optimized GaN-on-sapphire stack with $TBR = 10 \text{ m}^2\text{K/GW}$ and 0.3 W of dissipated power, the drop was from 160 W/m·K to ~85.5 W/m·K) and increases the effective size of the heat source. This increase leads to an optimal GaN layer thickness that is smaller than the value predicted using temperature-independent thermal conductivity. High dissipated power through GaN/diamond stacks shows that the effect of GaN layer thickness optimization becomes more significant as dissipated power increases and TBR decreases. As the dissipated power increases to 8 W, the optimal GaN layer thickness decreases to 500 nm (for $TBR = 10 \text{ m}^2\text{K/GW}$), and by optimization the heat source temperature can be reduced by 50 °C. Overall, pushing the GaN HEMTs towards higher power levels ($> 40 \text{ W/mm}$) requires engineering of novel architectures composed of submicron-thick GaN layers on high thermal conductivity substrates (e.g. diamond) with a low TBR.

CHAPTER 5 THERMAL CONDUCTIVITY OF GaN

As a wurtzite crystal, GaN shows uniaxial characteristics such as anisotropic mobility and saturation velocity. Another uniaxial property that may affect the electronic performance of GaN-based transistors is the anisotropic thermal conductivity. For the investigations of thermal resistance optimization of GaN-based devices, it was assumed that the thermal conductivity is isotropic. However, based on theoretical calculations of direction-dependent sound velocity and elastic constants [97], [98], GaN is expected to reveal anisotropic thermal conductivity. Nevertheless, such anisotropy has never been observed.

5.1 Time-Domain Thermoreflectance (TDTR)

Time-domain thermoreflectance (TDTR) [99], [100], [101] is an optical and non-destructive method for measuring thermal conductivity and thermal boundary resistance of materials and their interfaces. Figure 5.1 shows the TDTR setup located at the laser facility in the Materials Research Laboratory (MRL). It is a pump-probe laser technique in which the probe beam strikes the sample,

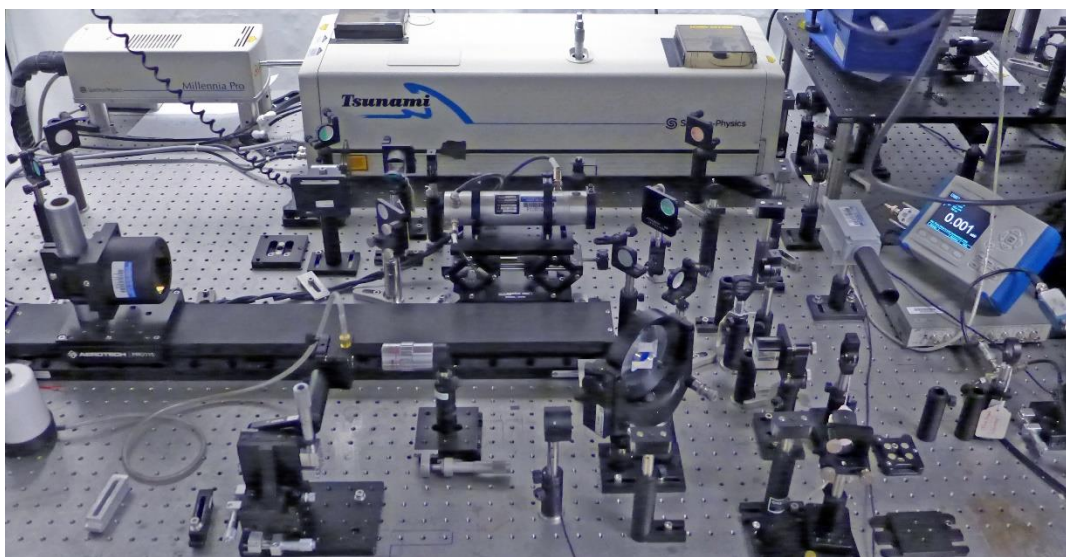


Figure 5.1. Photograph of TDTR measurement setup.

and the pump beam, delayed relative to the probe beam, is reflected from the sample and has its intensity recorded. The thermorefectance coefficient of the sample is proportional to the change in the material's reflectivity induced by the pump beam. By measuring the change in reflectance in the probe beam over a delay time, a characteristic figure of how the heat dissipates in the sample is generated over picosecond time delays. Figure 5.2 is a schematic diagram of the TDTR system showing the laser beam paths and the position of the optics.

As the name of the technique implies, the TDTR method is a transient heat flow method. Compared to more traditional steady-state heat flow methods, the transient heat flow method has advantages including that (1) the actual temperature measurement inside the sample is not required, (2) insulation with the environment can be minimized, and (3) it can be used on very thin samples.

The difference between electrical and thermal properties measurements is that electric current can be controlled such that it only passes through regions of interest whereas heat will always leak through undesired paths. In thermal conductivity measurements of materials using steady-state

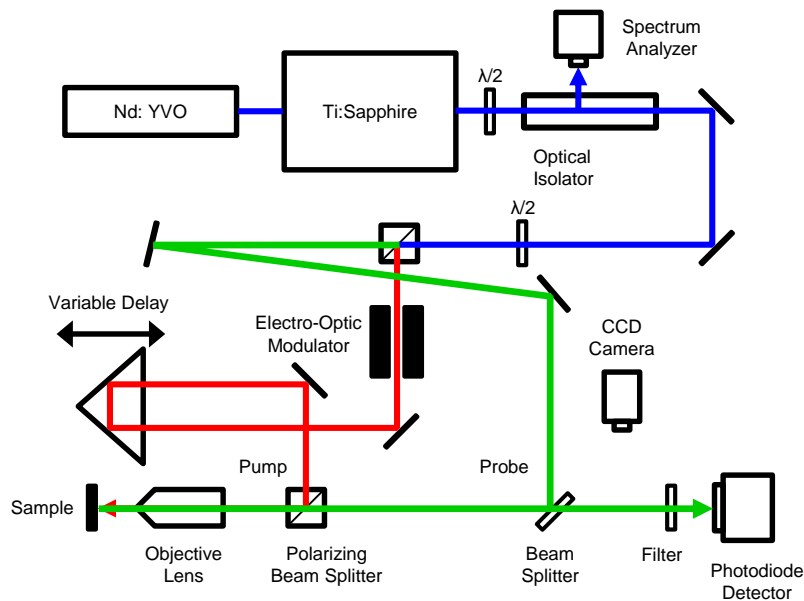


Figure 5.2. Schematic of the TDTR measurement setup with its laser beam paths. The red and green lines show the pump and probe laser beam paths, respectively.

heat flow, this calls for excessive heat insulation around the material of interest to ensure heat current is only flowing through the material [87]. In the TDTR technique, a small area (or volume) of the material is irradiated with an optical laser power which is then transformed into a heat power via the metal transducer layer. The small amount of heat power is dissipated through the material in a time scale of nanoseconds, excluding the need for any thermal insulation. Also, because the technique does not require the temperature profile of the sample to extract the thermal conductivity, the sample need not be thick. The simplest traditional methods extract the thermal conductivity of materials by observing the temperature difference between two temperature probes assuming one-dimensional heat flow. To obtain an accurate result, the temperature difference between the probes must be large enough, which in turn means that the sample has to be thick enough to induce a temperature difference. In comparison, the TDTR does not require the sample to be thick: even a thickness of few hundreds of nanometers is sufficient to obtain accurate thermal conductivity measurements provided the appropriate system setup is used.

The laser used in the experimental setup is a Ti:sapphire laser mode locked at a repetition rate of 80 MHz (repetition time is 12.5 ns), with a pulse width ~ 150 fs. The wavelength is set to 783 nm and is split into a pump beam and a probe beam using sharp edge filters. The optical isolator installed at the aperture of the laser prevents any reflected beam shooting back into the aperture. The electro-optical modulator (EOM) modulates the pump laser frequency typically to 11 MHz in order to isolate the signal from environmental noise by coupling through the lock-in amplifier. There is also an optical chopper installed at the probe beam path which runs at 200 Hz to suppress coherent pickup during data collection. The interval between the arrival of the pump laser beam and the probe laser beam at the sample is adjusted by the delay stage. In the setup, the pump beam goes through the delay stage rather than the probe beam. This configuration has an advantage over

the setup with the delayed probe beam in that the probe beam radius is not affected by the delay stage. Both beams are reflected off the sample and are passed through the final steep pass filter right before the photodiode to remove the pump beam signal.

The photodiode picks up the reflected probe beam signal and passes it through a RLC band-pass filter to the lock-in amplifier. The band-pass filter only allows signals with frequency very close to the EOM frequency to pass. This works to eliminate noise and removes the effects of higher order harmonics present in the signal due to the rectangular wave modulation of the EOM.

The signal is amplified and fed to the lock-in amplifier which outputs the signal in an in-phase and out-of-phase signal relative to the set frequency. The lock-in amplifier basically multiplies the input signal with a reference signal and outputs a set of low-pass filtered signals. Assuming the signal picked up by the detector is

$$V_L \sin(\omega_L t + \theta_L) \quad (5.1)$$

and the reference signal is

$$V_{\text{ref}} \sin(\omega_{\text{ref}} t + \theta_{\text{ref}}) \quad (5.2)$$

then the multiplied signal may be expressed as

$$\begin{aligned} & V_L V_{\text{ref}} \sin(\omega_L t + \theta_L) \sin(\omega_{\text{ref}} t + \theta_{\text{ref}}) \\ &= V_L V_{\text{ref}} \frac{1}{2} \cos[(\omega_L - \omega_{\text{ref}})t + (\theta_L - \theta_{\text{ref}})] - V_L V_{\text{ref}} \frac{1}{2} \cos[(\omega_L + \omega_{\text{ref}})t + (\theta_L + \theta_{\text{ref}})] \end{aligned} \quad (5.3)$$

where the resultant signal can be separated into two signals with frequencies $\omega_L - \omega_{\text{ref}}$ and $\omega_L + \omega_{\text{ref}}$. The signals picked up by the detector may include signals with various frequencies which may be expressed as linear combinations of (5.1). Since the reference signal is set by a function

generator, the frequency ω_{ref} is fixed to a value. If the signal (5.3) is sent through a low-pass filter, the obtained signal will become

$$V_L V_{\text{ref}} \cos[(\omega_L - \omega_{\text{ref}})t + (\theta_L - \theta_{\text{ref}})] = V_L V_{\text{ref}} \cos(\theta_L - \theta_{\text{ref}}) \quad (5.4)$$

where ω_L is now identical to ω_{ref} due to the filter. Therefore, the lock-in amplifier only outputs signals with a frequency identical to that of the reference signal. This signal is recorded and can be understood as the response to the pump beam signal without any noise.

In the experimental setup, the lock-in amplifier produces an output signal that was processed with a reference signal that has a 90° phase difference as well. This output may be expressed as

$$V_L V_{\text{ref}} \sin[(\omega_L - \omega_{\text{ref}})t + (\theta_L - \theta_{\text{ref}})] = V_L V_{\text{ref}} \sin(\theta_L - \theta_{\text{ref}}). \quad (5.5)$$

The cosine signal (5.4) is called the in-phase signal and the sine signal is called the out-of-phase signal. By adjusting the phase of the reference signal to $\theta_L = \theta_{\text{ref}}$, in theory, we can completely eliminate the out-of-phase signal and obtain the pure VL amplitude DC signal. However, in practice, the out-of-phase signal is not always removed because of the effect of the pump pulse from the previous time step. Conversely, the out-of-phase signal can be used to monitor the heat accumulation effect on the in-phase signal and to remove its impact from the in-phase signal to obtain a signal that can be analyzed more appropriately.

After acquiring measurement data from the TDTR technique, the results are analyzed using a program that models the heat flow in layered materials. The thermal conductivity and/or thermal boundary resistance of materials (and their interfaces) are obtained by fitting the data curve to the model.

Here, the most fundamental formalism is briefly discussed. A detailed description of the model can be found in other literature [99], [102]. The pump laser intensity, assuming a Dirac delta function for the pulses, is expressed in real space and time domain as

$$p_1(r, t) = \frac{2A_1}{\pi w_1^2} \exp\left(-\frac{2r^2}{w_1^2}\right) e^{i\omega_0 t} \sum_{n=-\infty}^{\infty} \delta(t - nT_s - t_0) \quad (5.6)$$

where A_1 is the average power of the pump beam, w_1 is the $1/e^2$ radius of the laser beam, ω_0 is the pump beam modulation frequency, and T_s is the laser repetition time. The frequency domain expression of the pump laser intensity can be obtained by using Hankel transform in space and Fourier transform in time:

$$P_1(k, \omega) = A_1 \exp(-\pi^2 k^2 w_1^2 / 2) \omega_s \sum_{n=-\infty}^{\infty} \delta(\omega - \omega_0 - n\omega_s) e^{-in\omega_s t_0} . \quad (5.7)$$

The surface temperature response in the frequency domain is the product of the heat input P_1 and the thermal response function of the system $G(k, \omega)$ and is expressed as

$$\Theta(k, \omega) = P_1(k, \omega) G(k, \omega) . \quad (5.8)$$

The temperature distribution of the surface is obtained by the inverse Hankel transform of the $\Theta(k, \omega)$ function which is given by

$$\Theta(r, \omega) = \int_0^{\infty} P_1(k, \omega) G(k, \omega) J_0(2\pi kr) 2\pi k dk . \quad (5.9)$$

The in-phase V_{in} and out-of-phase V_{out} signals output by the lock-in amplifier can be expressed as

$$V_{in} = \text{Re}[\Delta R(t)] = \frac{1}{2} \sum_{n=-\infty}^{\infty} [\Delta T(\omega_0 + n\omega_s) + \Delta T(-\omega_0 + n\omega_s)] \exp(in\omega_s t_d) , \quad (5.10)$$

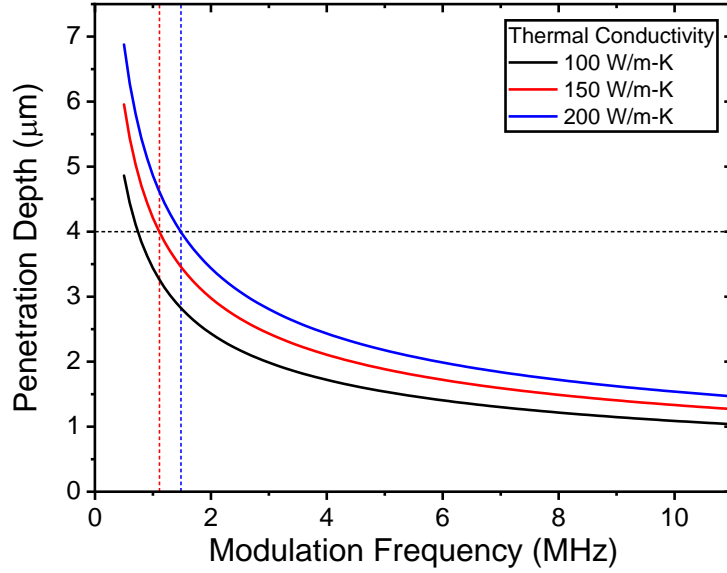


Figure 5.3. Thermal penetration depths d_p as a function of modulation frequency with thermal conductivity of 100, 150, and 200 W/m-K.

$$V_{\text{out}} = \text{Im}[\Delta R(t)] = -\frac{i}{2} \sum_{n=-\infty}^{\infty} [\Delta T(\omega_0 + n\omega_s) - \Delta T(-\omega_0 + n\omega_s)] \exp(in\omega_s t_d). \quad (5.11)$$

The thermal penetration depth can be controlled by adjusting the modulation frequency of the pump laser beam. The estimated depth is expressed as

$$d_p = \sqrt{\frac{\kappa}{\pi f_{\text{mod}} C}} \quad (5.12)$$

where κ is the thermal conductivity of the material, f_{mod} is the modulation frequency of the TDTR system, C is the volumetric heat capacity of the material. For thermal conductivity measurements of thin layers, depending on the modulation frequency, the heat generated by the pump laser may or may not reach the layers beneath the material of interest. In the case of GaN grown on top of foreign substrates, the defectivity also has a dependence of the GaN layer thickness. To obtain accurate analysis results, the modulation frequency should be selected such that thermal energy is reaching the material or interface of interest. Figure 5.3 shows the thermal penetration depths



Figure 5.4. Schematic diagram of the heat flow that is analyzed. At left, the laser spot size is larger than the thermal penetration depth. At right, the spot size is comparable to the penetration depth.

calculated using Eq. (5.12) as a function of modulation frequency with three different thermal conductivities. In this calculation, the volumetric heat capacity is assumed to be that of GaN which is $C = 2.64 \text{ J/cm}^3\text{K}$.

The laser spot size must also be considered while adjusting the modulation frequency. The thermal transport model used to analyze TDTR experimental data assumes a one-dimensional heat flow. To assure this is actually the case, the laser spot size w_1 must be considerably larger than the thermal penetration depth. The one-dimensional heat flow condition can only be met when the lateral heat flow is negligible compared to the vertical heat flow. A schematic diagram is shown in Figure 5.4 to depict the situation. At left, the laser spot size is larger than the thermal penetration depth. At right, the spot size is comparable to the penetration depth. The laser spot size is usually adjustable through choosing objective lenses with different magnifications.

5.2 Aluminum Film Characterization

One of the key material properties that determines the accuracy of the TDTR measurements is the thermal properties of the aluminum film sputtered on top of the sample of interest. Generally, the preferable properties of the metal film would be high absorption and reflection rate, high thermorefectance coefficient, high thermal conductivity, high volumetric heat capacity, low surface roughness, and high reproducibility.

5.2.1 X-Ray Reflectivity (XRR)

X-ray reflectivity (XRR) is a method used to measure thickness of thin films by X-ray interference. The difference in material density reflects different portions of the incident X-ray which results in a fringing intensity at different reflection angles. Generally, the periodicity of the resultant intensity curve decreases with thickness of the film. The maximum thickness that can be measured by XRR is dependent on the density of the film but is usually < 200 nm. The decay rate of the intensity curve may also be modeled to extract the density of the material and the interface roughness (see Figure 5.5).

Here, in relation with the TDTR method, the XRR technique is used to determine the thickness of the transducer layer or the aluminum film which is deposited on top of the sample. As shown in Figure 5.6, the TDTR measurement has the largest sensitivity in the heat capacity and thickness of the aluminum film. Therefore, it is critical to use the correct thickness in the analysis of TDTR data to obtain accurate thermal conductivity.

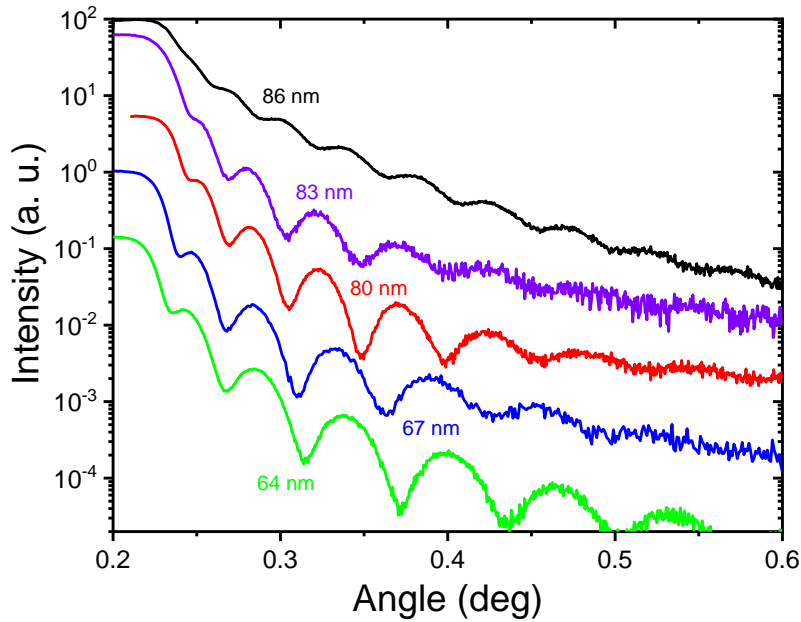


Figure 5.5. XRR measurement data showing results obtained from different samples with different thicknesses. Through detailed modeling, not only the thickness of the film but also the density of the material and interface roughness can be extracted.

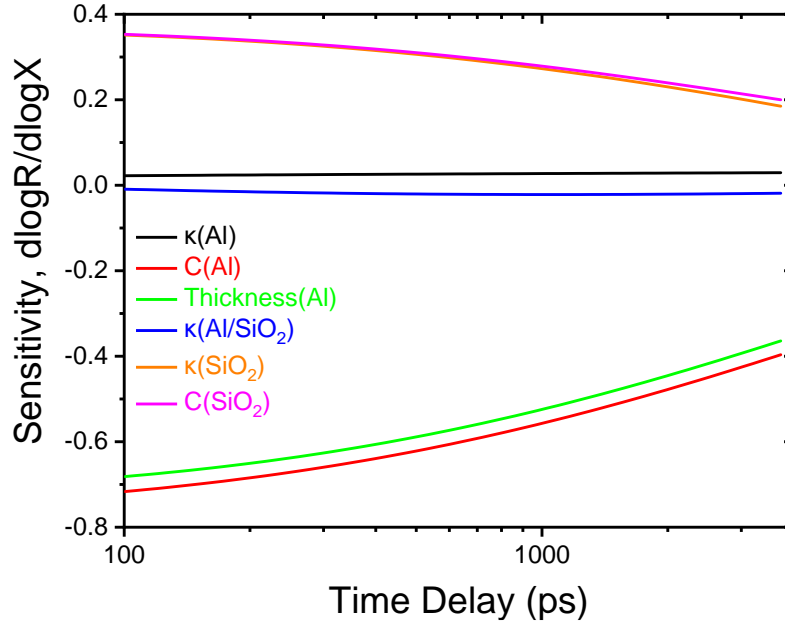


Figure 5.6. Sensitivity plot showing parameters that can be altered in TDTR analysis. The sensitivity plot is generated for an Al/SiO₂/Si system with thicknesses approximately 70 nm, 500 nm, and 500 μm, respectively. The parameters with the largest influence are heat capacity and thickness of aluminum shown in red and green curves.

The objective of the XRR measurements is to obtain an aluminum thickness measurement result that is consistent with other thickness measurement techniques (such as cross-sectional SEM imaging and picosecond acoustics) along with the already known sputtering deposition rate.

5.2.2 Four-Point Probe Resistivity

The four-point probe technique is a method used to measure the electrical conductivity of samples. For particular metal films, the thermal conductivity is mostly determined by the energy transfer due to electrons and hence the two conductivities are closely related by the Wiedemann-Franz law:

$$\frac{\kappa}{\sigma} = LT \quad (5.13)$$

where κ is the thermal conductivity, σ is the electrical thermal conductivity, T is temperature and L is the Lorenz number generally given as $L = 2.44 \times 10^{-8} \text{ W}\Omega/\text{K}^2$. Through the determination of

electrical conductivity, thermal conductivity can be extracted readily using the temperature-independent Lorenz number.

5.2.3 Scanning Electron Microscopy (SEM)

The surface scanning electron microscopy (SEM) technique is a solid method to investigate the surface morphology of the aluminum film. Although, to obtain more quantitative results, atomic force microscopy (AFM) is required, SEM is advantageous in that it is quick to perform and readily yields qualitative information of the sample.

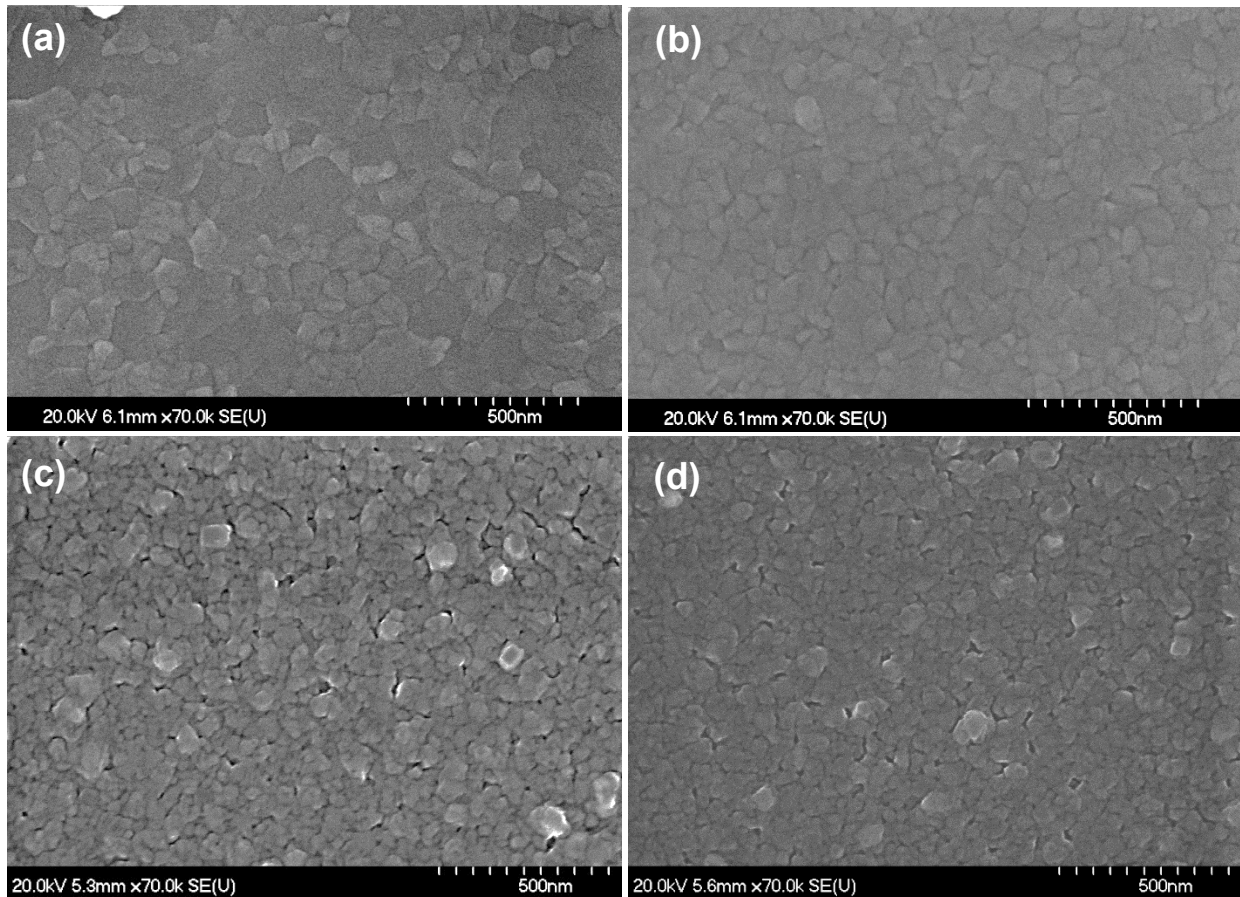


Figure 5.7 Surface scanning electron microscopy (SEM) images of sputtered aluminum using (a), (b) Sputter-1 and (c), (d) AJA3. The aluminum was sputtered onto samples of (a) Al_2O_3 , (b) GaN on Al_2O_3 , (c) and (d) SiO_2 on Si substrates. All images were taken with the same resolution and accelerating voltages.

Shown in Figure 5.7 are the surface SEM images of aluminum films sputtered using Sputter-1 [(a) and (b)], and AJA 3 [(c) and (d)]. The aluminum was sputtered onto samples of (a) Al_2O_3 , (b) GaN on Al_2O_3 , (c and d) SiO_2 on Si. Compared to (c) and (d), samples (a) and (b) show larger grain size and smoother surfaces. Four-point probe measurements on these samples also revealed that (a) and (b) films have higher thermal conductivities ($\sim 186 \text{ W/m-K}$) than (c) and (d) films ($\sim 80 \text{ W/m-K}$). Hence, coupled with the four-point probe measurements, SEM surface images were able to successfully determine high-quality aluminum films that are adequate for TDTR experiments.

5.3 Impact of Dislocations on Thermal Conductivity

Parts of this section are reproduced from [103], with the permission of AIP Publishing.

5.3.1 Introduction

Gallium nitride based semiconductors are of great interest in the optoelectronics and electronics community. In solid-state lighting, (In)GaN-based light emitting diodes (LEDs) have revolutionized general lighting and are driven with power densities exceeding 100 W/cm^2 [104]. In emerging wireless networks, (Al)GaN/GaN high-electron-mobility transistors (HEMTs) are leading in 5G efforts and their power densities are projected to reach 60 W/mm [62]. The strong interatomic bonding energy (9.3 eV/atom) leads to high thermal stability and high thermal conductivity (theoretical upper bound being $> 336 \text{ W/m-K}$) [76], [105] supporting the material's use in applications that demand high-power-density operation [41], [106]. While these projections are valid under ideal conditions, the vast majority of the available GaN are far from being a perfect crystal; reported values ranging from 110 to 269 W/m-K suggest the impact of the crystal imperfections including dopants, impurities, isotopes, carrier concentrations, vacancies, point defects, and threading dislocations on GaN thermal conductivity [81], [107], [108], [109], [110],

[111], [112]. With higher crystalline quality GaN grown by techniques such as hydride vapor phase epitaxy (HVPE) [113] and ammonothermal method [114] becoming more available, recently reported GaN thermal conductivity shows progress toward reaching its theoretical limit [109], [110], [112]. But most GaN layers are grown on non-native substrates for reduced cost, high scalability, and integrated functionality, and a complete study of such heterogeneously grown GaN is lacking [115]. It is thus important to explore thermal conductivities of such GaN-on-foreign-substrates, which could also take advantage of existing CMOS integration technology and their large scalability [115], [116], so that LED and HEMT researchers can create accurate thermoelectrical modeling for thermal management studies.

5.3.2 GaN Thermal Conductivity Measurement Using TDTR

Reported here is a time-domain thermoreflectance (TDTR) study on the thermal conductivity of GaN. Three c-plane GaN samples are studied: (1) 350- μm -thick freestanding GaN grown by hydride vapor phase epitaxy (HVPE), (2) 350- μm -thick freestanding GaN grown by high-nitride-pressure (HNP) growth method [117], (3) 4.5- μm -thick GaN grown on sapphire substrate by metal-organic chemical vapor phase deposition (MOCVD), and (4) 5- μm -thick GaN grown on Si(111) substrate by MOCVD with step-graded $\text{Al}_x\text{Ga}_{1-x}\text{N}$ and AlN buffer layers in between [i.e., 5- μm -thick GaN / 400-nm-thick $\text{Al}_{0.33}\text{Ga}_{0.67}\text{N}$ / 290-nm-thick $\text{Al}_{0.60}\text{Ga}_{0.40}\text{N}$ / 200-nm-thick $\text{Al}_{0.82}\text{Ga}_{0.18}\text{N}$ / 240-nm-thick AlN / Si(111)] [118], [119].

In the TDTR setup, a mode-locked Ti:sapphire laser that generates 783 nm laser pulses at an 80 MHz repetition rate is used as the light source. The pulses are split into a pump and probe beam. The pump beam is modulated by an electro-optical modulator (EOM) and passes through a mechanical delay stage where its arrival time at the sample is controlled. The modulation frequency f_{mod} is typically set to ~ 10 MHz and the mechanical delay stage introduces up to 3.6 ns

of delay with respect to the probe beam. The probe beam is modulated by a chopper that operates at 200 Hz to suppress coherent pickup. The reflected probe beam is collected by a fast-response photodiode detector, which converts the optical signals into electrical signals. A radio-frequency (RF) lock-in amplifier is then used to pick up the signal. The RF lock-in amplifier has outputs of an in-phase (V_{in}) signal and an out-of-phase (V_{out}) signal at the modulation frequency. The ratio $R = V_{in}/V_{out}$ is fit to the one-dimensional thermal diffusion transport model from an analytical solution for heat flow in a multilayered structure [99].

The thermal transport model uses thermal conductivity κ , volumetric heat capacity C_P , and thickness of each layer for its calculation. In the model calculations, volumetric heat capacities taken from literature and layer thicknesses are measured using cross-sectional scanning electron microscopy (SEM). In addition to the material stack of interest, properties of the metal transducer layer (aluminum in this work) and thermal boundary resistance (TBR) of interfaces are also considered in the model. For the sake of modeling, interfaces are assumed to have a negligible volumetric heat capacity of $C_P = 0.1 \text{ J/cm}^3\text{K}$ and a thickness of 1 nm. Once the thermal conductivity of this interface layer κ_i is obtained, TBR can be calculated as $(1 \text{ nm})/\kappa_i$ which is commonly expressed in the units of $\text{m}^2\text{K/GW}$. Fitting is done by minimizing the sum of the squares of error between the model calculation and measurement data while sweeping through a range of κ and TBR (transducer/material) [120].

A thin layer of aluminum is deposited, by dc magnetron sputtering, on top of the sample to serve as a transducer [121]. The aluminum film thickness is approximately 100 nm and varies slightly across different samples. The thickness is obtained from the picosecond acoustics echo observed at the short time delay ($< 100 \text{ ps}$) part of the TDTR measurement [122]. Assuming a longitudinal speed of sound $v_l = 6.42 \text{ nm/ps}$ [123], the thickness of the aluminum film may be obtained while

considering an additional 3-nm-thick native aluminum oxide layer, i.e., $t_{\text{Al}} = 6.42 \times t_1 / 2 + 3$, where t_1 is the time of echo. The thickness of the film is also verified using X-ray reflectivity (XRR) measurements. The thermal conductivity of the aluminum film is measured using the four-point probe technique. With the Wiedemann–Franz law, the electrical resistivity may be converted into thermal conductivity as $\kappa = LT/\rho$, where $L = 2.445 \times 10^{-8} \text{ W}\Omega/\text{K}^2$ is the Lorenz number. The typical thermal conductivity obtained is 180 W/m-K. The volumetric heat capacity is taken from literature as $C_{\text{P,Al}} = 2.43 \text{ J/cm}^3$ [124].

To ensure the thermorefectance of the transducer can be kept constant in the analysis and to obtain the room-temperature thermal conductivity of the material of interest, the steady-state temperature increase due to the pump and probe pulses must be small (usually less than 10 K). A rough estimation of the steady-state temperature increase may be calculated by [99]

$$\Delta T = \frac{A_0}{2\sqrt{\pi}w_0\kappa} \quad (5.14)$$

where A_0 is the laser power absorbed by the sample, w_0 is the $1/e^2$ radius of the pump and probe beam, and κ is the thermal conductivity of the material. A more accurate calculation may be performed by considering the transducer layer and the substrate material that lies underneath the material of interest, using equations provided in Ref. [99].

Whether an unknown thermal property can be measured with good accuracy from the experiments can be quantitatively estimated by calculating the sensitivity coefficient

$$S_\xi = \frac{\partial \ln R}{\partial \ln \alpha} = \frac{\alpha}{R} \frac{\partial R}{\partial \alpha}. \quad (5.15)$$

Here the sensitivity coefficient S_α represents how sensitive the measured ratio signal R is to the parameter α . Both the magnitude and the sign of S_α have specific meanings, i.e., 1% increase in

the parameter α will result in $S_\alpha \times 1\%$ increase in the ratio signal R . Throughout our measurement and analyses of this work, the sensitivity of the fitting parameters is closely monitored to ensure the fittings are valid.

The laser spot size and modulation frequency are important system parameters in TDTR measurements. For the temperature gradient to be one-dimensional in the through-plane direction and thus predominantly depend on the through-plane thermal conductivity κ_z , the laser spot size must be significantly larger than the thermal penetration depth $d_{p,z}$ which is expressed as $d_{p,z} = \sqrt{\kappa_z / \pi f_{\text{mod}} C_P}$ [125].

Figure 5.8 shows the ratio of laser spot size (defined by the $1/e^2$ radius of the laser) to thermal penetration depth as a heat map. For our TDTR measurements, we typically choose a combination such that the ratio is larger than a factor of 4 to guarantee accurate analysis [126]. The laser spot

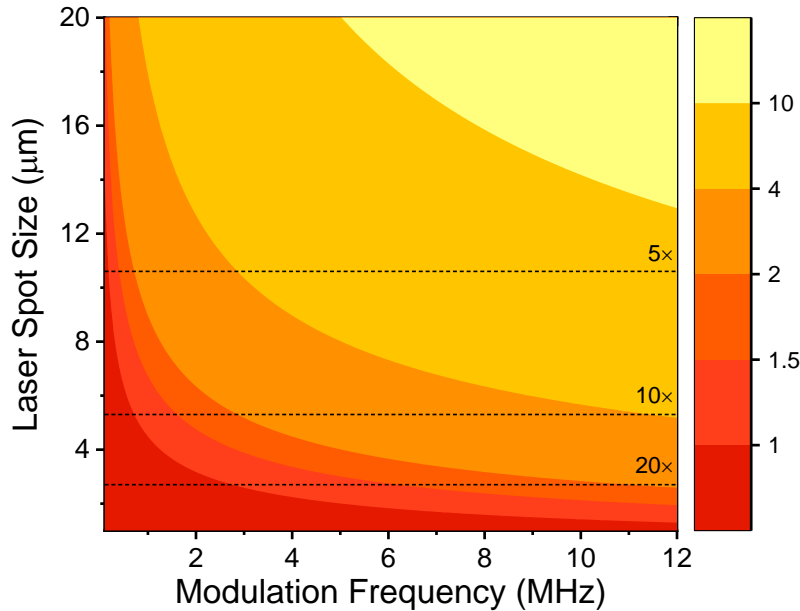


Figure 5.8. Heat map of laser spot size versus modulation frequency. Laser spot size must be larger than thermal penetration depth to assure heat flow is mostly one dimensional and the model is properly capturing the physics. For accurate analysis, the ratio should be larger than 4. Also shown together (as horizontal dashed lines) are the laser spot sizes obtained in the system with objective lenses of 5, 10, and 20 times magnification. Thermal penetration depth is calculated based on $\kappa = 175$ W/m-K and $C_{P,\text{GaN}} = 2.64$ J/cm³K for a GaN sample with moderate thermal conductivity.

size is usually adjustable through the use of objective lenses with different magnifications. The laser spot sizes obtained in the system with objective lenses of 5, 10, and 20 times magnification are shown as horizontal dashed lines. Here, the thermal penetration depth is calculated based on a moderate GaN thermal conductivity of $\kappa_{\text{GaN}} = 175 \text{ W/m-K}$ and volumetric heat capacity of GaN $C_{P,\text{GaN}} = 2.64 \text{ J/cm}^3\text{K}$ taken from the literature [127], [111], [128]. While a modulation frequency in the range of $4 < f_{\text{mod}} < 11 \text{ MHz}$ with the $5\times$ objective lens is sufficient for our measurements according to Figure 5.8, the thickness of the GaN layers of our samples further restricts the selection of modulation frequencies. In the TDTR measurements, a modulation frequency of $f_{\text{mod}} = 11 \text{ MHz}$ is used to assure the thermal penetration depth is smaller than the GaN layer thickness ($> 4.5 \mu\text{m}$) of our samples.

Figure 5.9 shows TDTR data of the freestanding GaN sample measured with different laser powers (black, red, magenta, blue, and orange correspond to total powers of 20, 24, 32, 40, and 48 mW, respectively). Plotted in (a) and (b) are the in-phase V_{in} and out-of-phase V_{out} signals recorded with a total power of 20, 24, and 32 mW. The pump and probe powers are typically set equal to each

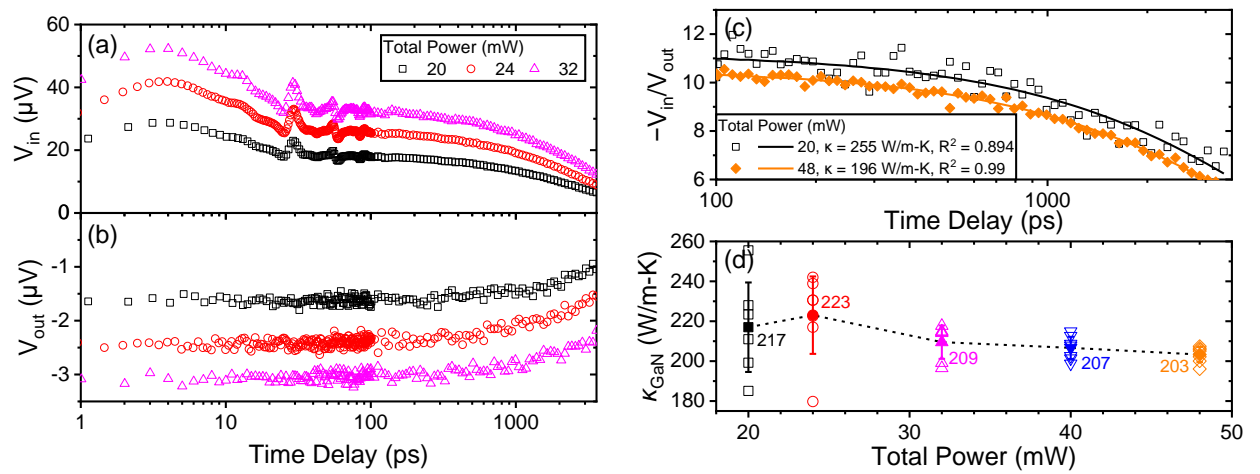


Figure 5.9. TDTR measurement results of HNP GaN. (a) In-phase signal V_{in} , (b) out-of-phase signal V_{out} , (c) ratio $-V_{\text{in}}/V_{\text{out}}$ and their fitting results, and (d) thermal conductivity from multiple measurements and average values with five different laser powers (20, 24, 32, 40, and 48 mW). At higher power, noise signals included in the relatively small out-of-phase signal have smaller effect on the analysis of the ratio.

other. In short time delays (< 100 ps), the signals are recorded with smaller intervals (0.5 ps) to extract the aluminum film's thickness with higher accuracy. In an ideal case, the power of the pump and probe beams should not affect the result since the ratio $-V_{in}/V_{out}$ signal is analyzed. However, due to the noise incorporated in the signal readings (mostly in the V_{out} signal), increasing the total power up to a level where the ratio signal is not severely distorted by the noise is practical for reducing the error in thermal conductivity. Figure 5.9 (c) shows the ratio signal data (symbols) and model calculation (solid lines) results for powers of 20 and 48 mW. The goodness of fitting assessed by the coefficient of determination R^2 is significantly larger for the measurement using 48 mW laser power. More importantly, the extracted thermal conductivity shows a 30% difference between the two measurements. Figure 5.9 (d) shows the extracted thermal conductivity with different laser powers. The average thermal conductivities (closed symbols) for each power and thermal conductivity extracted from each measurement (open symbols) are shown together. Measurements were done on the same spot of the sample while keeping all conditions equal except for the laser powers. With increasing power, the standard deviation is reduced. As the total power is increased from 20 to 24 mW, the average thermal conductivity increases due to the improved signal-to-noise ratio, but the standard deviation is still quite large; with power of 24 mW, the lowest and highest thermal conductivities measured are 180 and 255 W/m-K, respectively. At powers above 30 mW, the standard deviations are small ($< 5\%$) and the coefficient of determination for each fitting is consistently larger than $R^2 > 0.96$. However, also observed is a slight gradual decrease of thermal conductivity, which is suspected to be due to the steady-state heating of the material. Thus, in our measurements, considering the goodness of fitting, standard deviation in measured thermal conductivity, and the steady-state heating, a power of 32 mW is selected.

Figure 5.10 shows actual TDTR measurement data (open symbols) and thermal transport model calculations along with key experimental parameters for (a) HVPE GaN, (b) HNP GaN, (c) GaN/sapphire, and (d) GaN/Si samples. A good fit is achieved with coefficient of determination (i.e., R^2) > 0.97 and Al/GaN interfaces have consistent TBRs ($\sim 10 \text{ m}^2\text{K/GW}$) across samples. The thermal transport model calculations with $\kappa_{\text{GaN}} \pm 10\%$ are also plotted (dashed lines). Most of the actual TDTR measurement data points are within the $\kappa_{\text{GaN}} \pm 10\%$ curves throughout the entire time delay, indicating that the uncertainties of the measurements are relatively small and that the sensitivities of the κ_{GaN} data are sufficiently large, ensuring a valid fitting. Multiple TDTR

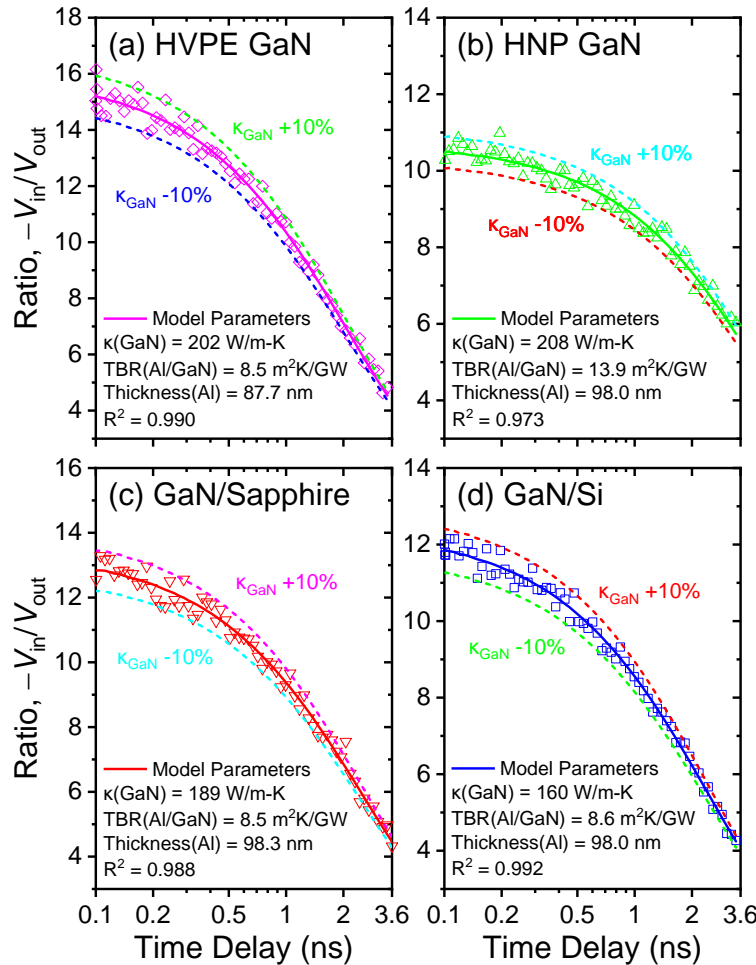


Figure 5.10. TDTR measurement results ($-V_{\text{in}}/V_{\text{out}}$ as a function of time delay) and fitted κ_{GaN} of (a) HVPE GaN, (b) HNP GaN, (c) GaN/sapphire, and (d) GaN/Si. Open symbols indicate measurement data, solid lines indicate thermal transport model calculation (with fitting parameters listed), and dashed lines indicate thermal transport model calculations with $\kappa_{\text{GaN}} \pm 10\%$.

measurements are done on each sample to obtain average κ_{GaN} . The results are tabulated in Table 5.1. HVPE and HNP GaN exhibit a relatively high κ_{GaN} of 204.7 (± 4.6) and 206.6 (± 6.8) W/m-K, respectively, GaN/sapphire exhibits a moderate κ_{GaN} of 191.5 (± 10.5) W/m-K, and GaN/Si exhibits the lowest κ_{GaN} of 164.4 (± 3.2) W/m-K. κ_{GaN} of HVPE and HNP GaN are statistically indistinguishable, but compared to that of the GaN/Si sample, they are larger by $\sim 25\%$.

5.3.3 GaN Material Characterization

To explore the origins of κ_{GaN} differences among the samples, dislocation densities (σ_D) are measured using the cathodoluminescence (CL) and the X-ray diffraction (XRD) technique. Figure 5.11 shows CL images of (a) HVPE GaN, (b) HNP GaN, (c) GaN/sapphire, and (d) GaN/Si samples, taken in panchromatic view with an acceleration voltage of 5 kV. As non-radiative recombination centers, dislocations appear as dark spots which are then counted for density calculations [129]. Five measurements per sample are collected. HVPE GaN, HNP GaN, GaN/sapphire, and GaN/Si samples have an average σ_D of $4.80 (\pm 0.42) \times 10^5$, $3.81 (\pm 0.08) \times 10^6$, $2.43 (\pm 0.20) \times 10^8$, and $1.10 (\pm 0.10) \times 10^9 \text{ cm}^{-2}$, respectively (Table 5.1).

Figure 5.12 shows representative XRD ω scans (rocking curves) in the (a) (0002) symmetric and (b) (10 $\bar{1}$ 2) asymmetric planes of the HVPE GaN, HNP GaN, GaN/sapphire, and GaN/Si samples. Based on the full width at half maximum (FWHM) of the (0002) and (10 $\bar{1}$ 2) ω scans, the screw-type dislocation density σ_{screw} and edge-type dislocation density σ_{edge} can be calculated by the relations [118], [130]:

$$\sigma_{\text{screw}} = \frac{\beta_{(0002)}^2}{4.35b_{\text{screw}}^2} \quad (5.16)$$

$$\sigma_{\text{edge}} = \frac{\beta_{(10\bar{1}2)}^2 - \beta_{(0002)}^2}{4.35b_{\text{edge}}^2} \quad (5.17)$$

where $\beta_{(0002)}$ and $\beta_{(10\bar{1}2)}$ are the FWHM (in units of rad) of the (0002) and $(10\bar{1}2)$ rocking curves, respectively; $b_{\text{screw}} = 0.5185$ nm and $b_{\text{edge}} = 0.3189$ nm are the Burgers vector length of screw- and edge-type dislocations, respectively. The calculated results are tabulated in Table 5.1.

For the GaN/sapphire and GaN/Si samples, both techniques reveal similar σ_D . For the HVPE and HNP GaN samples, XRD estimates a higher σ_D than the CL technique. The discrepancy in this case is most likely due to the limitations of the FWHM-based XRD σ_D calculation model in which it is assumed that the crystal forms a mosaic structure consisting of similar-sized blocks [130], [131]. For samples with low σ_D , the dislocations form in clusters, making it difficult to assume there exists a constant lateral coherence length between dislocations [129], [132].

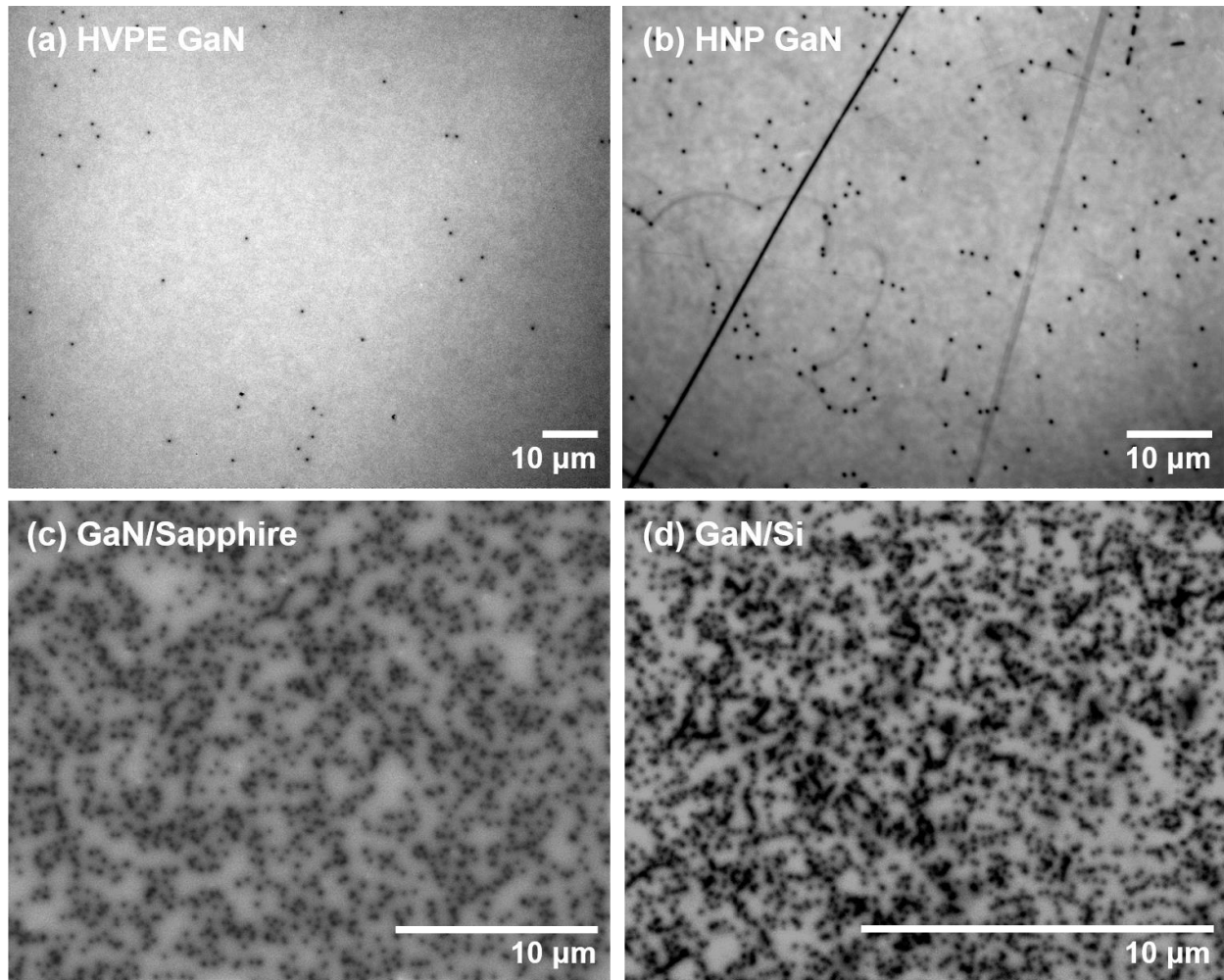


Figure 5.11. CL images of (a) HVPE GaN, (b) HNP GaN, (c) GaN/sapphire, and (d) GaN/Si.

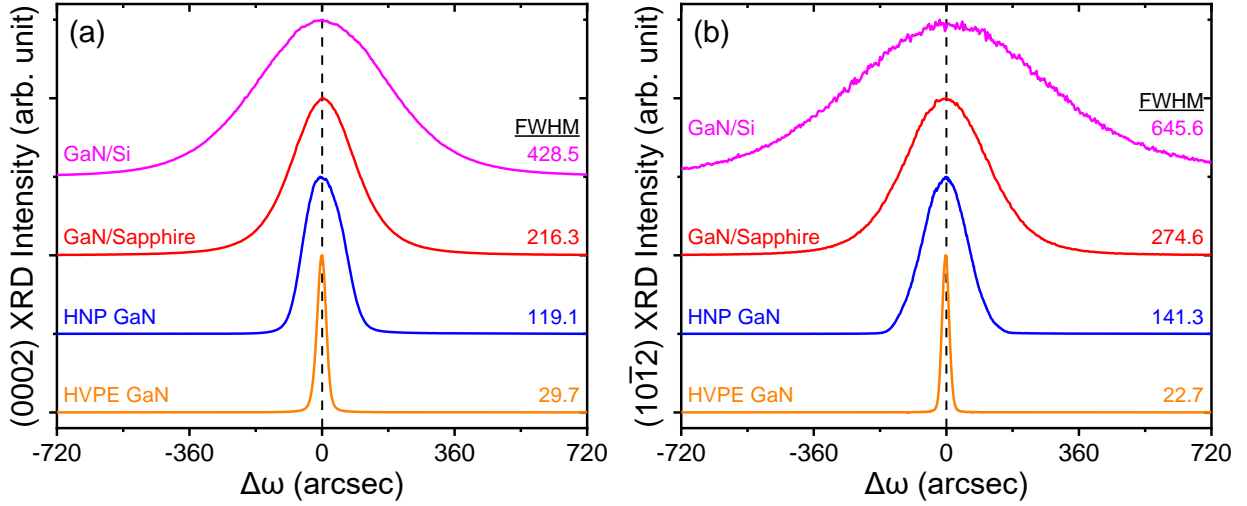


Figure 5.12. Representative XRD ω scans in the (a) (0002) symmetric and (b) (10 $\bar{1}$ 2) asymmetric planes are performed for the HVPE GaN, HNP GaN, GaN/sapphire, and GaN/Si samples (shown in magenta, red, blue, and orange, respectively). FWHM of the ω scans are extracted and used to estimate the dislocation density of each sample. Multiple scans are performed for each sample to obtain an average value.

Table 5.1. Dislocation densities measured by CL and XRD and GaN thermal conductivities κ_{GaN} measured by TDTR of HVPE GaN, HNP GaN, GaN/sapphire, and GaN/Si samples.

Sample	Dislocation Density σ_D ($\times 10^8 \text{ cm}^{-2}$)		κ_{GaN} (W/m-K)
	CL	XRD	
HVPE GaN	0.005	0.018	204.7 ± 4.6
HNP GaN	0.038	0.593	206.6 ± 6.8
GaN/Sapphire	2.433	2.562	191.5 ± 10.5
GaN/Si	10.993	14.671	164.4 ± 3.2

Table 5.2. Impurity concentrations measured by SIMS and impurity scattering strengths Γ calculated by Klemens's model of HVPE GaN, HNP GaN, GaN/sapphire, and GaN/Si samples.

Sample	Impurity Concentration (cm^{-3})				Γ
	Si	H	C	O	
HVPE GaN	9.0×10^{16}	8.3×10^{15}	7.7×10^{16}	7.6×10^{15}	6.82×10^{-7}
HNP GaN	3.0×10^{17}	8.1×10^{15}	8.0×10^{16}	7.4×10^{15}	9.56×10^{-7}
GaN/Sapphire	4.5×10^{15}	2.4×10^{17}	1.3×10^{17}	1.6×10^{16}	3.44×10^{-6}
GaN/Si	1.6×10^{15}	1.6×10^{17}	8.7×10^{18}	1.1×10^{16}	5.81×10^{-5}

A secondary ion mass spectroscopy (SIMS) is performed to estimate the impurity concentrations in the GaN samples. The concentrations of Si, H, C, and O are measured and are then used to quantify the *scattering strength* Γ through Klemens's model

$$\Gamma = \sum_i f_i \left[1 - \frac{M_i}{\bar{M}} \right]^2 \quad (5.18)$$

where f_i is the fractional concentration of the i -th impurity atom, M_i is the atomic mass of the i -th impurity atom, and \bar{M} is the average atomic mass. Both measured impurity concentrations and calculated Γ values are tabulated in Table 5.2. The largest Γ obtained from the GaN/Si sample is still a factor of five times smaller than the scattering due to naturally occurring isotopes suggesting that impurity concentrations of these samples in this work will not limit κ_{GaN} .

Figure 5.13 shows the SIMS measurement results of the (a) HVPE GaN, (b) HNP GaN, (c) GaN/sapphire, and (d) GaN/Si samples. Prior to SIMS analysis, a thin layer of Au is used to coat the sample to prevent any surface charging effect caused by sputtering. The analysis is performed by a CAMECA secondary ion mass spectrometer. The instrument applies a cesium ion beam with 14.5 keV energy to sputter the sample surface, after which the negative secondary atomic ions such as Si, H, C, and O, are captured by the detector. The detection limits of the Si, H, C, and O ions are 1×10^{15} , 7×10^{16} , 5×10^{15} , and $5 \times 10^{15} \text{ cm}^{-3}$, respectively. Except for Si in the (c) GaN/sapphire and (d) GaN/Si samples, the concentrations of impurities are well above the detection limit.

The impurity concentrations listed in Table 5.2 are averaged values. The first (top) 0.3 μm of the profile is excluded in taking the average concentration. Also, for the (c) GaN/sapphire and (d) GaN/Si samples, only depths of up to 2 μm and 2.5 μm , respectively, are considered. With the modulation frequency of 11 MHz used in the TDTR setting, the thermal penetration depth is less

than 2 μm assuming the thermal conductivity of GaN is 200 W/m-K and the volumetric heat capacitance of GaN is 2.64 J/cm³K. Therefore, only impurities within the top 2 μm will influence the thermal transport. SIMS analysis results on similar GaN samples reported in literature can be found in Refs. [109], [111], [133], [134].

The atomic masses of H, C, O, Si, Ga, and N used in the calculation are $M_{\text{H}} = 1.00794$, $M_{\text{C}} = 12.0107$, $M_{\text{O}} = 15.999$, $M_{\text{Si}} = 28.0855$, $M_{\text{Ga}} = 70.9247$, and $M_{\text{N}} = 14.0031$ Da, respectively. The phonon–isotope scattering process is also quantified using a similar approach [133], [135]:

$$\Gamma_{\text{isotope}} = 2 \left[\left(\frac{M_{\text{Ga}}}{M_{\text{Ga}} + M_{\text{N}}} \right)^2 \Gamma(\text{Ga}) + \left(\frac{M_{\text{Ga}}}{M_{\text{Ga}} + M_{\text{N}}} \right)^2 \Gamma(\text{N}) \right] \quad (5.19)$$

where Γ_{isotope} is the isotope *scattering strength* parameter; M_{Ga} and M_{N} are the average atomic mass of Ga and N isotopes, respectively; $\Gamma(\text{Ga})$ and $\Gamma(\text{N})$ are calculated by Eq. (5.18) while only considering isotope atoms of Ga and N (and not impurity atoms), respectively. The naturally occurring isotope compositions of the Ga atom are 60.1 % of ⁶⁹Ga and 39.9% of ⁷¹Ga. For the N atom, the compositions are 99.63% of ¹⁴N and 0.37% of ¹⁵N. The isotope masses are given as $M(^{69}\text{Ga}) = 68.9256$, $M(^{71}\text{Ga}) = 70.9247$, $M(^{14}\text{N}) = 14.0031$, and $M(^{15}\text{N}) = 15.0001$ Da. The GaN samples used in this study are not in any way isotopically enriched, hence, a constant Γ_{isotope} of 2.744×10^{-4} is applied for all samples.

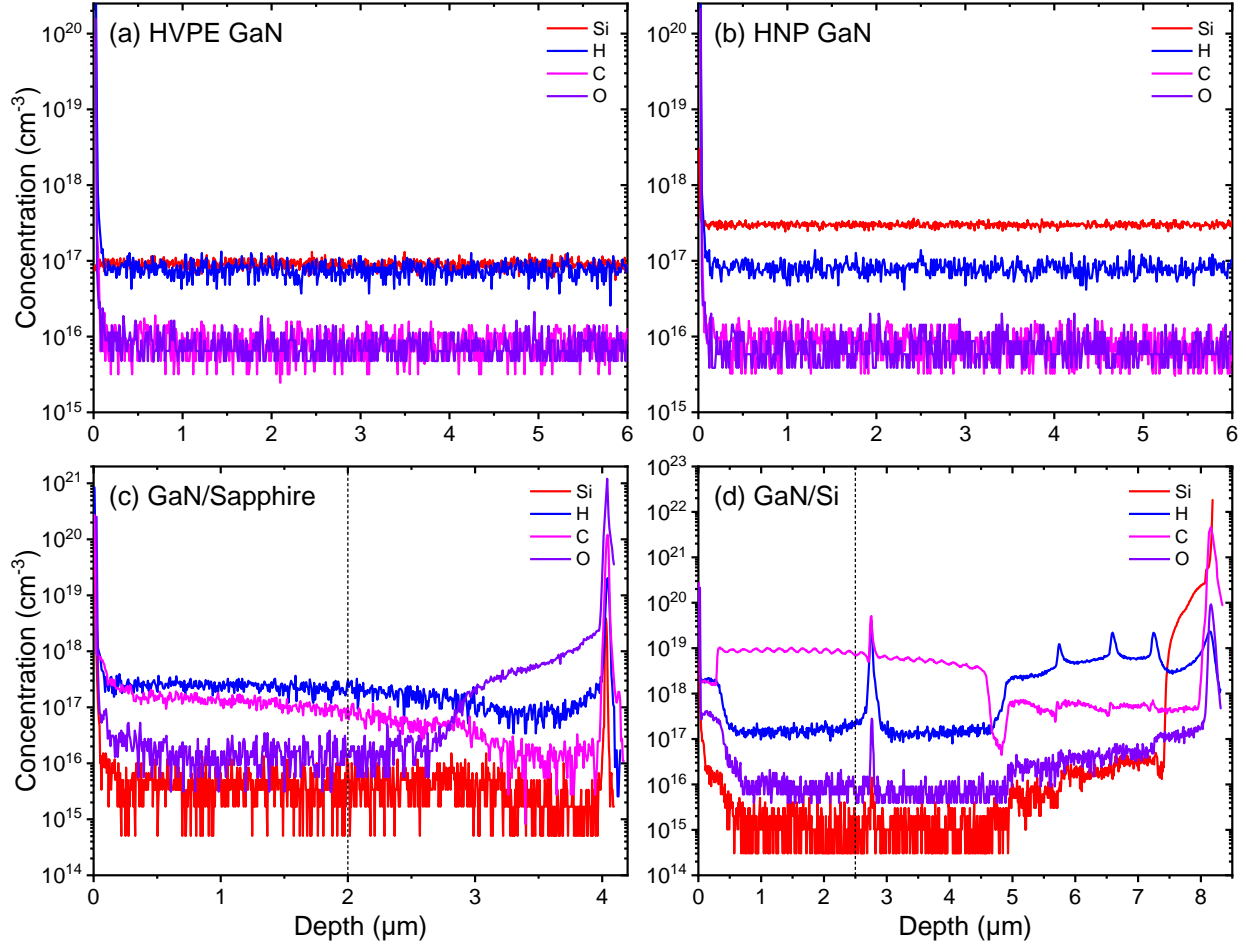


Figure 5.13. SIMS measurement results of the (a) HVPE GaN, (b) HNP GaN, (c) GaN/sapphire, and (d) GaN/Si samples. Average concentration values of impurities Si, H, C, and O are used in the Klemens's model to calculate the scattering strength Γ between phonons and impurities.

5.3.4 Results and Discussion

Figure 5.14 plots experimentally measured κ_{GaN} as a function of experimentally measured σ_{D} (open symbols). An earlier empirical model (plotted as dotted line for reference) by Mion et al. [136], expressed as $\kappa_{\text{GaN}} = 230 \tanh^{0.12}(5 \times 10^6 / \sigma_{\text{D}})$, fails to provide a good fit to this work. A new empirical model, $\kappa_{\text{GaN}} = 210 \tanh^{0.12}(1.5 \times 10^8 / \sigma_{\text{D}})$, is proposed in this work (plotted as dashed line for comparison). The two empirical models have two major differences. The first difference is the maximum κ_{GaN} employed in the empirical formula. In the literature, the highest reported κ_{GaN} values are $294 (\pm 44)$ and $253 (\pm 22)$ W/m-K (measured by the laser flash method) [137], [138],

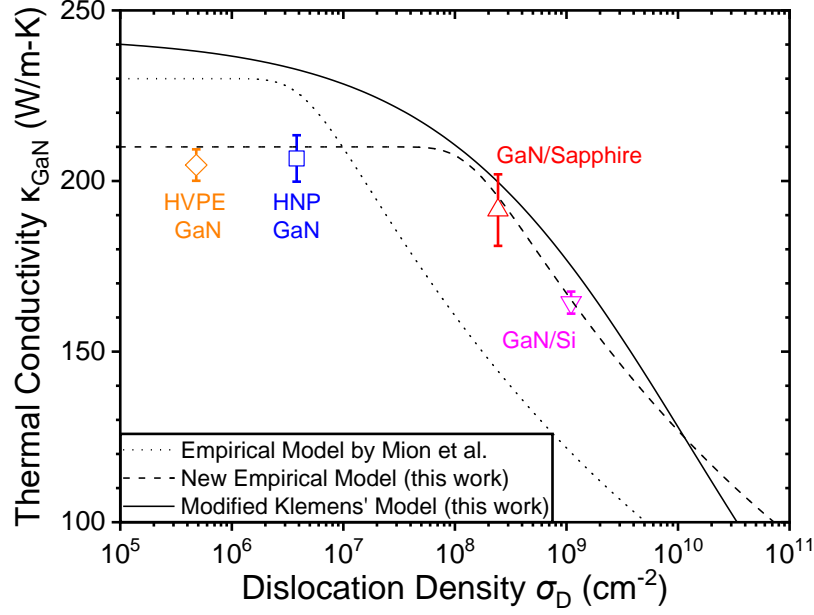


Figure 5.14. GaN thermal conductivity of HVPE GaN, HNP GaN, GaN/sapphire, and GaN/Si plotted as a function of σ_D (open symbols). Empirical model by Mion et al. from Ref. [136], $\kappa_{\text{GaN}} = 230 \tanh^{0.12}(5 \times 10^6 / \sigma_D)$ (dotted line), new empirical model, $\kappa_{\text{GaN}} = 210 \tanh^{0.12}(1.5 \times 10^8 / \sigma_D)$ (dashed line, this work), and modified Klemens's model (solid line, this work) are plotted together for comparison.

and 269 W/m-K (measured by the stationary heat flow method) [108]. Yet most of κ_{GaN} are reportedly < 230 W/m-K [110], [136], [139], [133], [140], [141]. In related work, Zheng et al. [142] recently studied high-quality HVPE and ammonothermal GaN using the TDTR technique and reported κ_{GaN} of ~ 209 W/m-K. These results suggest the discrepancy of measured maximum κ_{GaN} may arise from the differences in the employed experimental technique. The second difference is the deflection point where κ_{GaN} starts to drop as a function of σ_D . In the modified empirical model, σ_D level at which κ_{GaN} starts to drop rapidly is chosen as $1.5 \times 10^8 \text{ cm}^{-2}$ – a slightly larger value than that of Mion et al. [136] (i.e., $5 \times 10^6 \text{ cm}^{-2}$). With this shift, the new empirical model in this work properly captures not only our experimental data on the GaN/sapphire and GaN/Si samples but also other literature that studied GaN samples with high σ_D ($> 10^8 \text{ cm}^{-2}$) [85], [143], [144].

Based on the experimental data, we propose to modify Klemens's model to explain the findings.

Klemens's original model describes the effect of σ_D on κ_{GaN} by the functions [76], [145],

$$\frac{1}{\tau_{\text{DC}}} = \eta \sigma_D \frac{V_0^{4/3}}{v^2} \omega^3 \quad (5.20)$$

$$\frac{1}{\tau_s} = \frac{2^{3/2}}{3^{7/2}} \eta \sigma_D b_s^2 \gamma^2 \omega \quad (5.21)$$

$$\frac{1}{\tau_E} = \frac{2^{3/2}}{3^{7/2}} \eta \sigma_D b_E^2 \gamma^2 \omega \left\{ \frac{1}{2} + \frac{1}{24} \left(\frac{1-2\nu}{1-\nu} \right)^2 \left[1 + \sqrt{2} \left(\frac{v_L}{v_T} \right)^2 \right]^2 \right\} \quad (5.22)$$

where τ_{DC} is the phonon scattering relaxation time associated with dislocation cores, η is the weight factor to account for the mutual orientation of the direction of the temperature gradient and the dislocation line, V_0 is the volume per atom, v is the polarization-averaged phonon velocity, v_L (v_T) is the longitudinal (transverse) sound velocity, ω is the phonon frequency, τ_s (τ_E) is the phonon relaxation time associated with screw-type (edge-type) dislocations, b_s (b_E) is the screw-type (edge-type) dislocation Burgers vector, and γ is the Gruneisen parameter. Previously published literature [111], [136], [133] agrees that the impact of σ_D on κ_{GaN} is underestimated. In order to compensate for the discrepancy, a correction factor of 1000 is commonly used as a multiplier to the scattering rates to fit the experimental results [111], [133].

To fit the experimental data, the Klemens's model is modified accordingly: η is set as 2×10^{10} and σ_D is replaced by $\sigma_D^{0.4}$. The η should be considered as a correction factor rather than a factor that purely represents the effect of the relative orientation between the temperature gradient and the dislocation. These two modifications effectively increase the strength of phonon-dislocation scattering and adjust the rate of κ_{GaN} decrease such that κ_{GaN} is not vanishingly small (> 35 W/m-K) at $\sigma_D > 10^{10} \text{ cm}^{-2}$ [81], [107], [136]. This modified Klemens's model is plotted in Figure 5.14

(solid line). The basic GaN material parameters are taken from Ref. [76]. The same parameter set is used for the calculations of all four GaN samples.

5.3.5 TCAD Simulation of Thermal Resistance of HEMT Devices

To assess the impact of the different GaN thermal conductivities, the heat dissipation in these samples is simulated to extract the thermal resistance of the sample stacks. A three-dimensional structure is built to simulate the maximum temperature of a multi-finger AlGaIn/GaN HEMT [9]. In this model, instead of considering the entire multi-finger HEMT structure, we only work on a single finger with periodic boundary conditions applied in the lateral direction to mimic the center finger [72]. The maximum temperature of the multi-finger HEMT occurs at the center finger cell due to the more difficult lateral heat dissipation compared to the fingers located closer to the edge [146]. Employing a similar approach described in Ref. [57], the hotspot of the HEMT located under the drain side of the gate is simulated. The thickness of each sample and temperature-dependence [73], [142] based on the 300 K thermal conductivity obtained from the TDTR measurements are considered in the simulation. The gate-to-gate spacing, gate width, and length of hotspot are set to $s = 20 \text{ }\mu\text{m}$, $W_G = 250 \text{ }\mu\text{m}$, and $L_H = 1 \text{ }\mu\text{m}$ respectively. The parameters used in the TCAD simulations and their results are tabulated in Table 5.3.

Table 5.3. Thermal resistance of the GaN samples calculated assuming an AlGaIn/GaN multi-finger HEMT structure. Thicknesses and temperature-dependent thermal conductivity values used in TCAD simulation are listed. TBR between GaN and substrate layers are fixed to a moderate $20 \text{ m}^2\text{K/GW}$.

Sample	GaN		Substrate		Thermal Resistance (mm-K/W)
	Thickness (μm)	κ_{GaN} (W/m-K)	Thickness (μm)	κ_{sub} (W/m-K)	
HVPE/HNP GaN	350	$207 (300/T)^{1.4}$	-	-	23
GaN/Sapphire	4.5	$191 (300/T)^{1.4}$	450	$35 (300/T)$	162^a
GaN/Si	5	$164 (300/T)^{1.4}$	1000	$150 (300/T)^{1.3}$	79

^a With a 200- μm -thick sapphire substrate, the thermal resistance is reduced to 83 mm-K/W .

The thermal resistance is obtained by dividing the maximum temperature increase of the device by the dissipated heat (in units of W/mm). The results show that the thermal resistance of the freestanding GaN sample is the lowest. Despite the higher GaN thermal conductivity, the thermal resistance of the GaN/sapphire sample is more than twice that of the GaN/Si sample. This indicates that the device thermal resistance mostly depends on the substrate properties. To reach a thermal resistance comparable to the GaN/Si sample, the GaN/sapphire sample's substrate thickness must be reduced to less than 200 μm ; with a 200- μm -thick sapphire substrate, the thermal resistance is reduced to 83 mm-K/W. Studies have shown improved device performance achieved after substrate thinning [147], [148]. Note that in the simulations, the TBR between GaN and substrate layers is fixed to a moderate 20 $\text{m}^2\text{K/GW}$. In a design where the GaN layer thickness is too thin (typically less than 1 μm) to allow sufficient thermal spreading, the thermal resistance of the device may strongly depend on the TBR [57]. However, with the GaN layer thicknesses of my samples the TBR did not have much impact on the results.

5.4 Conclusion

In conclusion, four types of GaN samples (HVPE GaN, HNP GaN, GaN/sapphire, and GaN/Si) are studied using CL, XRD, and TDTR to determine σ_D and κ_{GaN} . GaN thermal conductivities of HVPE GaN, HNP GaN, GaN/sapphire, and GaN/Si are measured as 204.7 (± 4.6), 206.6 (± 6.8), 191.5 (± 10.5), 164.4 (± 3.2) W/m-K, respectively. The determining factor of κ_{GaN} is shown to be σ_D when $\sigma_D > 1.5 \times 10^8 \text{ cm}^{-2}$. The new empirical model $\kappa_{\text{GaN}} = 210 \tanh^{0.12}(1.5 \times 10^8 / \sigma_D)$ describes the relationship between κ_{GaN} and σ_D . A modified Klemens's model is proposed to increase the strength of phonon–dislocation scattering and adjust the rate of κ_{GaN} decrease such that it explains the experimental results. The thermal resistances of the GaN samples are also calculated using TCAD simulation. The GaN/sapphire sample, while having a larger thermal conductivity than the

GaN/Si sample, is shown to have the largest thermal resistance among the three samples. Overall, We report how κ_{GaN} of heteroepitaxial GaN can be estimated based on σ_{D} . This work lays the foundation for thermal management of the technologically important GaN-based semiconductor devices, typically grown on foreign substrates with high σ_{D} .

CHAPTER 6 SUMMARY AND CONCLUSION

First, we introduced the uniaxial dielectric continuum model with temperature-dependent phonon mode frequencies to study temperature- and orientation-dependent polar optical phonon limited electron mobility and saturation velocity in uniaxial semiconductors. The formalisms for calculating electron scattering rates, momentum relaxation rates, and rate of energy change as a function of the electron kinetic energy and incident electron angle with respect to the c -axis are presented and evaluated numerically. Electron–longitudinal optical phonon interactions are shown to depend weakly on the electron incident angle whereas the electron–transverse optical phonon interactions around the emission threshold energy are observed to depend most strongly on the electron incident angle when varied from $\pi/4$ to $\pi/2$ (with respect to the c -axis). The electron mobility and saturation velocity limits in different GaN crystal orientations as a function of temperature and electron concentration are provided. At room temperature and for an electron density of $5 \times 10^{18} \text{ cm}^{-3}$, electron mobility limit of $\sim 3200 \text{ cm}^2/\text{V-s}$ and electron saturation velocity limit of $3.15 \times 10^7 \text{ cm/s}$ are calculated. Both GaN electron mobility and saturation velocity are observed to be governed by the longitudinal optical phonon interaction, and their directional anisotropy is shown to vary less than 5% as the electron incident angle with respect to the c -axis is varied from 0 to $\pi/2$.

Presented next is a detailed theoretical analysis of the interaction between electrons and optical phonons of interface and confined modes in a wurtzite AlN/GaN/AlN quantum well heterostructure based on the uniaxial dielectric continuum model. The formalism describing the interface and confined mode optical phonon dispersion relation, electron–phonon scattering rates, and average group velocity of emitted optical phonons are developed and numerically calculated.

The dispersion relation of the interface phonons shows a convergence to the resonant phonon frequencies 577.8 and 832.3 cm^{-1} with a steep slope around the zone center indicating a large group velocity. At the onset of interface phonon emission, the average group velocity is small due to the large contribution of interface and confined mode phonons with close-to-zero group velocity, but eventually increases up to larger values than the bulk GaN acoustic phonon velocity along the wurtzite crystal *c*-axis (8 nm/ps). By adjusting the GaN thickness in the double heterostructure, the average group velocity can be engineered to become larger than the velocity of acoustic phonons at a specific electron energy. This suggests that the high group velocity interface mode optical phonons can be exploited to remove heat more effectively and reduce junction temperatures in GaN-based heterostructures.

Extending the discussion to a more macroscopic level, the effects of thermal boundary resistance and temperature-dependent thermal conductivity on the thermal resistance of GaN/ substrate stacks were also investigated. Combinations of parameters such as substrates (diamond, silicon carbide, silicon, and sapphire), thermal boundary resistance (10 to 60 $\text{m}^2\text{K/GW}$), heat source lengths (10 nm to 20 μm), and power dissipation levels (1 to 8W) are studied by using technology computer-aided design software Synopsys. Among diamond, silicon carbide, silicon, and sapphire substrates, diamond provides the lowest thermal resistance due to its superior thermal conductivity. We report that due to non-zero thermal boundary resistance and localized heating in GaN-based high-electron-mobility transistors, an optimal separation between heat source and substrate exists. For high-power heat dissipation on highly thermally conductive substrates such as diamond, the optimal separation between heat source and substrate becomes submicron thick (i.e. 500 nm), which reduces the hotspot temperature by as much as 50 $^{\circ}\text{C}$ compared to conventional multi-micron thick case (i.e. 4 μm). This is attributed to the thermal conductivity drop in GaN near the

heat source. Improving the TBR between GaN and diamond further increases temperature reduction by our approach. Thermal management design guidelines for GaN-based devices were provided in Chapter 4.

Lastly, GaN thermal conductivity of hydride vapor phase epitaxy grown GaN (HVPE GaN), high nitride pressure grown GaN (HNP GaN), and metal-organic chemical vapor deposition grown GaN on sapphire (GaN/sapphire), and on Si (111) (GaN/Si) are measured as 204.7 (± 4.6), 206.6 (± 6.8), 191.5 (± 10.5), 164.4 (± 3.2) W/m-K, respectively, using time-domain thermoreflectance technique. Dislocation densities of HVPE GaN, HNP GaN, GaN/sapphire and GaN/Si are measured as $4.80 (\pm 0.42) \times 10^5$, $3.81 (\pm 0.08) \times 10^6$, $2.43 (\pm 0.20) \times 10^8$, and $1.10 (\pm 0.10) \times 10^9$ cm⁻², respectively, using cathodoluminescence and X-ray diffraction studies. Impurity concentrations of Si, H, C, and O are measured by secondary ion mass spectroscopy studies. The relationship between GaN thermal conductivity and dislocation density is modeled through a new empirical model $\kappa_{\text{GaN}} = 210 \tanh^{0.12}(1.5 \times 10^8 / \sigma_D)$. A modified Klemens's model, where dislocation-induced scattering strength is increased, is proposed to explain the experimental rate of decrease in κ_{GaN} with increasing σ_D . Overall, Chapter 5 reports how GaN thermal conductivity of heteroepitaxially grown GaN can be estimated based on dislocation density, providing key design guidelines for thermal management in GaN semiconductor devices.

APPENDIX A P-CHANNEL CUBIC-PHASE GaN HETEROSTRUCTURE FIELD-EFFECT TRANSISTORS

A.1 Introduction

Recent advances in GaN technology have enabled GaN-based devices to replace their silicon-based counterparts in the field of high-power and high-frequency electronics applications. One of the major advantages of the material is the inherent polarization fields in the thermodynamically stable hexagonal-phase (h-) AlGaIn/GaN heterostructures which induce a two-dimensional electron gas (2DEG). As the 2DEG eliminates the need for any intentional doping, electrons do not suffer from impurity scattering and can traverse in the gas with high mobility. The drawbacks of such polarization fields are that (1) GaN-based HEMTs (high-electron-mobility transistors) operate in depletion mode and (2) p-channel devices cannot be built on the same epitaxial structure. To take full advantage of the superior material properties of GaN, we propose a p-channel device built on cubic-phase (c-) AlGaIn/GaN [149], [150].

A.2 Device Structure and Simulation Method

TCAD Synopsys Sentaurus is used to simulate characteristics of the cubic-phase AlGaIn/GaN HFET. The schematic diagram of the device structure is shown in Figure A.1. The device structure is basically a three-layer system: a SiO₂ layer on top of epitaxially grown c-AlGaIn on a c-GaN layer. The c-AlGaIn layer has a delta-doped (δ -doped) layer of thickness t_2 which is sandwiched by two intrinsic c-AlGaIn layers of thicknesses t_1 and t_3 . The thickness of the topmost AlGaIn layer is t_3 . The c-GaN layer where the two-dimensional hole gas (2DHG) channel is formed is also intrinsic. The gate metal contact forms a MOS (metal-oxide-semiconductor) system with the oxide

and AlGaN layer, whereas the source and drain contacts form ohmic contacts with the p-type doped GaN.

The material parameters used in the simulation are listed in Table A.1 [56], [151], [152], [153], [154], [155]. For comparison, the h-AlN and h-GaN material properties are included as well. The band gap of the AlN and GaN can be calculated by the Varshni model

$$E_G(T = 300) = E_0 - \frac{\alpha T^2}{\beta + T} \quad (\text{A.1})$$

where E_0 is the band gap at 0 K, T is temperature, α is the Varshni coefficient, and β is the Debye temperature. Material parameters of $\text{Al}_x\text{Ga}_{1-x}\text{N}$ with aluminum (Al) content of x are determined by a linear interpolation (bowing parameters are neglected for simplicity) between the values of the respective parameters of the *pure* AlN and GaN.

In the simulations, except for the varied design parameter, other parameters are set to their default values unless otherwise specified: $t_1 = 3$ nm, $t_2 = 2$ nm, $t_3 = 15$ nm, $t_{\text{ox}} = 5$ nm, δ -doping $= 2 \times 10^{19} \text{ cm}^{-3}$, aluminum content $x_{\text{Al}} = 0.4$, work function $\Phi_{\text{M}} = 4.5$ V. Standard physical treatments and techniques are employed; drift-diffusion transport, Poisson equation, continuity equation, and

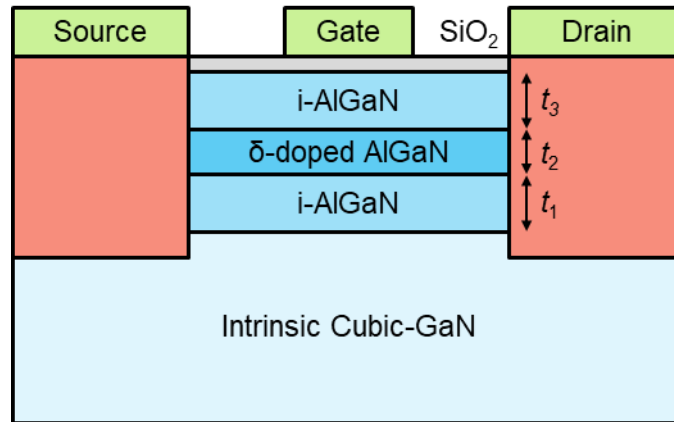


Figure A.1. Schematic of simulated device. Thicknesses of the AlGaN layers are t_1 , t_2 , and t_3 , with t_3 being the thickness of the topmost AlGaN layer.

Table A.1. Material parameters for cubic- and hexagonal-phase GaN and AlN. Mobilities in the parentheses are values for carriers in the two-dimensional electron or hole gas channel. The cubic material parameters are used in the p-channel device simulations.

Parameter	Symbol	Cubic	Hexagonal		
		c-AlN	c-GaN	h-AlN	h-GaN
Band gap at 0 K	E_0 (eV)	6.00	3.299	6.25	3.510
Varshni coefficient	α (eV/K)	5.93×10^{-4}	5.93×10^{-4}	1.799×10^{-3}	9.09×10^{-4}
Debye temperature	β (K)	6.00×10^2	6.00×10^2	1.462×10^3	8.30×10^2
Electron affinity	χ (V)	1.999	3.922	1.01	3.18
Relative permittivity	ε	9.14	9.7	8.5	8.9
Electron mobility	μ_e (cm ² /V-s)	300	1000 (1000)	300	1000 (1500)
Hole mobility	μ_h (cm ² /V-s)	20	150 (250)	14	200

Fermi statistics are applied to both electrons and holes. In addition, thermionic hole emission is also considered for any hole transport across heterojunctions. The interface conditions are as follows:

$$J_{p,2} = -2q \left[v_{p,2} p_2 - \frac{m_{p,2}}{m_{p,1}} v_{p,1} p_1 \exp \left(\frac{\Delta E_V}{kT_{p,1}} \right) \right] \quad (\text{A.2})$$

$$v_{p,i} = \sqrt{kT_{p,i} / 2\pi m_{p,i}}. \quad (\text{A.3})$$

$J_{p,1}$ and $J_{p,2}$ are the hole current density leaving material 1 and 2 ($J_{p,1} = J_{p,2}$), respectively, and $v_{p,i}$ is the emission velocity.

A.3 Results and Discussion

Figure A.2 shows the band diagram along the vertical direction of the center of the device at equilibrium with different Al contents. The first AlGaN layer on top of the GaN layer helps the triangular well confine holes and prevents them from escaping the channel. Therefore, increasing the Al content of the AlGaN layer increases the hole density in the channel as shown in Figure

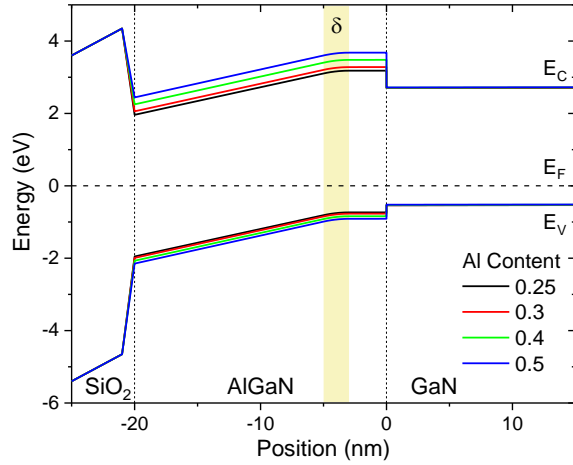


Figure A.2. Energy band diagram of the device under equilibrium condition with different aluminum contents.

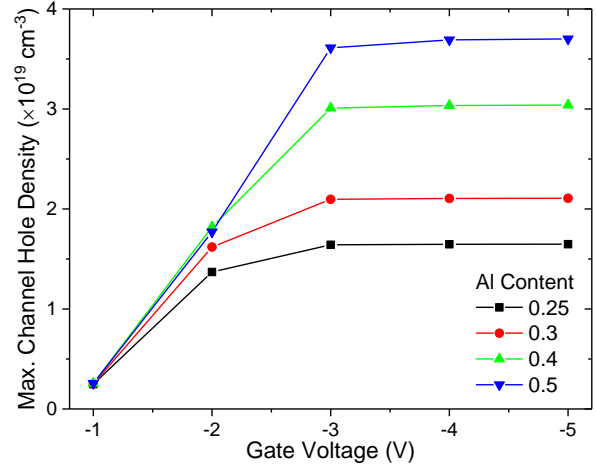


Figure A.3. Comparison of maximum channel hole density with varying aluminum content. Hole density increases with aluminum content.

A.3. For n-type devices where electrons are confined at the triangular well of the conduction band, Al composition of ~20% is desirable since it provides sufficient electron confinement without inducing too much lattice mismatch. However, for p-type devices, due to the smaller valence band offset, a number larger than 0.2 is necessary. The Al content is set to 0.4 to secure a valence band offset of 0.3 eV which is comparable to the conduction band offset of n-channel device with 20 % Al composition.

Figure A.4 shows the effect of Al content on transfer characteristics of the p-channel device. The curves intersect at gate voltage of about -4 V. As the gate voltage exceeds -4 V, a triangular well starts to form at the $\text{SiO}_2/\text{AlGaN}$ interface. Due to the serial capacitance effect, further increasing the gate voltage (in the negative direction) only contributes to the hole density increase at the $\text{SiO}_2/\text{AlGaN}$ interface. Once this channel is created, current starts to flow through this secondary channel.

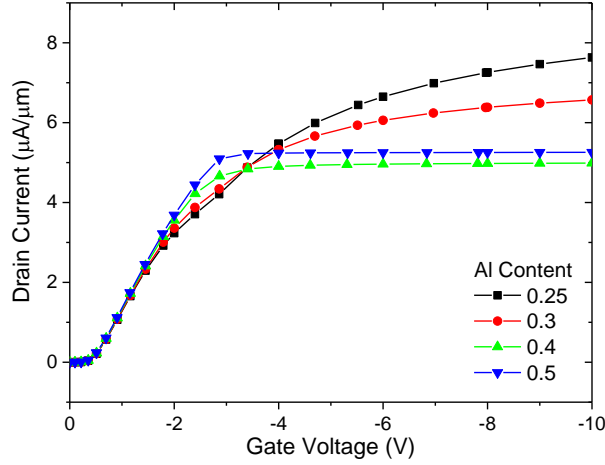


Figure A.4. Drain current at low drain bias (50 mV) with different aluminum contents. Irregular characteristics are due to hole pile-up at the $\text{SiO}_2/\text{AlGaN}$ interface.

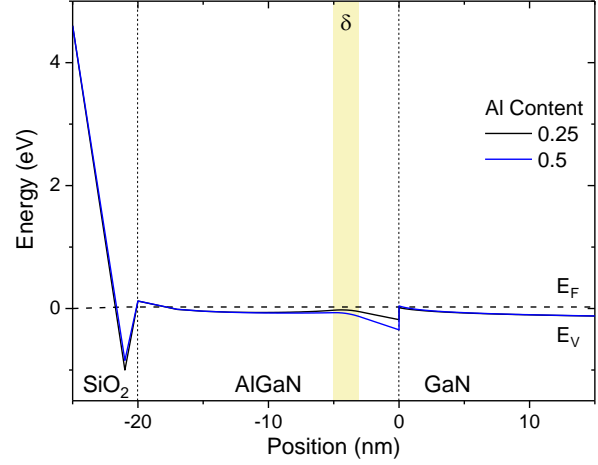


Figure A.5. Valence band diagram at gate voltage of -10 V showing formation of the secondary hole channel at the $\text{SiO}_2/\text{AlGaN}$ interface for aluminum content of 0.25 and 0.5.

As shown in Figure A.5, the larger valence band offset secured by increasing the Al composition does not prevent the formation of the secondary channel. However, the increased composition significantly impacts the hole mobility of the $\text{Al}_x\text{Ga}_{1-x}\text{N}$ layer which results in a negligible current through the channel.

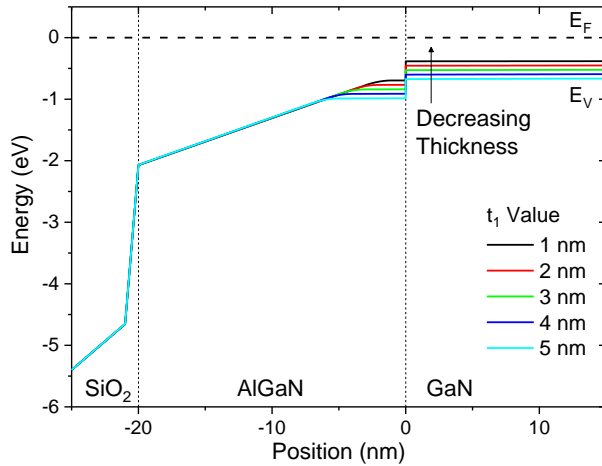


Figure A.6. Band diagram with different AlGaN layer thickness t_1 at equilibrium. *Thinning* the layer increases hole density in the channel.

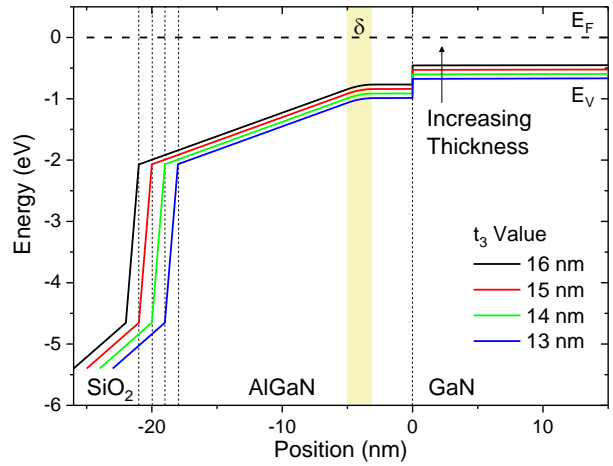


Figure A.7. Band diagram with different AlGaN layer thickness t_3 at equilibrium. *Thickening* the layer increases hole density in the channel.

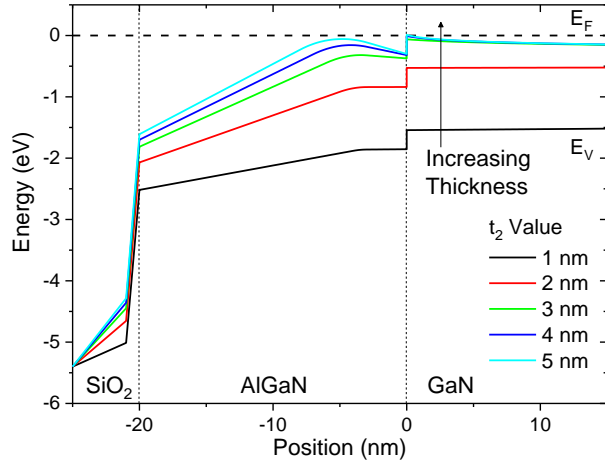


Figure A.8. Band diagram with different AlGaN layer thickness t_2 at equilibrium. Thickening the layer increases the hole density in the channel.

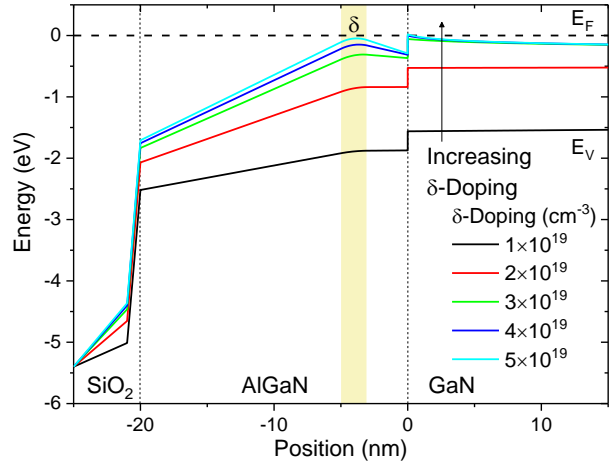


Figure A.9. Band diagram with different δ -doping concentrations at equilibrium. Hole density in the channel increases with doping level.

Figure A.6 and Figure A.7 show the valence band energy at equilibrium with different AlGaN layer thicknesses t_1 and t_3 , respectively. While varying thickness t_1 , the thickness of the whole AlGaN layer stack is fixed to 20 nm by thinning t_3 , so that $t_1 + t_3 = 18$ nm and $t_2 = 2$ nm. In the case of Figure A.7, the thickness of the stack is not kept constant. Compared to other design parameters, these two have less impact on the normally-OFF operation and transfer characteristics. For real devices, however, the first AlGaN layer serves as a layer that separates the channel and δ -doped AlGaN layer. If t_1 is too thin, mobility of holes in the channel is affected by the Coulomb potential induced by the ionized impurities in the δ -doped AlGaN layer.

As the δ -doped AlGaN layer primarily provides holes to the 2DHG, thickness and doping level of this layer are key parameters that have a large impact on the normally-OFF behavior. Figure A.8 shows the band diagram with different AlGaN layer thickness t_2 . Figure A.9 shows the band diagram with different δ -doping concentrations. Thickening t_2 and increasing the δ -doping level essentially increases the net number of holes that may be supplied to the channel and therefore pushes the valence band edge closer to the Fermi level. The valence band edge level exceeding the Fermi level is considered as an indicator of the 2DHG channel being formed even at zero gate

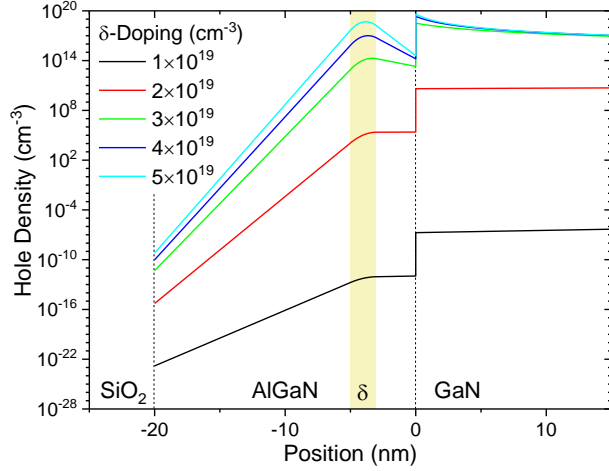


Figure A.10. Hole density distribution with different δ -doping concentrations. Doping level of $3 \times 10^{19} \text{ cm}^{-3}$ shows normally-ON behavior.

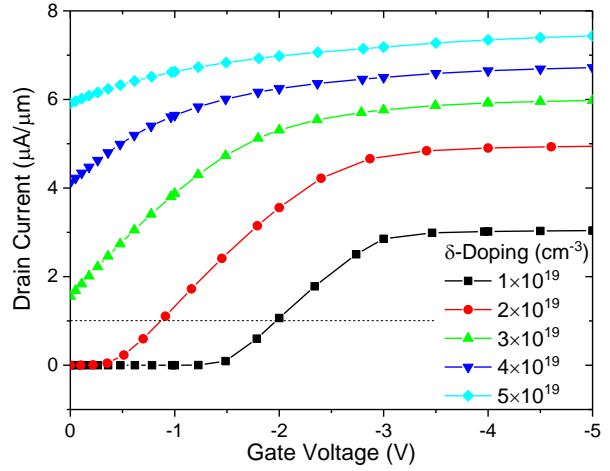


Figure A.11. Transfer characteristics with different δ -doping levels. Threshold voltage is controlled effectively by adjusting δ -doping levels.

voltage (see Figure A.10). Hence, to prevent it being normally-ON and allow sufficient room for threshold voltage adjustment, t_2 is set to 2 nm and the δ -doping level is set to $2 \times 10^{19} \text{ cm}^{-3}$.

Figure A.11 shows transfer characteristics with different δ -doping levels. Doping levels of $\geq 3 \times 10^{19} \text{ cm}^{-3}$ show the 2DHG channel is already formed at zero gate voltage resulting in a normally-ON device. Curves with $\leq 2 \times 10^{19} \text{ cm}^{-3}$ show that the threshold voltage can be effectively controlled by adjusting the doping level. Similar behavior is observed when the t_2 thickness is varied; thickening t_2 has the same effect of increasing doping level. These two parameters can be controlled complementarily to target the desired threshold voltage.

Although the gate metal selection is mostly limited by fabrication issues, it is worth noting that for p-channel devices, metals with a lower work function such as Ti and W may be desirable. Band diagram with various gate metals is shown in Figure A.12.

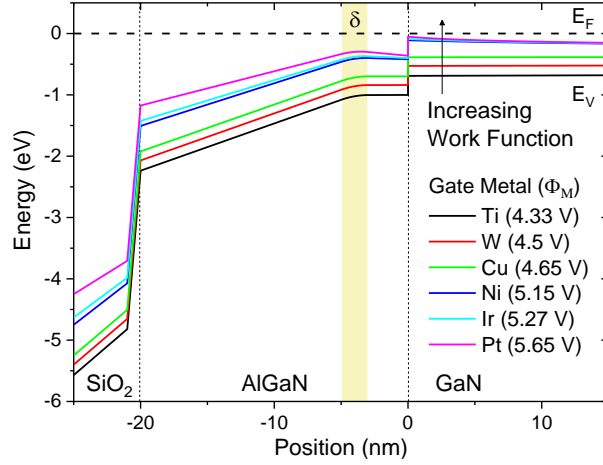


Figure A.12. Band diagram with various gate metals.

Figure A.13 shows transfer characteristics with different SiO₂ thicknesses at (a) low (50 mV) and (b) high drain bias (5 V). Setting the threshold voltage to be the voltage where current exceeds 1 $\mu\text{A}/\mu\text{m}$, we observe that $|V_{\text{th}}|$ shifts to a lower value as the drain voltage increases which indicates a DIBL-type effect is occurring. In this device, the gate-source and gate-drain separation is set to 0.25 μm and the gate length is set to 1 μm . To minimize the DIBL effect under stronger drain biases, a device longer in the lateral direction may be designed. Here, the primary focus is to study the effect of epilayer thicknesses and not consider optimizing lateral dimensions. As shown in Figure A.12, increasing the oxide thickness and increasing AlGaIn layer thickness t_3 have similar

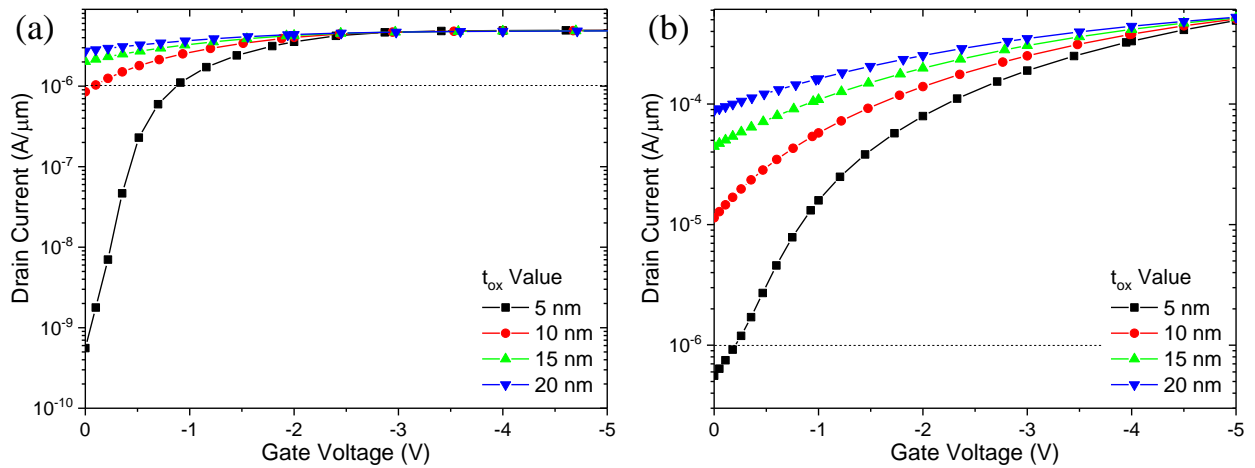


Figure A.13. Transfer characteristics with different SiO₂ thicknesses at (a) $V_D = 50$ mV and (b) 5 V.

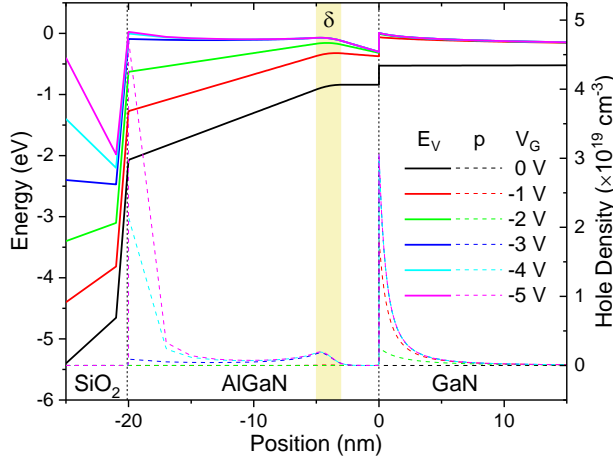


Figure A.14. Band diagram and hole density distribution at different gate voltages using default parameters.

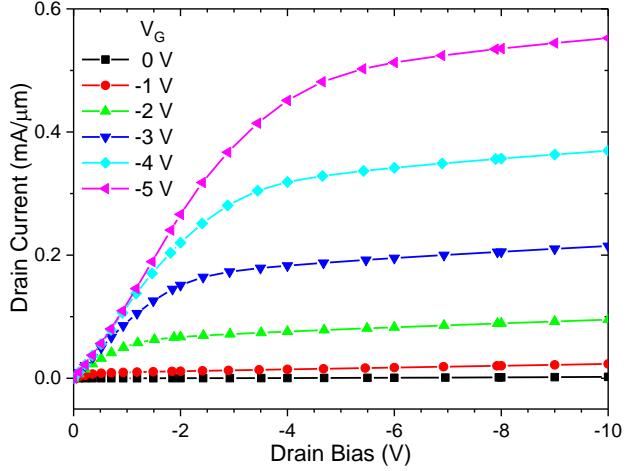


Figure A.15. I_D - V_D characteristics at different gate voltages using default parameters.

effects on the valence band alignment. Thinning the oxide as much as possible is beneficial as it increases the ON-current to OFF-current ratio and increases $|V_{th}|$ as well.

Figure A.14 shows the band diagram and hole density distribution at different gate voltages using the default design parameters. As mentioned above, increasing $|V_G|$ more than -4 V supplies holes to the $\text{SiO}_2/\text{AlGaIn}$ interface. Although the channel does not contribute much to the total current due to its low mobility, the gate voltage should be limited to > -4 V to assure there is no quantum mechanical tunneling through the oxide layer.

Figure A.15 shows the I-V characteristics of the device with default design parameters. A normally-OFF behavior with considerably high drain current (~ 0.4 mA/ μm) is achieved at the safe $V_G = -3$ V bias point.

A.4 Conclusion

P-channel cubic-phase GaN HFET is investigated via TCAD simulation. Effects of design parameters on transfer characteristics of the device are shown. Thickness and doping concentration

of the δ -doped AlGaN layer are shown to have the largest impact on the device performance. A normally-OFF device ($V_{th} < -1$ V) with drain current of 0.4 mA/ μ m is demonstrated.

APPENDIX B LOW-TEMPERATURE PHOTOLUMINESCENCE

For measurement of room-temperature internal quantum efficiency (IQE) in light emitting diodes (LEDs), low-temperature photoluminescence is typically used. By comparing the light intensity of LEDs at 300 K and 1.4 K, assuming that all non-radiative recombination centers are deactivated at 1.4 K, the room-temperature IQE can be extracted. Provided here is the operation manual of the helium bath cryostat and the photoluminescence setup located in the Materials Research Laboratory (MRL) of the University of Illinois at Urbana-Champaign.

The photoluminescence setup and a schematic of the equipment and laser path are shown in Figure B.1. A laser with wavelength of 266 nm is used to investigate the LEDs. The maximum laser power available at the sample end is 3.6 W due to the 45° reflector. By adjusting the polarizer, the laser power may be controlled. Generally, the acquired fluorescent signal intensity of the LEDs depends on four factors: focus of the laser beam, power of the laser beam, the slit opening of the spectrometer, and the integration time used in the CCD camera. The focus of the laser beam and integration time need to be fixed prior to the actual measurements. For analysis purposes, it is

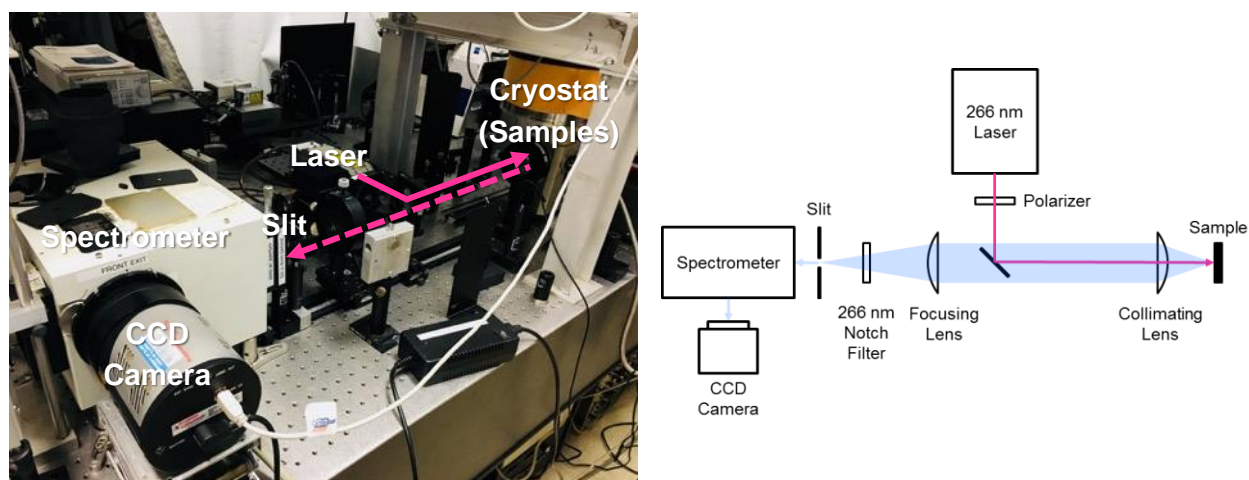


Figure B.1. Photograph of photoluminescence setup at MRL used to investigate LEDs and schematic diagram of the optics, equipment, sample, and laser beam path.

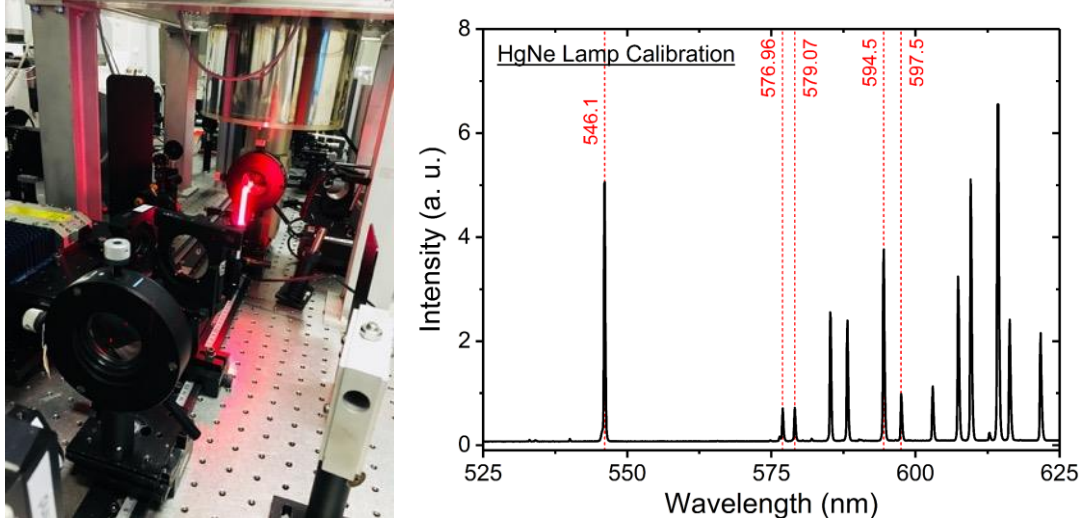


Figure B.2. Photograph of the wavelength calibration step using mercury-neon lamp and spectrometer readings of the lamp after calibration. The red dotted vertical lines show a few emission wavelengths that coincide with mercury-neon emission lines.

better to have larger signal intensity assuming it does not saturate the CCD camera. Also, the slit opening should not be too wide to worsen the spectral resolution considerably.

Before conducting any actual photoluminescence measurements, wavelength calibration of CCD camera using a mercury-neon lamp was done. For the measurements of blue LEDs, the spectrometer's gratings were set to have a center wavelength of 440 nm. For the green LED, it was set to 575 nm. Figure B.2 shows the experimental calibration procedure and the result data obtained from the lamp after calibration. Table B.1 shows the available gratings of the spectrometer. The grating can be selected from the software. The spectral resolution and the wavelength range vary depending on the grating selected. For GaN, grating 1 may be used.

Table B.1. List of grating and wavelength of the spectrometer.

Grating No.	Grooves	$\Delta\lambda/\text{slit}$ (nm/mm)	Blaze (nm)	Range
1	600	5.6	500	330 – 750 nm
2	150	22	500	330 – 750 nm
3	600	5.6	1200	1 μm – 2.1 μm

B.1 Optics

1. Install the CCD camera to the spectrometer.
 - a. The camera should be on the other side (right-hand side) of the PL setup (right to the cryostat).
 - b. Turn off power, disconnect power and communication cable from the back of the camera.
 - c. Unscrew screw that fixes the camera to the spectrometer. The 3/32 wrench should be used. Don't have to unscrew completely; just enough to remove the camera is fine.
 - d. The spectrometer on the left side should have a metal plate cover on the 'front exit' of the spectrometer. Unscrew the bolts so that the hole is exposed.
 - e. Place the camera in the hole (try to place it as level as possible), fix it with screws and connect back the cables. Figure B.3 shows camera installed into the spectrometer.
 - f. If the distance between the spectrometer and the camera is not adjusted to focal length, this has to be done later on.
2. Find the laser with the appropriate wavelength. For GaN, 266 nm laser may be used.
 - a. The laser may be in use at the time-resolved PL (TRPL) setup, so check if someone is using TRPL beforehand. It may also be in use on the other side (right-hand side) of the PL setup (right to the cryostat).
 - b. The laser must be in the proper position. For room-temperature measurements, installing the laser with an angle not perpendicular to the rail and laser path is fine. For low-temperature measurements, the laser may be installed perpendicular to the rail so that either the sample is held at 45° and bounces back the PL emission to the spectrometer or the incident laser path coincides with the emission path.

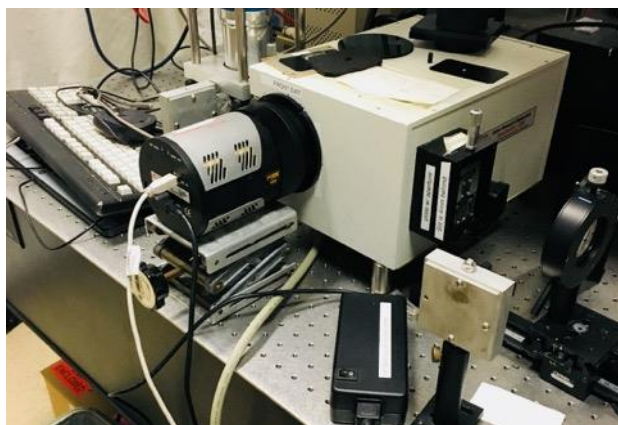


Figure B.3. Camera installed into the spectrometer.



Figure B.4. Power module for the 266 nm laser.

3. The two larger lenses are used to focus on the sample or the slit on the spectrometer. They will reform the laser into a parallel beam between them so that the distance between the two of these does not affect the focus on the slit and the sample.
4. First a paper card may be placed on the sample holder to see if the fluorescent light is focused on the slit.
5. Figure B.4 shows the power module of the laser. Turn on laser.
 - a. Turn key. Lights on the box will start to blink. Wait till the blink stops.
 - b. Press red button next to the key to turn on laser.
 - c. Put the appropriate wavelength goggles on. Wear thin nitrile gloves to protect hand from laser.
 - d. A sliding laser blocker (closed) is in front of the laser aperture. Open with the laser pointing approximately to the sample on the holder and necessary beam blocks to block stray beam.
6. Focus collimated beam onto slit on the spectrometer.
 - a. Using the paper card, focus light on the slit. This can be more easily done if the card used has letters on it (with ring illuminator). Try to make the letters on the slit illegible by adjusting the distance between the slit and the lens closer to it.

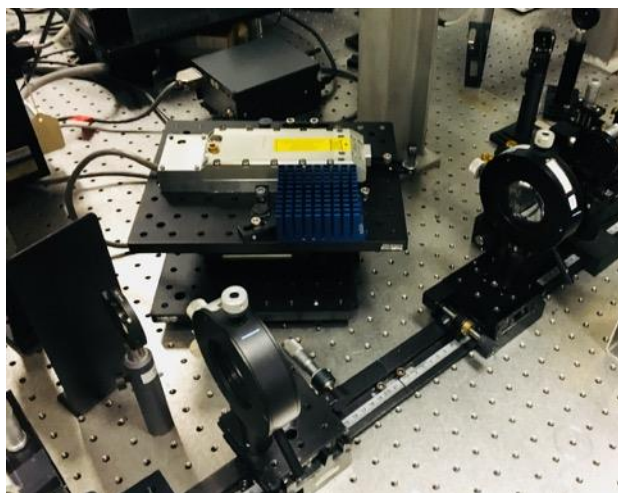


Figure B.5. Laser focused on the sample, and lenses collimating and focusing photoluminescence light on slit of spectrometer is shown.



Figure B.6. 266 nm wavelength notch is installed right before the slit to filter out stray laser source light arriving at spectrometer.

- b. Once the focal distance is found, fix the lens to the rail.
7. Place sample on to the holder.
8. Focus laser beam on the sample by adjusting the distance between sample and the lens closer to it. At this point, trying to make the fluorescent spot as small as possible will suffice. Figure B.5 shows position of spectrometer, laser module, collimating lens, and focusing lens, while laser is focused on the sample.
 - a. The fluorescent light should be collected and focused on the slit. By adjusting the height of the optics and sample, position the beam spot at the center between the slits, horizontally, but slightly above the middle, vertically (between the two screws).
9. Once the focal distance between the lens–slit and lens–sample is found, changing the distance between the lenses, theoretically, should not affect the experiment.
10. *Note on the laser configuration:* For room-temperature PL measurement that does not involve the use of cryostat, following the above steps is fine. However, when using the cryostat, the samples are loaded inside a chamber which can only be accessed through limited angles due

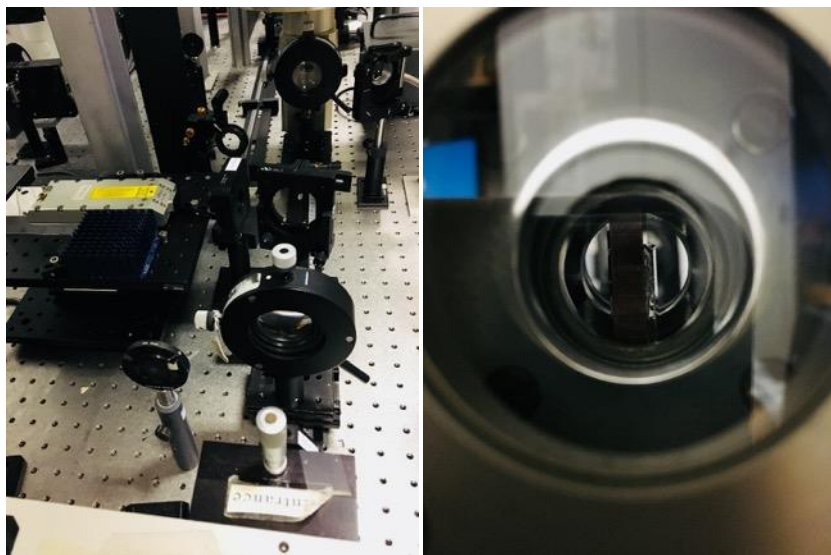


Figure B.7. (Left) Optics aligned beam path where 45° angle mirror was used. (Right) Sample inside cryostat sample chamber.

to the narrow windows. For this reason, the laser cannot be pointed at the sample with an angle that is not 90°.

To solve the issue, a small 45° angle mirror has been installed (between the two lenses) so that the incident beam arrives at the sample perpendicularly. The photoluminescent light is collected by the spectrometer. As shown in Figure B.6, a 266 nm wavelength notch is placed before the slit so that laser bouncing off unexpected surfaces does not get collected. Figure B.7 shows configuration of optics in which sample is loaded inside cryostat and 45° angle mirror is used to redirect laser beam.

B.2 Cryostat

1. One day before the actual measurement, the jacket must be vacuum pumped down to 10^{-6} mbar (1 mbar = 0.75 Torr).
 - a. Connect vacuum pump to the pipe in front of the cryostat chamber as in Figure B.8.
 - b. Connect exhaust to the pipe on the ceiling as in Figure B.9.

- c. There are two power cables, one for the turbo and roughing pumps and one for the vent.
When evacuating the jacket, the power to the vent should be off. Connect power to wall outlet or power strip without any parallel connection, if possible.
- d. *The roughing pump pumps down the pressure to 10^{-2} mbar and the turbo pump can be operated in pressures below that.*
- e. Open the valve on the pump side and power on the roughing pump. The roughing pump's power is at the backside of the panel, with a plastic cover on it.
- f. Make sure that everything before the jacket valve is evacuated below 10^{-2} mbar before switching to the turbo pump. Once the turbo pump is on, the jacket valve can be slowly opened.
- g. Depending on when the cryostat was last used, the pressure in the jacket may or may not be low enough to use the turbo pump only to evacuate (check the pressure meter on the hanging shelf). If the pressure reading is constantly going above 10^{-2} mbar when slowly opening the jacket valve, because the cryostat was not used for a long time, turn

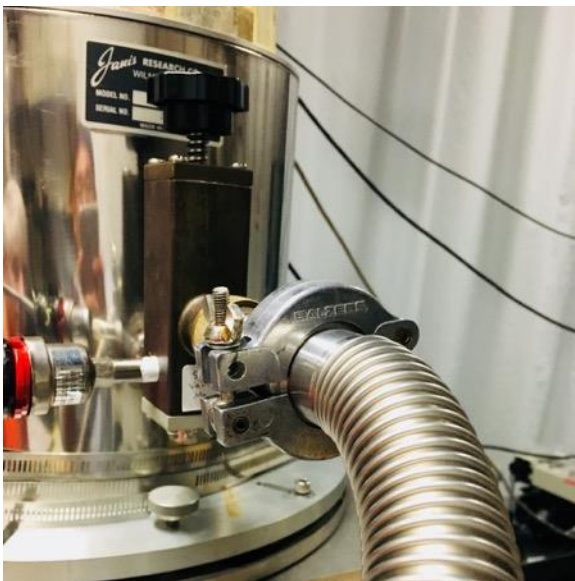


Figure B.8. Vacuum pump connected to cryostat.

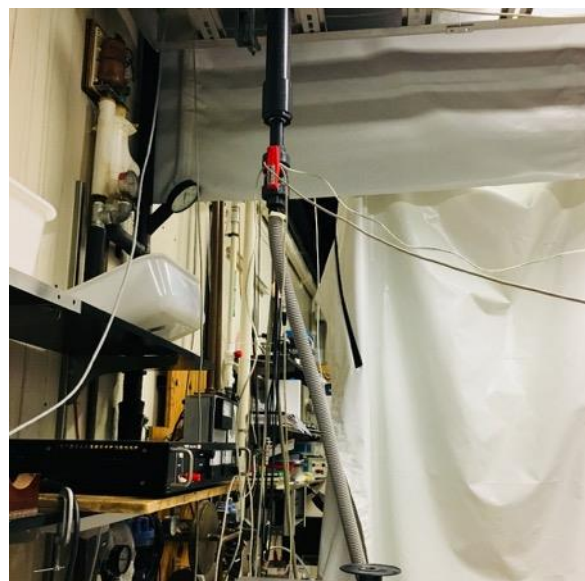


Figure B.9. Vacuum pump connected to exhaust.

off the turbo pump and pump the jacket down using the roughing pump to below 10^{-4} before running the turbo pump.

- h. After a day running the pump, the jacket pressure should be lowered down to 10^{-6} mbar.
2. Purge: evacuate air from the He reservoir and sample space. Figure B.10 shows the cryostat system's pipes, valves, and gas tank. Figure B.11 shows the schematic of the system with the valves numbered.
 - a. Turn on vacuum pump on. At least one of the valves must be open. Recovery should be open after last use at this point. Open exhaust valve, then close recovery valve.
 - b. Close the closest valves to the pump and read pressure gauge to see if there is no leak.
 - c. Fill the oil (cold) trap bucket with LN₂: this is to prevent any vapors from flowing back into the vacuum pump. The cold LN₂ will condense the vapor and keep them from flowing backwards and damaging the pump.



Figure B.10. Photograph showing pipes, valves, and He₂ gas tank.

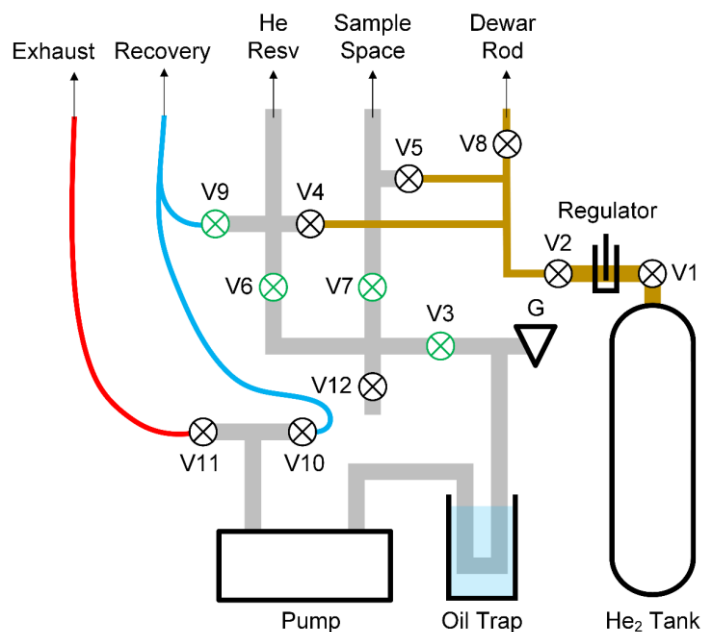


Figure B.11. Schematic diagram of cryostat vacuum pump.

- d. Close **V12** and open **V3**: don't evacuate the atmosphere. At every stage, check the pressure gauge to see if everything is working properly.
 - e. Open **V7** to evacuate the sample space.
 - f. Open **V6** in a moment to evacuate the He reservoir. The He reservoir's pressure must be higher than the sample space pressure.
 - g. After a minute or so, close **V6** then close **V7**.
 - h. Open **V4** and **V5**.
3. Fill sample space and He reservoir with He₂ gas.
 - a. Open **V1**. Pressure gauge before and after the regulator should show reading. Regulator controls the He₂ gas flow.
 - b. Make sure **V8** is closed and open **V2**.
4. Sample holder should be removable at this point since He₂ gas is flowing into sample space. Take out the sample holder and mount samples. Put the sample holder back into the chamber.
5. Disconnect turbo pump.
 - a. Close the valve and be prepared to pour LN₂ into the nitrogen reservoir.
 - b. Turn off turbo pump and disconnect from jacket valve, then connect power to vent.
6. Pour LN₂ into nitrogen reservoir.
 - a. Make sure heating coils are wrapped around cryostat chamber as in Figure B.12. Turn on heating coils so that the knobs don't freeze up.
 - b. Open needle slightly so that it doesn't jam after contraction due to the temperature drop.
7. Close **V4** and **V5**.
8. Measure level of liquid He in the dewar.
 - a. Open valve on the side of the dewar.

- b. Open top cap of the dewar.
 - c. Put in the measuring tube into the dewar. The rubber membrane on top of the tube will start to vibrate at a higher frequency once the tube hits the surface of liquid He. Temperature increase due to contact with the tube vaporizes liquid He into the tube.
 - d. Mark the level with the clip. The surface level is important to know in the transferring procedure.
9. Transfer liquid He from dewar to the He reservoir.
- a. Insert transfer rod in dewar, but above the surface. Keep the other end of the rod hanging outside of the cryostat.
 - b. Open **V8**: the dewar end of rod has a slit that lets He₂ gas flow into the dewar. The He₂ gas pushes the liquid He into the cryostat reservoir. Wait for a minute to purge the rod, after seeing gas coming out to the other end.

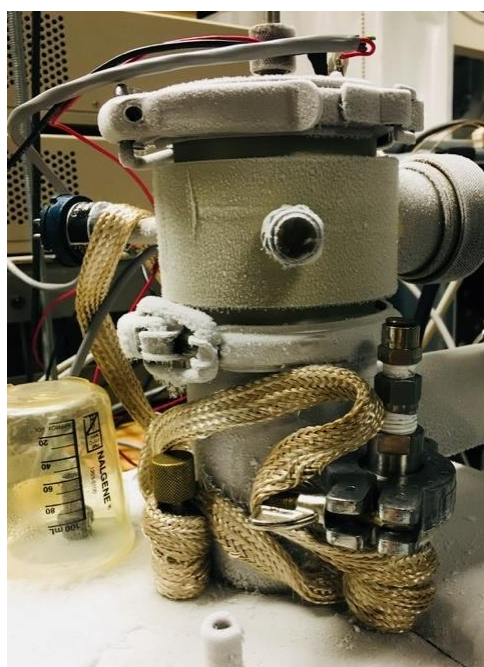


Figure B.12. Cryostat chamber with liquid N₂ filled and heating coils wrapped around knobs.

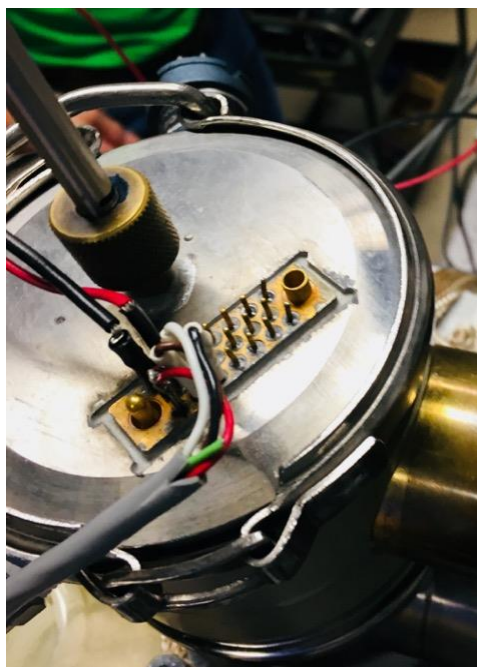


Figure B.13. Wire connection on top of the sample space used to measure and control temperature.

- c. Insert cryostat end of the rod in the cryostat.
 - d. Insert dewar end rod below liquid He surface. At this point, **V4** should be closed so that He₂ gas is not flowing into the reservoir. If He₂ gas is flowing to both the dewar and the reservoir, liquid He will not flow into reservoir. Conversely, if the gas is only flowing into the reservoir and not to the dewar, the liquid He will flow back to the dewar, which might contaminate the liquid He inside the dewar.
 - e. Turn on the liquid He level sensor (*AMI 135*). The update mode shows the real-time level whereas the sample mode only updates the level reading hourly.
 - f. Close **V8**. Take cryostat end of rod out and dewar end out.
 - g. Close **V2** and **V1**. Vent He₂ gas tube by opening **V8**. After hearing the hiss close **V8**.
10. Open path to He recovery by opening **V10** and **V9**, then close **V11**.
11. Control liquid He flow from reservoir to sample space by adjusting needle opening and **V7**.
12. Connect temperature controller wires to leads on top of the sample space cap to monitor and control temperature inside the cryostat as in Figure B.13.

APPENDIX C NUMERICAL CALCUALTION OF SCATTERING BETWEEN ELECTRONS AND OPTICAL PHONONS IN GaN-BASED QUANTUM WELLS

This section contains the MATLAB program files used to perform the numerical calculations described in Chapter 3. The code consists of one main function and three subfunctions. The subfunction `KP_IF` calculates the dispersion relation of the interface mode optical phonons and their scattering rates with electrons. The subfunction `KP_CONFINED` calculates those related to the confined mode optical phonons. The subfunctions also calculate the group velocities of the emitted optical phonons as a function of phonon frequency and the overall average group velocity as a function of the electron energy they scatter with. The `SOLVE_k` subfunction solves for k_1 and k_2 which are the electron wave vectors inside and outside of the finite quantum well.

C.1 Main Function

```
global hbar0 q0 m0 kBT c0 aB hbarc m_eff m d V0
%-- Fundamental physical parameters
hbar0 = 1.05457180e-34; % [J-s]
q0 = 1.60217662e-19; % [Coulombs]
m0 = 9.10938356e-31; % [kg]
kB = 1.38064852e-23; % [J/K]
T = 300; % [K]
kBT = kB*T; % [J]
eps0 = 8.854187817e-12; % [F/m]
c0 = 299792458; % [m/s]
aB = hbar0^2/q0^2; % [(J-s)^2/C^2]=[ (C-V-s)^2/C^2]=[ (V-s)^2]
hbarc = 2*pi*hbar0*c0; % [J-m]: actually hc not hbarc

m_eff = 0.22; % effective mass of electrons in GaN
m = m_eff*m0;
d = 5.0e-9; % quantum well thickness
V0 = 2.3*q0; % conduction band offset

[k1,k2] = SOLVE_k;

%-- Phonon frequencies
%- GaN
w_lz = 53100*c0; % A1(TO) [1/s]
```

```

w_1t = 55900*c0;           % E1(TO) [1/s]
w_1Lz = 73400*c0;          % A1(LO) [1/s]
w_1Lt = 74100*c0;          % E1(LO) [1/s]
eps_1 = 5.35*eps0;          % [F/m]

%-- AlN
w_2z = 61100*c0;           % A1(TO) [1/s]
w_2t = 67100*c0;           % E1(TO) [1/s]
w_2Lz = 89000*c0;          % A1(LO) [1/s]
w_2Lt = 91200*c0;          % E1(LO) [1/s]
eps_2 = 4.77*eps0;          % [F/m]

w1 = struct('z',w_1z,'t',w_1t,'Lz',w_1Lz,'Lt',w_1Lt);
w2 = struct('z',w_2z,'t',w_2t,'Lz',w_2Lz,'Lt',w_2Lt);

%-- Inputs
E1_TO = 5e-5*q0;           % IF cutoff energy [J]
E1_LO = 5e-5*q0;           % 
E2_TO = 1e-5*q0;           % C cutoff energy [J]
E2_LO = 1e-5*q0;           % 
fig_flag = 0;              % plot figures?
Nw = 2000;                 % number of omegas
NEk = 501;                 % number of energies
hEk = 0.5;                 % upper limit of energy
nMODE = 1:1;
Ek_eV = linspace(0,hEk,NEk)';

%-- Dielectric functions
w = linspace(40000,100000,6001)*c0;

e1z = eps_1*(w.^2-w1.Lz^2)./(w.^2-w1.z^2);
e1t = eps_1*(w.^2-w1.Lt^2)./(w.^2-w1.t^2);
e2z = eps_2*(w.^2-w2.Lz^2)./(w.^2-w2.z^2);
e2t = eps_2*(w.^2-w2.Lt^2)./(w.^2-w2.t^2);

xi1 = sqrt(abs(e1z.*e1t));
xi2 = sqrt(abs(e2z.*e2t));

figure; plot(w/c0/100,e1z/eps0,'k'); hold on; grid minor;
plot(w/c0/100,e1t/eps0,'r');
plot(w/c0/100,e2z/eps0,'b');
plot(w/c0/100,e2t/eps0,'m');
hold off;
ylim([-20 30]);
xlabel('Phonon Frequency \omega (cm^{-1})', 'FontWeight', 'normal');
ylabel('Dielectric Constant Conditions', 'FontWeight', 'normal');

figure; semilogy(w/c0/100,xi1,'r'); hold on; grid minor;
semilogy(w/c0/100,xi2,'b');
hold off;

```

```

%----- INTERFACE PHONONS -----
wTO = linspace(w1.t/c0+10,w2.z/c0-10,Nw)*c0;
wLO = linspace(w1.Lt/c0+10,w2.Lz/c0-10,Nw)*c0;

[qIF_TO,wIF_TO,VgIF_TO,WkIF_Em_TO,WkIF_Ab_TO,dWkIF_Em_TO] =
KP_IF('TO',wTO,w1,w2,eps_1,eps_2,Ek_eV,E1_TO,k1,k2);
[qIF_LO,wIF_LO,VgIF_LO,WkIF_Em_LO,WkIF_Ab_LO,dWkIF_Em_LO] =
KP_IF('LO',wLO,w1,w2,eps_1,eps_2,Ek_eV,E1_LO,k1,k2);

wIF_SyTO_cm = wIF_TO.Sy/100/c0;
wIF_AsyTO_cm = wIF_TO.Asy/100/c0;
wIF_SyLO_cm = wIF_LO.Sy/100/c0;
wIF_AsyLO_cm = wIF_LO.Asy/100/c0;

%- IF: Average group velocity
dVgIF_SyEm_TO = dWkIF_Em_TO.Sy.*(ones(NEk,1)*abs(VgIF_TO.Sy));
dVgIF_AsyEm_TO = dWkIF_Em_TO.Asy.*(ones(NEk,1)*abs(VgIF_TO.Asy));
dVgIF_SyEm_LO = dWkIF_Em_LO.Sy.*(ones(NEk,1)*abs(VgIF_LO.Sy));
dVgIF_AsyEm_LO = dWkIF_Em_LO.Asy.*(ones(NEk,1)*abs(VgIF_LO.Asy));
VgIF_SyEm_TO = trapz(wIF_TO.Sy,dVgIF_SyEm_TO,2);
VgIF_AsyEm_TO = trapz(wIF_TO.Asy,dVgIF_AsyEm_TO,2);
VgIF_SyEm_LO = trapz(wIF_LO.Sy,dVgIF_SyEm_LO,2);
VgIF_AsyEm_LO = trapz(wIF_LO.Asy,dVgIF_AsyEm_LO,2);
VgIF_Em =
(VgIF_SyEm_TO+VgIF_AsyEm_TO+VgIF_SyEm_LO+VgIF_AsyEm_LO)./(WkIF_Em_TO.Sy+WkIF
_Em_TO.Asy+WkIF_Em_LO.Sy+WkIF_Em_LO.Asy);

%----- CONFINED PHONONS -----
wC_TO = linspace(w1.z/c0+10,w1.t/c0-10,Nw)*c0;
wC_LO = linspace(w1.Lz/c0+10,w1.Lt/c0-10,Nw)*c0;

wC_TO_cm = wC_TO/100/c0;
wC_LO_cm = wC_LO/100/c0;

%-- Dispersion and scattering rate calculation for each branch
%- Symmetric modes
[qCSy_TO,VgCSy_TO,WkC_SyEm_TO,WkC_SyAb_TO,dWkC_SyEm_TO] =
KP_CONFINED('sym',nMODE,'lo',wC_TO,w1,w2,eps_1,eps_2,Ek_eV,E2_TO,k1,k2);
[qCSy_LO,VgCSy_LO,WkC_SyEm_LO,WkC_SyAb_LO,dWkC_SyEm_LO] =
KP_CONFINED('sym',nMODE,'lo',wC_LO,w1,w2,eps_1,eps_2,Ek_eV,E2_LO,k1,k2);

%- Asymmetric modes
[qCAsy_TO,VgCAsy_TO,WkC_AsyEm_TO,WkC_AsyAb_TO,dWkC_AsyEm_TO] =
KP_CONFINED('asym',nMODE,'lo',wC_TO,w1,w2,eps_1,eps_2,Ek_eV,E2_TO,k1,k2);
[qCAsy_LO,VgCAsy_LO,WkC_AsyEm_LO,WkC_AsyAb_LO,dWkC_AsyEm_LO] =
KP_CONFINED('asym',1:2,'lo',wC_LO,w1,w2,eps_1,eps_2,Ek_eV,E2_LO,k1,k2);

%- Sign correction
WkC_SyEm_TO = abs(WkC_SyEm_TO);
WkC_SyEm_LO = abs(WkC_SyEm_LO);

```

```

WkC_AsyEm_TO = abs(WkC_AsyEm_TO);
WkC_AsyEm_LO = abs(WkC_AsyEm_LO);
WkC_SyAb_TO = abs(WkC_SyAb_TO);
WkC_SyAb_LO = abs(WkC_SyAb_LO);
WkC_AsyAb_TO = abs(WkC_AsyAb_TO);
WkC_AsyAb_LO = abs(WkC_AsyAb_LO);

WkC_Em_TO = WkC_SyEm_TO+WkC_AsyEm_TO;
WkC_Em_LO = WkC_SyEm_LO+WkC_AsyEm_LO;
WkC_Ab_TO = WkC_SyAb_TO + WkC_AsyAb_TO;
WkC_Ab_LO = WkC_SyAb_LO + WkC_AsyAb_LO;
WkC_Em = WkC_Em_TO + WkC_Em_LO;
WkC_Ab = WkC_Ab_TO + WkC_Ab_LO;
WkC = WkC_Em + WkC_Ab;
WkIF_TE = WkIF_Em_TO.Asy + WkIF_Em_TO.Sy;
WkIF_TA = WkIF_Ab_TO.Asy + WkIF_Ab_TO.Sy;
WkIF_LE = WkIF_Em_LO.Asy + WkIF_Em_LO.Sy;
WkIF_LA = WkIF_Ab_LO.Asy + WkIF_Ab_LO.Sy;
WkIF_Em = WkIF_TE+WkIF_LE;
WkIF_Ab = WkIF_TA+WkIF_LA;
WkIF = WkIF_Em+WkIF_Ab;
Wk = WkC + WkIF;

% %-- FIGURES
%- IF and CONFINED Dispersion
figure; plot(qIF_TO.Sy*d,wIF_SyTO_cm,'b'); grid minor; hold on;
plot(qIF_TO.Asy*d,wIF_AsyTO_cm,'r');
plot(qIF_LO.Sy*d,wIF_SyLO_cm,'b');
plot(qIF_LO.Asy*d,wIF_AsyLO_cm,'r');
plot(qCSy_TO*d,wC_TO_cm,'b');
plot(qCAsy_TO*d,wC_TO_cm,'r');
plot(qCSy_LO*d,wC_LO_cm,'b');
plot(qCAsy_LO(2,:) *d,wC_LO_cm,'r');
hold off;
% xlim([0 12]);
xlabel('Wave Vector qd', 'FontWeight', 'normal');
ylabel('Phonon Frequency \omega (cm^{-1})', 'FontWeight', 'normal');
legend('Symmetric','Asymmetric','Location','southeast');

%- IF Total scattering rate
figure; semilogy(Ek_eV,WkIF,'k'); grid minor; hold on;
semilogy(Ek_eV,WkIF_Em,'--b');
semilogy(Ek_eV,WkIF_LE,'--m');
semilogy(Ek_eV,WkIF_TE,':m');
semilogy(Ek_eV,WkIF_Ab,'--r');
ylim([1e11 1e14]);
hold off;
xlabel('Electron Energy E_{k}(eV)', 'FontWeight', 'normal');
ylabel('IF Total Scattering Rate (s^{-1})', 'FontWeight', 'normal');
legend('Total','Emission','Absorption','Location','southeast');

```

```

%- IF and CONFINED Total scattering rate
figure; semilogy(Ek_eV,Wk,'k'); grid minor; hold on;
semilogy(Ek_eV,WkC,'--b');
semilogy(Ek_eV,WkIF,'--r');
hold off;
xlabel('Electron Energy E_{k}(eV)', 'FontWeight', 'normal');
ylabel('IF+C Total Scattering Rate (s^{-1})', 'FontWeight', 'normal');
legend('Total','Confined','IF','Location','southeast');

```

C.2 Subfunction: Interface Optical Phonons

```

function [qIF,wIF,VgIF,Wk_emi,Wk_abs,dWk_emi] =
KP_IF(TOLO,w,w1,w2,eps_1,eps_2,Ek_eV,E0,k1,k2)
global hbar0 q0 kBT c0 aB m d

e1z = eps_1*(w.^2-w1.Lz^2)./(w.^2-w1.z^2);
e1t = eps_1*(w.^2-w1.Lt^2)./(w.^2-w1.t^2);
e2z = eps_2*(w.^2-w2.Lz^2)./(w.^2-w2.z^2);
e2t = eps_2*(w.^2-w2.Lt^2)./(w.^2-w2.t^2);

xi1 = sqrt(abs(e1z.*e1t));
xi2 = sqrt(abs(e2z.*e2t));

alpha = 0.5*sqrt(abs(e1t./e1z));
beta = 0.5*sqrt(abs(e2t./e2z));

if strcmp(TOLO,'TO')
    q = 0.5*log((xi1+xi2)./(xi1-xi2))./(alpha*d);
    iq = find(imag(q)~=0,1)-1;
    q = real(q);
    q_sym = q(1:iq);
    q_asym = q(iq+1:end);
    w_sym = w(1:iq);
    w_asym = w(iq+1:end);
elseif strcmp(TOLO,'LO')
    q = 0.5*log((xi1+xi2)./(xi1-xi2))./(alpha*d);
    iq = find(imag(q)==0,1)-1;
    q = real(q);
    q_asym = q(1:iq);
    q_sym = q(iq+1:end);
    w_asym = w(1:iq);
    w_sym = w(iq+1:end);
end

qIF = struct('Sy',q_sym,'Asy',q_asym);
wIF = struct('Sy',w_sym,'Asy',w_asym);

w_sym_cm = w_sym/100/c0;

```

```

w_asym_cm = w_asym/100/c0;

Eq = hbar0^2*q.^2/(2*m);
if strcmp(TOLO,'TO')
    Eq_sym = Eq(1:iq);
    Eq_asym = Eq(iq+1:end);
elseif strcmp(TOLO,'LO')
    Eq_asym = Eq(1:iq);
    Eq_sym = Eq(iq+1:end);
end

Nqs = length(w_sym);
Nqa = length(w_asym);

Ek = Ek_eV*q0;
[NEk,~] = size(Ek);

delzdw = 2*eps_1*(w./(w.^2 - w1.z^2) - w.*(w.^2 - w1.Lz^2)./(w.^2 -
w1.z^2).^2);
deltdw = 2*eps_1*(w./(w.^2 - w1.t^2) - w.*(w.^2 - w1.Lt^2)./(w.^2 -
w1.t^2).^2);
de2zdw = 2*eps_2*(w./(w.^2 - w2.z^2) - w.*(w.^2 - w2.Lz^2)./(w.^2 -
w2.z^2).^2);
de2tdw = 2*eps_2*(w./(w.^2 - w2.t^2) - w.*(w.^2 - w2.Lt^2)./(w.^2 -
w2.t^2).^2);

%-- Full D IF
zetalp = deltdw./(2*alpha)+2*delzdw.*alpha;
zetaln = deltdw./(2*alpha)-2*delzdw.*alpha;
zeta2p = de2tdw./(2*beta)+2*de2zdw.*beta;

ups = (sin(k1*d)./(2*k1) + d/2 + cos(k1*d/2).^2./k2).^(-0.5);

FF2 = ups.^4.*(cos(k1*d/2).^2.*cosh(alpha.*q*d)./(k2+beta.*q) +
((2*cos(k1*d/2).^2.*alpha.^2.*q.^2+k1.^2).*sinh(alpha.*q*d) +
alpha.*q.*k1.*cosh(alpha.*q*d).*sin(k1*d))./(2*alpha.*q.*(alpha.^2.*q.^2+k1.
^2))).^2;
f = cosh(alpha.*q*d).^2.*zeta2p + alpha.*q*d.*zetaln +
sinh(alpha.*q*d).*zetalp;
DIF = FF2./f;

if strcmp(TOLO,'TO')
    DIF_sym = ones(NEk,1)*DIF(1:iq);
    DIF_asym = ones(NEk,1)*DIF(iq+1:end);
elseif strcmp(TOLO,'LO')
    DIF_asym = ones(NEk,1)*DIF(1:iq);
    DIF_sym = ones(NEk,1)*DIF(iq+1:end);
end

Vg_sym = 2*pi*([w_sym(2:end) w_sym(end)]-[w_sym(1) w_sym(1:end-
1)])./([q_sym(2:end) q_sym(end)]-[q_sym(1) q_sym(1:end-1)]);

```



```

Vg_asym = 2*pi*([w_asym(2:end) w_asym(end)]-[w_asym(1) w_asym(1:end-1)])./([q_asym(2:end) q_asym(end)]-[q_asym(1) q_asym(1:end-1)]);
VgIF = struct('Sy',Vg_sym,'Asy',Vg_asym);

Vp_sym = 2*pi*w_sym./q_sym;
Vp_asym = 2*pi*w_asym./q_asym;

if strcmp(TOLO,'TO')
    sigma_emi_sym = ones(NEk,Nqs);
    sigma_emi_asym = -ones(NEk,Nqa);
    sigma_abs_sym = ones(NEk,Nqs);
    sigma_abs_asym = -ones(NEk,Nqa);
elseif strcmp(TOLO,'LO')
    sigma_emi_sym = -ones(NEk,Nqs);
    sigma_emi_asym = ones(NEk,Nqa);
    sigma_abs_sym = -ones(NEk,Nqs);
    sigma_abs_asym = ones(NEk,Nqa);
end

templ_emi_sym = ones(NEk,1)*(0.5*q_sym-(m/hbar0)*(Vp_sym-Vg_sym));
templ_emi_asym = ones(NEk,1)*(0.5*q_asym-(m/hbar0)*(Vp_asym-Vg_asym));
templ_abs_sym = ones(NEk,1)*(0.5*q_sym+(m/hbar0)*(Vp_sym-Vg_sym));
templ_abs_asym = ones(NEk,1)*(0.5*q_asym+(m/hbar0)*(Vp_asym-Vg_asym));

%-- sqrt w/ E0
temp2_emi_sym = (sqrt(1/m*(2*Ek*ones(1,Nqs)+ones(NEk,1)*(-0.5*Eq_sym - hbar0*2*pi*w_sym))-ones(NEk,1)*Vp_sym.^2) + sqrt(E0/m)).^2./sqrt(1/m*(2*Ek*ones(1,Nqs)+ones(NEk,1)*(-0.5*Eq_sym - hbar0*2*pi*w_sym))-ones(NEk,1)*Vp_sym.^2);
temp2_emi_asym = (sqrt(1/m*(2*Ek*ones(1,Nqa)+ones(NEk,1)*(-0.5*Eq_asym - hbar0*2*pi*w_asym))-ones(NEk,1)*Vp_asym.^2) + sqrt(E0/m)).^2./sqrt(1/m*(2*Ek*ones(1,Nqa)+ones(NEk,1)*(-0.5*Eq_asym - hbar0*2*pi*w_asym))-ones(NEk,1)*Vp_asym.^2);
temp2_abs_sym = (sqrt(1/m*(2*Ek*ones(1,Nqs)+ones(NEk,1)*(-0.5*Eq_sym + hbar0*2*pi*w_sym))-ones(NEk,1)*Vp_sym.^2) + sqrt(E0/m)).^2./sqrt(1/m*(2*Ek*ones(1,Nqs)+ones(NEk,1)*(-0.5*Eq_sym + hbar0*2*pi*w_sym))-ones(NEk,1)*Vp_sym.^2);
temp2_abs_asym = (sqrt(1/m*(2*Ek*ones(1,Nqa)+ones(NEk,1)*(-0.5*Eq_asym + hbar0*2*pi*w_asym))-ones(NEk,1)*Vp_asym.^2) + sqrt(E0/m)).^2./sqrt(1/m*(2*Ek*ones(1,Nqa)+ones(NEk,1)*(-0.5*Eq_asym + hbar0*2*pi*w_asym))-ones(NEk,1)*Vp_asym.^2);

sigma_emi_sym(imag(temp2_emi_sym)~=0) = 0;
sigma_emi_asym(imag(temp2_emi_asym)~=0) = 0;
sigma_abs_sym(imag(temp2_abs_sym)~=0) = 0;
sigma_abs_asym(imag(temp2_abs_asym)~=0) = 0;

temp3_emi_sym = -ones(NEk,1)*((Vp_sym./q_sym - 0.5*hbar0/m)./Vg_sym-1./q_sym);
temp3_emi_asym = -ones(NEk,1)*((Vp_asym./q_asym - 0.5*hbar0/m)./Vg_asym-1./q_asym);

```

```

temp3_abs_sym = ones(NEk,1)*((Vp_sym./q_sym + 0.5*hbar0/m)./Vg_sym-
1./q_sym);
temp3_abs_asym = ones(NEk,1)*((Vp_asym./q_asym + 0.5*hbar0/m)./Vg_asym-
1./q_asym);

Nw_sym = ones(NEk,1)*(1./(exp(hbar0*2*pi*w_sym/kBT)-1));
Nw_asym = ones(NEk,1)*(1./(exp(hbar0*2*pi*w_asym/kBT)-1));

dWk_emi_sym =
(2*m/aB)*sigma_emi_sym.*(Nw_sym+1).*DIF_sym.*temp3_emi_sym./(temp1_emi_sym.*
temp2_emi_sym);
Wk_emi_sym = trapz(w_sym,dWk_emi_sym,2);
dWk_emi_asym
=(2*m/aB)*sigma_emi_asym.*(Nw_asym+1).*DIF_asym.*temp3_emi_asym./(temp1_emi_
asym.*temp2_emi_asym);
Wk_emi_asym = trapz(w_asym,dWk_emi_asym,2);
dWk_abs_sym =
(2*m/aB)*sigma_abs_sym.*(Nw_sym).*DIF_sym.*temp3_abs_sym./(temp1_abs_sym.*te
mp2_abs_sym);
Wk_abs_sym = trapz(w_sym,dWk_abs_sym,2);
dWk_abs_asym =
(2*m/aB)*sigma_abs_asym.*(Nw_asym).*DIF_asym.*temp3_abs_asym./(temp1_abs_asy
m.*temp2_abs_asym);
Wk_abs_asym = trapz(w_asym,dWk_abs_asym,2);

dWk_emi = struct('Sy',dWk_emi_sym,'Asy',dWk_emi_asym);
Wk_emi = struct('Sy',Wk_emi_sym,'Asy',Wk_emi_asym);
Wk_abs = struct('Sy',Wk_abs_sym,'Asy',Wk_abs_asym);

%- Figure: phonon-freq dep. scattering rate
meV120 = find(Ek_eV == 0.1);
meV300 = find(Ek_eV == 0.3);
% meV500 = find(Ek_eV == 0.5);
figure; semilogy(w_asym_cm,dWk_emi_asym(meV120,:),'b'); grid minor; hold on;
semilogy(w_asym_cm,dWk_emi_asym(meV300,:),'r');
semilogy(w_asym_cm,dWk_emi_asym(NEk,:),'k');
semilogy(w_sym_cm,dWk_emi_sym(meV120,:),'b');
semilogy(w_sym_cm,dWk_emi_sym(meV300,:),'r');
semilogy(w_sym_cm,dWk_emi_sym(NEk,:),'k');
hold off;
xlabel('Phonon Frequency \omega (cm^{-1})','FontWeight','normal');
ylabel('Scattering Rate (s^{-1}/s^{-1})','FontWeight','normal');
legend('E_{k} = 0.12 eV','E_{k} = 0.3 eV','E_{k} = 0.5
eV','Location','southeast');

end

```

C.3 Subfunction: Confined Optical Phonons

```
function [qc,Vg,Wk_emi,Wk_abs,dWk_emi] =
KP_CONFINED(MODE,nMODE,HILO,w,w1,w2,eps_1,eps_2,Ek_eV,E0,k1,k2)
global d hbar0 m q0 kBT aB

elz = eps_1*(w.^2-w1.Lz^2)./(w.^2-w1.z^2);
elt = eps_1*(w.^2-w1.Lt^2)./(w.^2-w1.t^2);
e2z = eps_2*(w.^2-w2.Lz^2)./(w.^2-w2.z^2);
e2t = eps_2*(w.^2-w2.Lt^2)./(w.^2-w2.t^2);

xi1 = sqrt(abs(elt.*elt));
xi2 = sqrt(abs(e2z.*e2t));

alpha = 0.5*sqrt(abs(elt./elz));
beta = 0.5*sqrt(abs(e2t./e2z));
mu = sign(elz.*e2z);

qc = zeros(length(nMODE),length(w));
Nq = length(qc);

for n = nMODE
    if strcmp(MODE,'sym')
        if strcmp(HILO,'lo')
            qc(n,:) = (n*pi + mu.*atan(xi2./xi1))./(alpha*d);
        elseif strcmp(HILO,'hi')
            qc(n,:) = ((n-1)*pi + mu.*atan(xi2./xi1))./(beta*d);
        end

        elseif strcmp(MODE,'asym')
            if strcmp(HILO,'lo')
                qc(n,:) = ((n-1)*pi - mu.*atan(xi1./xi2))./(alpha*d);
            elseif strcmp(HILO,'hi')
                qc(n,:) = (n*pi - mu.*atan(xi1./xi2))./(beta*d);
            end
        end
    end
end

Ek = Ek_eV*q0;
[NEk,~] = size(Ek);

delzdw = 2*eps_1*(w./(w.^2 - w1.z^2) - w.*(w.^2 - w1.Lz^2)./(w.^2 -
w1.z^2).^2);
deltdw = 2*eps_1*(w./(w.^2 - w1.t^2) - w.*(w.^2 - w1.Lt^2)./(w.^2 -
w1.t^2).^2);
de2zdw = 2*eps_2*(w./(w.^2 - w2.z^2) - w.*(w.^2 - w2.Lz^2)./(w.^2 -
w2.z^2).^2);
de2tdw = 2*eps_2*(w./(w.^2 - w2.t^2) - w.*(w.^2 - w2.Lt^2)./(w.^2 -
w2.t^2).^2);
```

```

%-- Full D C
zeta1p = deltdw./(2*alpha)+2*delzdw.*alpha;
zeta1n = deltdw./(2*alpha)-2*delzdw.*alpha;
zeta2p = de2tdw./(2*beta)+2*de2zdw.*beta;

Wk_emi = zeros(NEk,length(nMODE));
Wk_abs = zeros(NEk,length(nMODE));

Vg = zeros(length(nMODE),length(w));
Vp = zeros(length(nMODE),length(w));

for n = nMODE
    q = qc(n,:);
    Eq = hbar0^2*q.^2/(2*m);

    ups = (sin(k1*d)./(2*k1) + d/2 + cos(k1*d/2).^2./k2).^(-0.5);
    FF2 = ups.^4.*(cos(k1*d/2).^2.*cos(alpha.*q*d)./(k2+beta.*q) +
    ((2*cos(k1*d/2).^2.*alpha.^2.*q.^2-k1.^2).*sin(alpha.*q*d) -
    alpha.*q.*k1.*cos(alpha.*q*d).*sin(k1*d))./(2*alpha.*q.*(alpha.^2.*q.^2-
    k1.^2))).^2;
    f = cos(alpha.*q*d).^2.*zeta2p + alpha.*q*d.*zeta1p +
    sin(alpha.*q*d).*cos(alpha.*q*d).*zeta1n;
    DC = FF2./f;
    DC = ones(NEk,1)*DC;

    Vg(n,:) = 2*pi*([w(2:end) w(end)]-[w(1) w(1:end-1)])./([q(2:end)
    q(end)]-[q(1) q(1:end-1)]);
    Vp(n,:) = 2*pi*w./q;

    sigma_emi = ones(NEk,Nq);
    sigma_abs = ones(NEk,Nq);

    temp1_emi = ones(NEk,1)*(0.5*q-(m/hbar0)*(Vp(n,:)-Vg(n,:)));
    temp1_abs = ones(NEk,1)*(0.5*q+(m/hbar0)*(Vp(n,:)-Vg(n,:)));

    temp2_emi = (sqrt(1/m*(2*Ek*ones(1,Nq)+ones(NEk,1)*(-0.5*Eq -
    hbar0*2*pi*w))-ones(NEk,1)*Vp(n,:).^2) +
    sqrt(E0/m)).^2./sqrt(1/m*(2*Ek*ones(1,Nq)+ones(NEk,1)*(-0.5*Eq -
    hbar0*2*pi*w))-ones(NEk,1)*Vp(n,:).^2);
    temp2_abs = (sqrt(1/m*(2*Ek*ones(1,Nq)+ones(NEk,1)*(-0.5*Eq +
    hbar0*2*pi*w))-ones(NEk,1)*Vp(n,:).^2) +
    sqrt(E0/m)).^2./sqrt(1/m*(2*Ek*ones(1,Nq)+ones(NEk,1)*(-0.5*Eq +
    hbar0*2*pi*w))-ones(NEk,1)*Vp(n,:).^2);

    sigma_emi(imag(temp2_emi)~=0) = 0;
    sigma_abs(imag(temp2_abs)~=0) = 0;

    temp3_emi = -ones(NEk,1)*((Vp(n,:)./q - 0.5*hbar0/m)./Vg(n,:) - 1./q);
    temp3_abs = ones(NEk,1)*((Vp(n,:)./q + 0.5*hbar0/m)./Vg(n,:) - 1./q);

```

```

Nw = ones(NEk,1)*(1./(exp(hbar0*2*pi*w/kBT)-1));

dWk_emi =
(2*m/aB)*sigma_emi.*(Nw+1).*DC.*temp3_emi./(temp1_emi.*temp2_emi);
Wk_emi(:,n) = trapz(w,dWk_emi,2);
dWk_abs =
(2*m/aB)*sigma_abs.*(Nw).*DC.*temp3_abs./(temp1_abs.*temp2_abs);
Wk_abs(:,n) = trapz(w,dWk_abs,2);
end

Wk_emi = sum(Wk_emi,2);
Wk_abs = sum(Wk_abs,2);

end

```

C.4 Subfunction: Electron Wave Vectors

```

function [k1,k2] = SOLVE_k()
global hbar0 d m V0

roundd = round(d,1,'significant')*1e9;
switch roundd
    case 20
        k = 1.615130236490229e8;
    case 10
        k = 2.9e8;
    case 5
        k = 5.659474067051942e8;
    case 4
        k = 6.901357880170896e8;
    case 3
        k = 8.838774058207904e8;
    case 2
        k = 1.227306970645387e9;
    case 1
        k = 1.987757079903387e9;
end

k1 = fzero(@(k1) k1.^2.*(1+tan(k1*d/2).^2)-2*m*V0/hbar0^2,k);
k2 = k1*tan(k1*d/2);

end

```

REFERENCES

- [1] F. Iacopi, M. Van Hove, M. Charles, and K. Endo, “Power electronics with wide bandgap materials: Toward greener, more efficient technologies,” *MRS Bull.*, vol. 40, no. 5, pp. 390–395, 2015.
- [2] M. H. Rashid, *Power Electronics Handbook*. Butterworth-Heinemann, 2017.
- [3] B. J. Baliga, “Gallium nitride devices for power electronic applications,” *Semicond. Sci. Technol.*, vol. 28, no. 7, 2013.
- [4] X. Chen, S. Boumaiza, and L. Wei, “Self-heating and equivalent channel temperature in short gate length GaN HEMTs,” *IEEE Trans. Electron Devices*, vol. 66, no. 9, pp. 3748–3755, 2019.
- [5] B. M. Paine, T. Rust, and E. A. Moore, “Measurement of temperature in GaN HEMTs by gate end-to-end resistance,” *IEEE Trans. Electron Devices*, vol. 63, no. 2, pp. 590–597, 2016.
- [6] S. Singhal *et al.*, “Reliability of large periphery GaN-on-Si HFETs,” *Microelectron. Reliab.*, vol. 46, no. 8, pp. 1247–1253, 2006.
- [7] K. Park, M. A. Strosio, and C. Bayram, “Investigation of electron mobility and saturation velocity limits in gallium nitride using uniaxial dielectric continuum model,” *J. Appl. Phys.*, vol. 121, no. 24, 2017.
- [8] U. K. Mishra, Shen Likun, T. E. Kazior, and Yi-Feng Wu, “GaN-based RF power devices and amplifiers,” *Proc. IEEE*, vol. 96, no. 2, pp. 287–305, Feb. 2008.
- [9] M. Kuball *et al.*, “Measurement of temperature distribution in multifinger AlGaIn/GaN heterostructure field-effect transistors using micro-Raman spectroscopy,” *Appl. Phys. Lett.*, vol. 82, no. 1, pp. 124–126, 2003.
- [10] O. Katz, A. Horn, G. Bahir, and J. Salzman, “Electron mobility in an AlGaIn/GaN two-dimensional electron gas I-carrier concentration dependent mobility,” *IEEE Trans. Electron Devices*, vol. 50, no. 10, pp. 2002–2008, Oct. 2003.

- [11] B. K. Ridley, B. E. Foutz, and L. F. Eastman, "Mobility of electrons in bulk GaN and $\text{Al}_x\text{Ga}_{1-x}\text{N}/\text{GaN}$ heterostructures," *Phys. Rev. B*, vol. 61, no. 24, pp. 16862–16869, Jun. 2000.
- [12] A. Matulionis *et al.*, "Hot-phonon temperature and lifetime in a biased $\text{Al}_x\text{Ga}_{1-x}\text{N}/\text{GaN}$ channel estimated from noise analysis," *Phys. Rev. B*, vol. 68, no. 3, p. 035338, Jul. 2003.
- [13] I. P. Smorchkova *et al.*, "AlN/GaN and (Al,Ga)N/AlN/GaN two-dimensional electron gas structures grown by plasma-assisted molecular-beam epitaxy," *J. Appl. Phys.*, vol. 90, no. 10, pp. 5196–5201, 2001.
- [14] R. Gaska *et al.*, "Electron transport in AlGaIn-GaN heterostructures grown on 6H-SiC substrates," *Appl. Phys. Lett.*, vol. 72, no. 6, pp. 707–709, 1998.
- [15] N. M. Stanton, A. J. Kent, A. V. Akimov, P. Hawker, T. S. Cheng, and C. T. Foxon, "Energy relaxation by hot electrons in n-GaN epilayers," *J. Appl. Phys.*, vol. 89, no. 2, pp. 973–979, 2001.
- [16] J. D. Albrecht, R. P. Wang, P. P. Ruden, M. Farahmand, and K. F. Brennan, "Electron transport characteristics of GaN for high temperature device modeling," *J. Appl. Phys.*, vol. 83, no. 9, pp. 4777–4781, 1998.
- [17] J. Z. Zhang, A. Dyson, and B. K. Ridley, "Momentum relaxation due to polar optical phonons in AlGaIn/GaN heterostructures," *Phys. Rev. B - Condens. Matter Mater. Phys.*, vol. 84, no. 15, pp. 1–11, 2011.
- [18] M. E. Mora-Ramos, V. R. Velasco, and J. Tutor, "Scattering of electrons by polar optical phonons in AlGaIn/GaN single heterostructures," *Surf. Sci.*, vol. 592, no. 1–3, pp. 112–123, 2005.
- [19] C. Bulutay, B. K. Ridley, and N. A. Zakhleniuk, "Full-band polar optical phonon scattering analysis and negative differential conductivity in wurtzite GaN," *Phys. Rev. B*, vol. 62, no. 23, pp. 15754–15763, Dec. 2000.
- [20] B. Lee, K. Kim, M. Dutta, and M. Strosio, "Electron-optical-phonon scattering in wurtzite crystals," *Phys. Rev. B - Condens. Matter Mater. Phys.*, vol. 56, no. 3, pp. 997–1000, 1997.

- [21] S. Chowdhury and U. K. Mishra, "Lateral and vertical transistors using the Algan/GaN Heterostructure," *IEEE Trans. Electron Devices*, vol. 60, no. 10, pp. 3060–3066, 2013.
- [22] G. Irmer, C. Röder, C. Himcinschi, and J. Kortus, "Phonon polaritons in uniaxial crystals: A Raman scattering study of polaritons in α -GaN," *Phys. Rev. B - Condens. Matter Mater. Phys.*, vol. 88, no. 10, 2013.
- [23] N. Mori and T. Ando, "Electronoptical-phonon interaction in single and double heterostructures," *Phys. Rev. B*, vol. 40, no. 9, pp. 6175–6188, 1989.
- [24] R. Loudon, "The Raman effect in crystals," *Adv. Phys.*, vol. 13, no. 52, pp. 423–482, 1964.
- [25] W. S. Li, Z. X. Shen, Z. C. Feng, and S. J. Chua, "Temperature dependence of Raman scattering in hexagonal gallium nitride films," *J. Appl. Phys.*, vol. 87, no. 7, pp. 3332–3337, 2000.
- [26] D. Maier *et al.*, "Testing the temperature limits of GaN-based HEMT devices," *IEEE Trans. Device Mater. Reliab.*, vol. 10, no. 4, pp. 427–436, 2010.
- [27] E. Ejder, "Refractive index of GaN," *Phys. Status Solidi*, vol. 6, no. 2, pp. 445–448, Aug. 1971.
- [28] Y. V. Davydov *et al.*, "Composition dependence of optical phonon energies and Raman line broadening in hexagonal (formula presented) alloys," *Phys. Rev. B - Condens. Matter Mater. Phys.*, vol. 65, no. 12, pp. 1–13, 2002.
- [29] M. A. Stroscio and M. Dutta, "Phonons in Nanostructures," *Phonons in Nanostructures*, 2001.
- [30] C. Chen, M. Dutta, and M. A. Stroscio, "Electron scattering via interactions with optical phonons in wurtzite crystals," *Phys. Rev. B - Condens. Matter Mater. Phys.*, vol. 70, no. 7, pp. 1–7, 2004.
- [31] B. K. Ridley, *Quantum Processes in Semiconductors*. Oxford University Press, 2013.
- [32] B. K. Ridley, W. J. Schaff, and L. F. Eastman, "Hot-phonon-induced velocity saturation in GaN," *J. Appl. Phys.*, vol. 96, no. 3, pp. 1499–1502, 2004.

- [33] B. Gelmont, K. Kim, and M. Shur, "Monte Carlo simulation of electron transport in gallium nitride," *J. Appl. Phys.*, vol. 74, no. 3, pp. 1818–1821, 1993.
- [34] B. L. Gelmont, M. Shur, and M. Strosio, "Polar optical-phonon scattering in three- and two-dimensional electron gases," *J. Appl. Phys.*, vol. 77, no. 2, pp. 657–660, 1995.
- [35] B. L. Gelmont, M. S. Shur, and M. Strosio, "Analytical theory of electron mobility and drift velocity in GaN," *MRS Proc.*, vol. 449, no. 1, p. 609, Feb. 1996.
- [36] D. K. Ferry, "High-field transport in wide-band-gap semiconductors," *Phys. Rev. B*, vol. 12, no. 6, pp. 2361–2369, 1975.
- [37] I. Ahmad *et al.*, "Self-heating study of an AlGaNGaN -based heterostructure field-effect transistor using ultraviolet micro-Raman scattering," *Appl. Phys. Lett.*, vol. 86, no. 17, pp. 1–3, 2005.
- [38] K. Park, A. Mohamed, M. Dutta, M. A. Strosio, and C. Bayram, "Electron scattering via interface optical phonons with high group velocity in wurtzite GaN-based quantum well heterostructure," *Sci. Rep.*, vol. 8, no. 1, p. 15947, Dec. 2018.
- [39] M. C. Schmidt *et al.*, "Demonstration of nonpolar m-plane InGaN/GaN laser diodes," *Japanese J. Appl. Physics, Part 2 Lett.*, vol. 46, no. 8–11, 2007.
- [40] U. K. Mishra, P. Parikh, and Y. F. Wu, "AlGaIn/GaN HEMTs - An overview of device operation and applications," *Proc. IEEE*, vol. 90, no. 6, pp. 1022–1031, 2002.
- [41] L. Lindsay, D. A. Broido, and T. L. Reinecke, "Thermal conductivity and large isotope effect in GaN from first principles," *Phys. Rev. Lett.*, vol. 109, no. 9, pp. 1–5, 2012.
- [42] A. A. Balandin, E. P. Pokatilov, and D. L. Nika, "Phonon engineering in hetero- and nanostructures," *J. Nanoelectron. Optoelectron.*, vol. 2, no. 2, pp. 140–170, 2007.
- [43] B. K. Ridley, "The LO phonon lifetime in GaN," *J. Phys. Condens. Matter*, vol. 8, no. 37, 1996.
- [44] S. Barman and G. P. Srivastava, "Long-wavelength nonequilibrium optical phonon dynamics in cubic and hexagonal semiconductors," *Phys. Rev. B - Condens. Matter Mater. Phys.*, vol. 69, no. 23, 2004.

- [45] J. Khurgin, Y. J. Ding, and D. Jena, “Hot phonon effect on electron velocity saturation in GaN: A second look,” *Appl. Phys. Lett.*, vol. 91, no. 25, pp. 1–4, 2007.
- [46] A. Matulionis *et al.*, “Novel fluctuation-based approach to optimization of frequency performance and degradation of nitride heterostructure field effect transistors,” *Phys. Status Solidi Appl. Mater. Sci.*, vol. 208, no. 1, pp. 30–36, 2011.
- [47] K. Sarkar *et al.*, “Raman analysis of phonon modes in a short period AlN/GaN superlattice,” *Superlattices Microstruct.*, vol. 115, pp. 116–122, 2018.
- [48] J. Gleize *et al.*, “Angular dispersion of polar phonons in a hexagonal GaN-AlN superlattice,” *Mater. Sci. Eng. B Solid-State Mater. Adv. Technol.*, vol. 82, no. 1–3, pp. 27–29, 2001.
- [49] B. Lee, K. Kim, M. Strosio, and M. Dutta, “Optical-phonon confinement and scattering in wurtzite heterostructures,” *Phys. Rev. B - Condens. Matter Mater. Phys.*, vol. 58, no. 8, pp. 4860–4865, 1998.
- [50] S. Komirenko, K. Kim, M. Strosio, and M. Dutta, “Energy-dependent electron scattering via interaction with optical phonons in wurtzite crystals and quantum wells,” *Phys. Rev. B - Condens. Matter Mater. Phys.*, vol. 61, no. 3, pp. 2034–2040, 2000.
- [51] V. Y. Davydov *et al.*, “Phonon dispersion and Raman scattering in hexagonal GaN and AlN,” *Phys. Rev. B - Condens. Matter Mater. Phys.*, vol. 58, no. 19, pp. 12899–12907, 1998.
- [52] H. Harima, “Properties of GaN and related compounds studied by means of Raman scattering,” *J. Phys. Condens. Matter*, vol. 14, no. 38, 2002.
- [53] S. M. Komirenko, K. W. Kim, M. A. Strosio, and M. Dutta, “Dispersion of polar optical phonons in wurtzite quantum wells,” *Phys. Rev. B*, vol. 59, no. 7, pp. 5013–5020, 1999.
- [54] J. Baur, K. Maier, M. Kunzer, U. Kaufmann, and J. Schneider, “Determination of the GaN/AlN band offset via the (-/0) acceptor level of iron,” *Appl. Phys. Lett.*, vol. 65, no. 17, pp. 2211–2213, 1994.

- [55] P. Sohi, D. Martin, and N. Grandjean, “Critical thickness of GaN on AlN: Impact of growth temperature and dislocation density,” *Semicond. Sci. Technol.*, vol. 32, no. 7, 2017.
- [56] M. E. Levinshtein, S. L. Rumyantsev, and M. S. Shur, *Properties of Advanced Semiconductor Materials: GaN, AlN, InN, BN, SiC, SiGe*. John Wiley & Sons, 2001.
- [57] K. Park and C. Bayram, “Thermal resistance optimization of GaN/substrate stacks considering thermal boundary resistance and temperature-dependent thermal conductivity,” *Appl. Phys. Lett.*, vol. 109, no. 15, 2016.
- [58] T. P. Chow *et al.*, “SiC and GaN bipolar power devices,” *Solid. State. Electron.*, vol. 44, no. 2, pp. 277–301, 2000.
- [59] E. T. Swartz and R. O. Pohl, “Thermal boundary resistance,” *Rev. Mod. Phys.*, vol. 61, no. 3, pp. 605–668, 1989.
- [60] G. J. Riedel *et al.*, “Reducing thermal resistance of AlGaIn/GaN electronic devices using novel nucleation layers,” *IEEE Electron Device Lett.*, vol. 30, no. 2, pp. 103–106, 2009.
- [61] Sangmin Lee *et al.*, “Reliability assessment of AlGaIn/GaN HEMT technology on SiC for 48V applications,” in *2008 IEEE International Reliability Physics Symposium*, 2008, pp. 446–449.
- [62] Y. -f. Wu, M. Moore, A. Saxler, T. Wisleder, and P. Parikh, “40-W/mm double field-plated GaN HEMTs,” in *2006 64th Device Research Conference*, 2006, pp. 151–152.
- [63] J. Cho, E. Bozorg-Grayeli, D. H. Altman, M. Asheghi, and K. E. Goodson, “Low thermal resistances at GaN-SiC interfaces for HEMT technology,” *IEEE Electron Device Lett.*, vol. 33, no. 3, pp. 378–380, 2012.
- [64] J. W. Pomeroy, M. Bernardoni, D. C. Dumka, D. M. Fanning, and M. Kuball, “Low thermal resistance GaN-on-diamond transistors characterized by three-dimensional Raman thermography mapping,” *Appl. Phys. Lett.*, vol. 104, no. 8, pp. 6–11, 2014.

- [65] J. Cho *et al.*, “Thermal characterization of GaN-on-diamond substrates for HEMT applications,” *Intersoc. Conf. Therm. Thermomechanical Phenom. Electron. Syst. ITherm*, pp. 435–439, 2012.
- [66] H. Sun *et al.*, “Reducing GaN-on-diamond interfacial thermal resistance for high power transistor applications,” *Appl. Phys. Lett.*, vol. 106, no. 11, 2015.
- [67] Y. Won, J. Cho, D. Agonafer, M. Asheghi, and K. E. Goodson, “Fundamental cooling limits for high power density gallium nitride electronics,” *IEEE Trans. Components, Packag. Manuf. Technol.*, vol. 5, no. 6, pp. 737–744, Jun. 2015.
- [68] *Sentaurus Device User Guide Version K-2015.6*. Synopsys, Mountain View, CA, USA, 2015.
- [69] D. I. Babić, “Optimal AlGaIn/GaN HEMT buffer layer thickness in the presence of an embedded thermal boundary,” *IEEE Trans. Electron Devices*, vol. 61, no. 4, pp. 1047–1053, 2014.
- [70] H. C. Nochetto, N. R. Jankowski, and A. Bar-Cohen, “The impact of GaN/substrate thermal boundary resistance on a HEMT device,” *ASME 2011 Int. Mech. Eng. Congr. Expo. IMECE 2011*, vol. 10, no. PARTS A AND B, pp. 241–249, 2011.
- [71] J. Piprek, *Nitride Semiconductor Devices: Principles and Simulation*. Wiley Online Library, 2007.
- [72] A. M. Darwish, A. J. Bayba, and H. A. Hung, “Thermal resistance calculation of AlGaIn-GaN devices,” *IEEE Trans. Microw. Theory Tech.*, vol. 52, no. 11, pp. 2611–2620, 2004.
- [73] A. Sarua *et al.*, “Thermal boundary resistance between GaN and substrate in AlGaIn/GaN electronic devices,” *IEEE Trans. Electron Devices*, vol. 54, no. 12, pp. 3152–3158, 2007.
- [74] A. Manoi, J. W. Pomeroy, N. Killat, and M. Kuball, “Benchmarking of thermal boundary resistance in AlGaIn/GaN HEMTs on SiC substrates: Implications of the nucleation layer microstructure,” *IEEE Electron Device Lett.*, vol. 31, no. 12, pp. 1395–1397, 2010.

- [75] M. Kuball, N. Killat, A. Manoi, and J. W. Pomeroy, "Benchmarking of thermal boundary resistance of GaN-SiC interfaces for AlGaIn/GaN HEMTs: US, European and Japanese suppliers," *2010 Int. Conf. Compd. Semicond. Manuf. Technol. CS MANTECH 2010*, 2010.
- [76] J. Zou, D. Kotchetkov, A. A. Balandin, D. I. Florescu, and F. H. Pollak, "Thermal conductivity of GaN films: Effects of impurities and dislocations," *J. Appl. Phys.*, vol. 92, no. 5, pp. 2534–2539, 2002.
- [77] K. A. Filippov and A. A. Balandin, "The effect of the thermal boundary resistance on self-heating of AlGaIn/GaN HFETs," *MRS Internet J. Nitride Semicond. Res.*, vol. 8, no. 2, pp. 8–11, 2003.
- [78] T. A. Eckhause, Ö. Süzer, Ç. Kurdak, F. Yun, and H. Morkoç, "Electric-field-induced heating and energy relaxation in GaN," *Appl. Phys. Lett.*, vol. 82, no. 18, pp. 3035–3037, 2003.
- [79] L. De Bellis, P. E. Phelan, and R. S. Prasher, "Variations of acoustic and diffuse mismatch models in predicting thermal-boundary resistance," *J. Thermophys. Heat Transf.*, vol. 14, no. 2, pp. 144–150, Apr. 2000.
- [80] G. A. Slack, L. J. Schowalter, D. Morelli, and J. A. Freitas, "Some effects of oxygen impurities on AlN and GaN," *J. Cryst. Growth*, vol. 246, no. 3–4, pp. 287–298, 2002.
- [81] D. I. Florescu *et al.*, "Thermal conductivity of fully and partially coalesced lateral epitaxial overgrown GaN/sapphire (0001) by scanning thermal microscopy," *Appl. Phys. Lett.*, vol. 77, no. 10, pp. 1464–1466, 2000.
- [82] H. Morkoç, *Handbook of Nitride Semiconductors and Devices Vol. 1: Materials Properties, Physics and Growth*. Wiley-VCH Verlag GmbH & Co. KGaA, Weinheim, 2008.
- [83] J. Das *et al.*, "Improved thermal performance of AlGaIn/GaN HEMTs by an optimized flip-chip design," *IEEE Trans. Electron Devices*, vol. 53, no. 11, pp. 2696–2702, 2006.

- [84] A. N. Smith and J. P. Calame, "Impact of thin film thermophysical properties on thermal management of wide bandgap solid-state transistors," *Int. J. Thermophys.*, vol. 25, no. 2, pp. 409–422, 2004.
- [85] C. Luo, D. R. Clarke, and J. R. Dryden, "The temperature dependence of the thermal conductivity of single crystal GaN films," *J. Electron. Mater.*, vol. 30, no. 3, pp. 138–146, 2001.
- [86] X. Chen, F. N. Donmezer, S. Kumar, and S. Graham, "A numerical study on comparing the active and passive cooling of AlGaIn/GaN HEMTs," *IEEE Trans. Electron Devices*, vol. 61, no. 12, pp. 4056–4061, 2014.
- [87] G. A. Slack and C. J. Glassbrenner, "Thermal conductivity of Si and Ge from 3K to the melting point," *Phys. Rev.*, vol. 134, no. 4A, pp. A1058–A1069, 1964.
- [88] S. Russo, V. D'Alessandro, M. Costagliola, G. Sasso, and N. Rinaldi, "Analysis of the thermal behavior of AlGaIn/GaN HEMTs," *Mater. Sci. Eng. B Solid-State Mater. Adv. Technol.*, vol. 177, no. 15, pp. 1343–1351, 2012.
- [89] A. Wang, M. J. Tadjer, and F. Calle, "Simulation of thermal management in AlGaIn/GaN HEMTs with integrated diamond heat spreaders," *Semicond. Sci. Technol.*, vol. 28, no. 5, 2013.
- [90] I. Ahmad, V. Kasisomayajula, D. Y. Song, L. Tian, J. M. Berg, and M. Holtz, "Self-heating in a GaN based heterostructure field effect transistor: Ultraviolet and visible Raman measurements and simulations," *J. Appl. Phys.*, vol. 100, no. 11, pp. 1–7, 2006.
- [91] E. A. Burgemeister, W. Von Muench, and E. Pettenpaul, "Thermal conductivity and electrical properties of 6H silicon carbide," *J. Appl. Phys.*, vol. 50, no. 9, pp. 5790–5794, 1979.
- [92] J. W. Pomeroy and M. Kuball, "Optimizing GaN-on-diamond transistor geometry for maximum output power," *Tech. Dig. - IEEE Compd. Semicond. Integr. Circuit Symp. CSIC*, pp. 14–17, 2014.
- [93] J. E. Butler and A. V. Sumant, "The CVD of nanodiamond materials," *Chem. Vap. Depos.*, vol. 14, no. 7-8 SPEC. ISS., pp. 145–160, 2008.

- [94] M. Nazari, B. L. Hancock, E. L. Piner, and M. W. Holtz, "Self-heating in a GaN-based heterojunction field-effect transistor investigated by ultraviolet and visible micro-Raman spectroscopy," in *2015 IEEE Compound Semiconductor Integrated Circuit Symposium (CSICS)*, 2015, vol. 1, pp. 1–4.
- [95] J. Wu, J. Min, W. Lu, and P. K. L. Yu, "Thermal resistance extraction of AlGaIn/GaN depletion-mode HEMTs on diamond," *J. Electron. Mater.*, vol. 44, no. 5, pp. 1275–1280, 2015.
- [96] E. A. Douglas, F. Ren, and S. J. Pearton, "Finite-element simulations of the effect of device design on channel temperature for AlGaIn/GaN high electron mobility transistors," *J. Vac. Sci. Technol. B, Nanotechnol. Microelectron. Mater. Process. Meas. Phenom.*, vol. 29, no. 2, p. 020603, 2011.
- [97] A. Polian, M. Grimsditch, and I. Grzegory, "Elastic constants of gallium nitride," *J. Appl. Phys.*, vol. 79, no. 6, pp. 3343–3344, 1996.
- [98] C. Deger *et al.*, "Sound velocity of Al_xGa_{1-x}N thin films obtained by surface acoustic-wave measurements," *Appl. Phys. Lett.*, vol. 72, no. 19, pp. 2400–2402, 1998.
- [99] D. G. Cahill, "Analysis of heat flow in layered structures for time-domain thermoreflectance," *Rev. Sci. Instrum.*, vol. 75, no. 12, pp. 5119–5122, 2004.
- [100] H. Jang, C. R. Ryder, J. D. Wood, M. C. Hersam, and D. G. Cahill, "3D anisotropic thermal conductivity of exfoliated rhenium disulfide," *Adv. Mater.*, vol. 29, no. 35, pp. 1–6, 2017.
- [101] P. Jiang, X. Qian, X. Gu, and R. Yang, "Probing anisotropic thermal conductivity of transition metal dichalcogenides MX₂ (M = Mo, W and X = S, Se) using time-domain thermoreflectance," *Adv. Mater.*, vol. 29, no. 36, p. 1701068, 2017.
- [102] P. Jiang, X. Qian, and R. Yang, "Tutorial: Time-domain thermoreflectance (TDTR) for thermal property characterization of bulk and thin film materials," *J. Appl. Phys.*, vol. 124, no. 16, 2018.
- [103] K. Park and C. Bayram, "Impact of dislocations on the thermal conductivity of gallium nitride studied by time-domain thermoreflectance," *J. Appl. Phys.*, vol. 126, no. 18, 2019.

- [104] M. Ha and S. Graham, “Development of a thermal resistance model for chip-on-board packaging of high power LED arrays,” *Microelectron. Reliab.*, vol. 52, no. 5, pp. 836–844, 2012.
- [105] A. Witek, “Some aspects of thermal conductivity of isotopically pure diamond - A comparison with nitrides,” *Diam. Relat. Mater.*, vol. 7, no. 7, pp. 962–964, 1998.
- [106] S. Porowski, “Near defect free GaN substrates,” *MRS Internet J. Nitride Semicond. Res.*, vol. 4, no. S1, pp. 27–37, Jun. 1999.
- [107] D. I. Florescu, V. M. Asnin, F. H. Pollak, R. J. Molnar, and C. E. C. Wood, “High spatial resolution thermal conductivity and Raman spectroscopy investigation of hydride vapor phase epitaxy grown n-GaN/sapphire (0001): Doping dependence,” *J. Appl. Phys.*, vol. 88, no. 6, pp. 3295–3300, 2000.
- [108] A. Jezowski, O. Churiukova, J. Mucha, T. Suski, I. A. Obukhov, and B. A. Danilchenko, “Thermal conductivity of heavily doped bulk crystals GaN:O. Free carriers contribution,” *Mater. Res. Express*, vol. 2, no. 8, 2015.
- [109] R. Rounds *et al.*, “Thermal conductivity of GaN single crystals: Influence of impurities incorporated in different growth processes,” *J. Appl. Phys.*, vol. 124, no. 10, 2018.
- [110] M. Slomski, P. P. Paskov, J. H. Leach, J. F. Muth, and T. Paskova, “Thermal conductivity of bulk GaN grown by HVPE: Effect of Si doping,” *Phys. Status Solidi Basic Res.*, vol. 254, no. 8, pp. 1–5, 2017.
- [111] T. E. Beechem *et al.*, “Size dictated thermal conductivity of GaN,” *J. Appl. Phys.*, vol. 120, no. 9, 2016.
- [112] A. Jezowski *et al.*, “Thermal conductivity of GaN crystals in 4.2-300 K range,” *Solid State Commun.*, vol. 128, no. 2–3, pp. 69–73, 2003.
- [113] B. Łucznik *et al.*, “Deposition of thick GaN layers by HVPE on the pressure grown GaN substrates,” *J. Cryst. Growth*, vol. 281, no. 1, pp. 38–46, 2005.
- [114] R. Dwiliński *et al.*, “Excellent crystallinity of truly bulk ammonothermal GaN,” *J. Cryst. Growth*, vol. 310, no. 17, pp. 3911–3916, 2008.

- [115] K. T. Lee *et al.*, “GaN devices on a 200 mm Si platform targeting heterogeneous integration,” *IEEE Electron Device Lett.*, vol. 38, no. 8, pp. 1094–1096, 2017.
- [116] H. Amano *et al.*, “The 2018 GaN power electronics roadmap,” *J. Phys. D. Appl. Phys.*, vol. 51, no. 16, 2018.
- [117] S. Krukowski *et al.*, “High-nitrogen-pressure growth of GaN single crystals: Doping and physical properties,” *J. Phys. Condens. Matter*, vol. 13, no. 40, pp. 8881–8890, 2001.
- [118] H. P. Lee, J. Perozek, L. D. Rosario, and C. Bayram, “Investigation of AlGaIn/GaN high electron mobility transistor structures on 200-mm silicon (111) substrates employing different buffer layer configurations,” *Sci. Rep.*, vol. 6, no. October, pp. 1–10, 2016.
- [119] E. Arslan, M. K. Ozturk, A. Teke, S. Ozcelik, and E. Ozbay, “Buffer optimization for crack-free GaN epitaxial layers grown on Si(1 1 1) substrate by MOCVD,” *J. Phys. D. Appl. Phys.*, vol. 41, no. 15, 2008.
- [120] J. Yang, E. Ziade, and A. J. Schmidt, “Uncertainty analysis of thermoreflectance measurements,” *Rev. Sci. Instrum.*, vol. 87, no. 1, 2016.
- [121] Y. Wang, J. Y. Park, Y. K. Koh, and D. G. Cahill, “Thermoreflectance of metal transducers for time-domain thermoreflectance,” *J. Appl. Phys.*, vol. 108, no. 4, 2010.
- [122] G. T. Hohensee, W. P. Hsieh, M. D. Losego, and D. G. Cahill, “Interpreting picosecond acoustics in the case of low interface stiffness,” *Rev. Sci. Instrum.*, vol. 83, no. 11, 2012.
- [123] J. Rumble, *CRC Handbook of Chemistry and Physics*. CRC press, 2017.
- [124] E. H. Buyco and F. E. Davis, “Specific heat of aluminum from zero to its melting temperature and beyond. Equation for representation of the specific heat of solids,” *J. Chem. Eng. Data*, vol. 15, no. 4, pp. 518–523, Oct. 1970.
- [125] P. Jiang, X. Qian, and R. Yang, “Time-domain thermoreflectance (TDTR) measurements of anisotropic thermal conductivity using a variable spot size approach,” *Rev. Sci. Instrum.*, vol. 88, no. 7, 2017.

- [126] J. Liu, J. Zhu, M. Tian, X. Gu, A. Schmidt, and R. Yang, “Simultaneous measurement of thermal conductivity and heat capacity of bulk and thin film materials using frequency-dependent transient thermoreflectance method,” *Rev. Sci. Instrum.*, vol. 84, no. 3, 2013.
- [127] B. A. Danilchenko, T. Paszkiewicz, S. Wolski, A. Jezowski, and T. Plackowski, “Heat capacity and phonon mean free path of wurtzite GaN,” *Appl. Phys. Lett.*, vol. 89, no. 6, pp. 1–4, 2006.
- [128] J. Leitner, A. Strejc, D. Sedmidubský, and K. Růžicka, “High temperature enthalpy and heat capacity of GaN,” *Thermochim. Acta*, vol. 401, no. 2, pp. 169–173, 2003.
- [129] S. J. Rosner, E. C. Carr, M. J. Ludowise, G. Girolami, and H. I. Erikson, “Correlation of cathodoluminescence inhomogeneity with microstructural defects in epitaxial GaN grown by metalorganic chemical-vapor deposition,” *Appl. Phys. Lett.*, vol. 70, no. 4, pp. 420–422, 1997.
- [130] M. A. Moram and M. E. Vickers, “X-ray diffraction of III-nitrides,” *Reports Prog. Phys.*, vol. 72, no. 3, 2009.
- [131] M. A. Moram *et al.*, “On the origin of threading dislocations in GaN films,” *J. Appl. Phys.*, vol. 106, no. 7, 2009.
- [132] T. Metzger *et al.*, “Defect structure of epitaxial GaN films determined by transmission electron microscopy and triple-axis X-ray diffractometry,” *Philos. Mag. A*, vol. 77, no. 4, pp. 1013–1025, Apr. 1998.
- [133] P. P. Paskov, M. Slomski, J. H. Leach, J. F. Muth, and T. Paskova, “Effect of Si doping on the thermal conductivity of bulk GaN at elevated temperatures - Theory and experiment,” *AIP Adv.*, vol. 7, no. 9, 2017.
- [134] G. Parish, S. Keller, S. P. Denbaars, and U. K. Mishra, “SIMS investigations into the effect of growth conditions on residual impurity and silicon incorporation in GaN and Al_xGa_{1-x}N,” *J. Electron. Mater.*, vol. 29, no. 1, pp. 15–20, 2000.
- [135] D. T. Morelli, J. P. Heremans, and G. A. Slack, “Estimation of the isotope effect on the lattice thermal conductivity of group IV and group III-V semiconductors,” *Phys. Rev. B - Condens. Matter Mater. Phys.*, vol. 66, no. 19, pp. 1953041–1953049, 2002.

- [136] C. Mion, J. F. Muth, E. A. Preble, and D. Hanser, “Accurate dependence of gallium nitride thermal conductivity on dislocation density,” *Appl. Phys. Lett.*, vol. 89, no. 9, 2006.
- [137] E. Richter *et al.*, “GaN boules grown by high rate HVPE,” *Phys. Status Solidi Curr. Top. Solid State Phys.*, vol. 8, no. 5, pp. 1450–1454, 2011.
- [138] H. Shibata *et al.*, “High thermal conductivity of gallium nitride (GaN) crystals grown by HVPE process,” *Mater. Trans.*, vol. 48, no. 10, pp. 2782–2786, 2007.
- [139] E. Ziade, J. Yang, G. Brummer, D. Nothorn, T. Moustakas, and A. J. Schmidt, “Thickness dependent thermal conductivity of gallium nitride,” *Appl. Phys. Lett.*, vol. 110, no. 3, 2017.
- [140] R. B. Simon, J. Anaya, and M. Kuball, “Thermal conductivity of bulk GaN - Effects of oxygen, magnesium doping, and strain field compensation,” *Appl. Phys. Lett.*, vol. 105, no. 20, pp. 10–15, 2014.
- [141] W. Liu, A. A. Balandin, C. Lee, and H. Y. Lee, “Increased thermal conductivity of free-standing low-dislocation-density GaN films,” *Phys. Status Solidi Appl. Mater. Sci.*, vol. 202, no. 12, pp. 135–137, 2005.
- [142] Q. Zheng, C. Li, A. Rai, J. H. Leach, D. A. Broido, and D. G. Cahill, “Thermal conductivity of GaN, GaN 71, and SiC from 150 K to 850 K,” *Phys. Rev. Mater.*, vol. 3, no. 1, pp. 1–14, 2019.
- [143] J. Cho, Y. Li, W. E. Hoke, D. H. Altman, M. Asheghi, and K. E. Goodson, “Phonon scattering in strained transition layers for GaN heteroepitaxy,” *Phys. Rev. B - Condens. Matter Mater. Phys.*, vol. 89, no. 11, pp. 1–11, 2014.
- [144] C. Y. Luo, H. Marchand, D. R. Clarke, and S. P. Denbaars, “Thermal conductivity of lateral epitaxial overgrown GaN films,” *Appl. Phys. Lett.*, vol. 75, no. 26, pp. 4151–4153, 1999.
- [145] D. Kotchetkov, J. Zou, A. A. Balandin, D. I. Florescu, and F. H. Pollak, “Effect of dislocations on thermal conductivity of GaN layers,” *Appl. Phys. Lett.*, vol. 79, no. 26, pp. 4316–4318, 2001.

- [146] Y. Zhang *et al.*, “Electrothermal simulation and thermal performance study of GaN vertical and lateral power transistors,” *IEEE Trans. Electron Devices*, vol. 60, no. 7, pp. 2224–2230, 2013.
- [147] H. Zhu *et al.*, “Effect of substrate thinning on the electronic transport characteristics of AlGaIn/GaN HEMTs,” *Solid. State. Electron.*, vol. 145, no. September 2017, pp. 40–45, 2018.
- [148] H. K. Lee, J. S. Yu, and Y. T. Lee, “Thermal analysis and characterization of the effect of substrate thinning on the performances of GaN-based light emitting diodes,” *Phys. Status Solidi Appl. Mater. Sci.*, vol. 207, no. 6, pp. 1497–1504, 2010.
- [149] R. Liu and C. Bayram, “Cathodoluminescence study of luminescence centers in hexagonal and cubic phase GaN hetero-integrated on Si(100),” *J. Appl. Phys.*, vol. 120, no. 2, 2016.
- [150] R. Grady and C. Bayram, “Simulation of zincblende AlGaIn/GaN high electron mobility transistors for normally-off operation,” *J. Phys. D. Appl. Phys.*, vol. 50, no. 26, 2017.
- [151] I. Vurgaftman and J. R. Meyer, “Band parameters for nitrogen-containing semiconductors,” *J. Appl. Phys.*, vol. 94, no. 6, pp. 3675–3696, 2003.
- [152] P. G. Moses, M. Miao, Q. Yan, and C. G. Van De Walle, “Hybrid functional investigations of band gaps and band alignments for AlN, GaN, InN, and InGaIn,” *J. Chem. Phys.*, vol. 134, no. 8, 2011.
- [153] V. W. L. Chin, T. L. Tansley, and T. Osotchan, “Electron mobilities in gallium, indium, and aluminum nitrides,” *J. Appl. Phys.*, vol. 75, no. 11, pp. 7365–7372, 1994.
- [154] J. Edwards, K. Kawabe, G. Stevens, and R. H. Tredgold, “Space charge conduction and electrical behaviour of aluminium nitride single crystals,” *Solid State Commun.*, vol. 3, no. 5, pp. 99–100, 1965.
- [155] C. G. Rodrigues *et al.*, “Hole mobility in zincblende c-GaN,” *J. Appl. Phys.*, vol. 95, no. 9, pp. 4914–4917, 2004.